FEDERAL CENTER OF TECHNOLOGICAL EDUCATION OF MINAS GERAIS
CIVIL ENGINEERING DEPARTMENT

ELAYNE MARQUES SILVA

INVESTIGATION ON BOND AND CRACKING BEHAVIOURS OF GFRP-REINFORCED CONCRETE MEMBERS

ELAYNE MARQUES SILVA

“INVESTIGATION ON BOND AND CRACKING BEHAVIOURS OF GFRP-REINFORCED CONCRETE MEMBERS”

Thesis presented to the Graduate Program in Civil Engineering of the Civil Engineering Department of the Federal Center of Technological Education of Minas Gerais, being part of the requirements for the “Doctorate in Civil Engineering” degree.

Advisor: Prof. Dr. Péter Ludvig
Co-advisor: Prof. Dr. Kent A. Harries

BELO HORIZONTE
2023

Silva, Elayne Marques
S586e Investigation on bond and cracking behaviours of GFRP - Reinforced Concrete Members. / Elayne Marques Silva. – – Belo Horizonte, 2024.
174 f. : il.

Tese (doutorado) – Centro Federal de Educação Tecnológica de Minas Gerais. Programa de Pós-Graduação em Engenharia Civil. 2024.
Orientador: Prof. Dr. Péter Ludvig
Coorientador: Prof. Dr Kent A. Harries – University of Pittsburgh.

Bibliografia

1. Concreto. 2. Barras (Engenharia) – Fibra de vidro. 3. Resistência de Materiais. I. Ludvig, Peter. II. Centro Federal de Educação Tecnológica de Minas Gerais. III. Título

CDD 693.54

Elaboração da ficha catalográfica pela Bibliotecária Elisângela Gonçalves Barbieri CRB-2 2624 / CEFET-MG

ELAYNE MARQUES SILVA

“INVESTIGATION ON BOND AND CRACKING BEHAVIOURS OF GFRP-REINFORCED CONCRETE MEMBERS”

Thesis presented to the Graduate Program in Civil Engineering of the Civil Engineering Department of the Federal Center of Technological Education of Minas Gerais, being part of the requirements for the “Doctorate in Civil Engineering” degree.

Examination committee:

_____

Prof. Péter Ludvig – Supervisor
Department of Civil Engineering – CEFET-MG

_____

Prof. Kent A. Harries – Supervisor
Department of Civil and Environmental Engineering – University of Pittsburgh

_____

Prof. Conrado de Souza Rodrigues
Department of Civil Engineering – CEFET-MG

_____

Prof. Cristina Barris
Department of Mechanical Engineering and Industrial Construction – Universitat de Girona

_____

Prof. Sandor Sólyom,
Department of Construction Materials and Technologies – Budapest University of Technology and Economics

_____

Prof. Sofia Maria Carrato Diniz
Department of Structural Engineering – UFMG

Belo Horizonte, December 14th, 2023.

ACKNOWLEDGEMENTS

First of all, I would like to thank God for giving me strength to finish this work although many difficulties that arose from a pandemic season that the world faced: "*For I know the plans I have for you, declares the Lord, plans to prosper you and not to harm you, plans to give you hope and a future*" (Jeremiah 29:11).

I do not have enough words to express all my gratitude for each person involved in the accomplishment of this work!

I will start expressing my thanks to my family for all the patience and understanding they showed to me. A special thanks to my sister (-in-law) Tamiris and my friends Angélica, Laisa Cristina, Karol, Renata, and Vânia for always encouraging me during the completion of this work. To my spiritual leaders, Fernanda and Luiz, thank you for the prayers and advice. My thanks to Evens Robert, who supported me for most part of this journey, I will always be grateful for you. Thanks to my love Vinícius, who was an unexpected gift for me and was very important to encourage me in the final steps of this journey. I love you!

I would like to express my appreciation and gratitude to my advisor, Dr. Péter Ludvig from Federal Center of Technological Education of Minas Gerais (CEFET-MG), for believing in my potential to develop this research; my deepest gratitude to my co-advisor, Dr. Kent Harries from University of Pittsburgh, for accepting to be my supervisor and for receiving me during my sandwich program. Thank you both for all advice, support, teachings, and patience to help me, my endless gratitude.

I would like to express my immense gratitude to Professor Conrado de Souza Rodrigues from CEFET-MG for his excellent lectures and for all the support he provided me during my course.

I would also like to thank Professors Júnia Nunes de Paula, Nilton Maia, Rogério Cabral, Sándor Sólyom, and my master advisor Sofia Maria Carrato Diniz for their cooperation and guidance.

I could not fail to mention my deep gratitude to Professor Hersília de Andrade Santos, who showed great solidarity for me in the moment I most needed in the final stretch of my doctorate.

To the staff members of CEFET-MG and University of Pittsburgh, for the support, especially Ivan Batista Morais from CEFET-MG and Charles Hager from University of Pittsburgh, for all the laboratory support.

A special thanks to my colleagues Bruno, Isabela, Laísa Carneiro, André, and Taciana from CEFET-MG and Dr. Shawn Platt from University of Pittsburgh for helping me with my experimental tests.

To the lovely people I met in Pittsburgh: Connie, Laura, Jacob, Yingbo, Ping, for the affection. I would like to thank a special friend I made in Pittsburgh, Chase Rogers. Thank you for making me feel at home during my stay and welcoming me in my hard moments.

To CAPES, FAPEMIG, and CEFET-MG for the financial support. This study was financed in part by the Coordenação de Aperfeiçoamento de Pessoal de Nível Superior - Brasil (CAPES) - Finance Code 001.

I wish to acknowledge the support of the following companies: Stratus FRP, Owens Corning, Belgo Bekaert, Lafarge Holcim, Weiler C. Holzberger Industrial, The Perryman Company, and Viapol.

RESUMO

Embora as barras de reforço de polímero reforçado com fibra de vidro (GFRP) estejam se tornando comuns, suas propriedades mecânicas – baixo módulo de elasticidade e alta resistência à tração – fazem com que o projeto de membros de concreto reforçado com GFRP (GFRP-RC) seja frequentemente governado pelo controle de flechas e fissuras no Estado Limite de Utilização. O desempenho de aderência das barras de GFRP impacta o controle de fissuras fornecido e, devido à natureza empírica da caracterização da aderência no projeto, a aderência das barras de GFRP é descrita em relação à do aço. Para descrever o desempenho da aderência das barras de GFRP, um coeficiente dependente da ligação, k_b, é adotado em normas de projeto. Os comportamentos de aderência e fissuração das barras de GFRP no concreto – incluindo a estimativa de k_b – foram investigados a partir de 80 testes de arrancamento e 12 testes de tensão de prisma não-padronizados. Neste trabalho é proposta a avaliação de k_b utilizando o ensaio de arrancamento preconizado pela norma ASTM D7913, confirmando o desempenho da aderência utilizando um menor número de testes de tensão do prisma. Esse teste não padronizado tem a vantagem de fornecer comparação quantitativa, além de qualitativa, do comportamento de fissuração, uma vez que é afetado pelas características da barra de reforço. Os dados obtidos neste programa experimental complementaram um banco de dados existente de 137 resultados de testes de arrancamento comparáveis, incluindo uma variedade de parâmetros de barras de GFRP e concreto. Com o objetivo demonstrar a influência de alguns parâmetros na estimativa de k_b, esse trabalho também apresenta um estudo paramétrico de k_b baseado em 157 dados disponíveis em 19 estudos publicados nos quais k_b foi previsto a partir de testes experimentais de flexão utilizando barras de GFRP.

Palavras-chave: Comportamento de Aderência; Coeficiente de Aderência; Fissuração; Barra GFRP; Ensaio de Tração de Prisma; Ensaio de Arrancamento.

ABSTRACT

Although Glass Fiber-Reinforced Polymer (GFRP) reinforcing bars are becoming commonplace, their mechanical properties – low modulus of elasticity and high tensile strength – result in design of GFRP-reinforced concrete members (GFRP-RC) often being governed by deflection and crack control at the serviceability limit state. Bond performance of GFRP bars impacts the crack control provided and, due to the empirical nature of bond characterisation in design, bond of GFRP remains described in relation to that of steel. To describe the bond performance of GFRP bars, a bond-dependent coefficient, k_b, is adopted in design guides and standards. The bond and cracking behaviours of GFRP bars embedded in concrete – including the estimation of k_b – were investigated through 80 pull-out and 12 non-standard prism tension tests. The evaluation of k_b using ASTM D7913 pull-out, confirming the bond performance using a smaller number of prism tension tests, is proposed. This non-standard test has the advantage of providing quantitative, in addition to qualitative comparison of cracking behaviour as it is affected by reinforcing bar characteristics. The data obtained in this experimental programme supplemented an extant database of 137 comparable pull-out test results covering a range of GFRP bar and concrete parameters. In order to demonstrate the influence of some parameters in the estimation of k_b, this work also presents an parametric study of k_b based on 157 data available in 19 published studies in which k_b was predicted from experimental flexural tests using GFRP bars.

Keywords: Bond Behaviour; Bond-Dependent Coefficient; Cracking; GFRP Bar; Prism Tension Test; Pull-Out Test.

LIST OF FIGURES

Figure 2.1 – Concrete uniaxial tensile stress-strain behaviour. 27

Figure 2.2 – Transfer of forces from concrete to reinforcement. 30

Figure 2.3 – Definitions of A615 steel geometry. 31

Figure 2.4 – Simply-supported beam subject to flexure. 32

Figure 2.5 – Equilibrium conditions. 32

Figure 2.6 – Variation of steel force and bond stress in reinforced concrete member subject to pure bending: (a) cracked concrete segment, (b) bond stress acting on reinforcing bar, (c) variation of tensile force in steel, and (d) variation of bond stresses along steel. 34

Figure 2.7 – ASTM D7913-14 (2020) pull-out test set-up. 35

Figure 2.8 – Schematic representation of prism tension test and stresses in bar and concrete. 37

Figure 2.9 – Schematic representation of concrete stress, bond stress, and slip between two primary cracks. 39

Figure 3.1 – Number of specimens tested *versus* year of publication work. 53

Figure 3.2 – Flowchart of deterministic procedure to back calculate k_b based on Frosch equation. 55

Figure 3.3 – Reported (a) and calculated (b) k_b (Equation 2.11) *versus* crack width. 63

Figure 3.4 – Reported and calculated k_b (Equation 2.11) *versus* bar diameter (for w = 0.70 mm). 64

Figure 3.5 – GFRP reinforcing bar stress, f_f, *versus* diameter (for w = 0.70 mm). 65

Figure 3.6 – Representative example of calculated k_b (Equation 2.11) *versus* bar stress, f_f, (for w = 0.70 mm) for beams tested by Abdelkarim et al. (2019). 66

Figure 3.7 – Reported and calculated k_b (Equation 2.11) *versus* clear cover (for w = 0.70 mm). 66

Figure 3.8 – Reported and calculated k_b (Equation 2.11) *versus* concrete compressive strength (for w = 0.70 mm).....67

Figure 3.9 – Reported and calculated k_b (Equation 2.11) *versus* surface treatment (for w = 0.70 mm).....68

Figure 3.10 – Reported k_b (Equation 2.11) *versus* service stress level (for w = 0.70 mm).....70

Figure 3.11 – Calculated and reported k_b (Equation 2.11) *versus* year (for w = 0.70 mm).....71

Figure 3.12 – Bar stress, f_f, versus bond performance parameters. 78

Figure 3.13 – Bar stress, f_f, versus normalised bond coefficient, k_b/w, for different bar surface treatments for w > 0.10 mm.....80

Figure 4.1 – Details of the mechanical characterisation of #2 hGFRP and #3 hGFRP bars. ...87

Figure 4.2 – Failure mode of (a) #2 hGFRP and (b) #3 hGFRP bars.....88

Figure 5.1 – Details of ASTM D7913 test specimens: 200 mm cube moulds prior to concrete casting.....96

Figure 5.2 – ASTM D7913 test specimens after concrete casting at (a) CEFET-MG and (b) PITT.....96

Figure 5.3 – ASTM D7913 test set-up. 97

Figure 5.4 – Bond-stress slip curves for reinforcing bars: (a) #2 steel, (b) #3 steel, (c) #2 hGFRP, (d) #3 hGFRP, (e) #4 steel, (f) #6 steel, (g) #4 rGFRP, (h) #6 rGFRP, (i) #4 sGFRP, (j) #5 sGFRP, and (k) #5 sGFRP-s.....101

Figure 5.5 - Representative bond stress versus slip relationships from pull-out tests.....102

Figure 5.6 – Bond stress from ASTM D7913 test (MPa).....108

Figure 5.7 – Maximum bond stress *versus* relative rib area. 109

Figure 5.8 – Relative rib area *versus* bond-dependent coefficient. 110

Figure 5.9 – Maximum bond stress *versus* relative rib area for data of Sólyom and Bálazs study. 111

Figure 5.10 – Relative rib area *versus* bond-dependent coefficient for data of Sólyom and Bálazs study. 111

Figure 5.11 – Maximum bond stress *versus* bond-dependent coefficient for data of Sólyom and Bálazs study. 112

Figure 6.1 – Details of prism forms. 120

Figure 6.2 – Prism tension test set-up (#6 steel shown). 121

Figure 6.3 – Prism test and crack pattern: #4 steel – specimen 1. 123

Figure 6.4 – Prism test and crack pattern: #4 steel – specimen 2. 123

Figure 6.5 – Prism test and crack pattern: #6 steel – specimen 1. 124

Figure 6.6 – Prism test and crack pattern: #6 steel – specimen 2. 124

Figure 6.7 – Prism test and crack pattern: #6 steel – specimen 3. 125

Figure 6.8 – Prism test and crack pattern: #4 rGFRP – specimen 1. 125

Figure 6.9 – Prism test and crack pattern: #4 rGFRP – specimen 2. 125

Figure 6.10 – Prism test and crack pattern: #6 rGFRP – specimen 1. 126

Figure 6.11 – Prism test and crack pattern: #6 rGFRP – specimen 2. 126

Figure 6.12 – Prism test and crack pattern: #6 rGFRP – specimen 3. 126

Figure 6.13 – Prism test and crack pattern: #4 sGFRP – specimen 1. 127

Figure 6.14 – Prism test and crack pattern: #4 sGFRP – specimen 2.....127

Figure 7.1 – Test specimens and apparatus. 136

Figure 7.2 – Applied load versus displacement results for sand adhesion tests. 138

Figure B.1 – Moment-to-maximum crack width relationships. 160

LIST OF TABLES

Table 3.1 – Summary of the results for k_b. 56

Table 3.2 – Minimum and maximum k_b values for each type of surface treatment. 69

Table 3.3 – Correlation matrix of surface configuration of GFRP bars. 69

Table 3.4 – Mean k_b values. 72

Table 3.5 - Variables considered in one-way ANOVA analyses. 73

Table 3.6 – Spearman correlation coefficients, r_s. 74

Table 3.7 – Equations of trend lines shown in Figure 3.12. 76

Table 3.8 – Summary of bond parameters for w > 0.10 mm shown in Figure 3.13. 80

Table 4.1 – Composition of concrete mixes and strengths. 83

Table 4.2 – Characteristics of bars used in this study. 85

Table 4.3 – Geometric properties of bars. 89

Table 4.4 – Deformation measurements (lug) of bars (undeformed sand-coated bars not included). 91

Table 4.5 – Summary of deformation measurements requirements. 92

Table 5.1 – Pull-out tests results. 99

Table 5.2 – Correlation matrix of bond behaviour of the bars tested. 105

Table 6.1 – Prism tension test results. 122

Table 6.2 – Bond-dependent coefficient (k_b) calculated ASTM D7913 from pull-out and prism tension tests. 131

Table 7.1 – Results from sand adhesion tests. 139

Table A.1 – Details of the specimens of the database of the parametric study. 154

Table C.1 – Calculation of tensile strength of C3 concrete. 164

Table D.1 – Pull-out test results. 165

Table E.1 – Results of the pull-out tests of the experimental database. 169

TABLE OF CONTENTS

1. INTRODUCTION 18
   1.1 Statement of the problem 18
   1.2 Research significance 22
   1.3 Objectives 23
   1.4 Organization of the thesis 24
2. LITERATURE REVIEW 26
   2.1 Mechanical properties of materials 26
      2.1.1 Concrete 26
      2.1.2 Glass fiber-reinforced polymer bars 28
      2.1.3 Mechanisms of reinforcing bar bond to concrete 29
         2.1.3.1 “Relative rib area” parameter 30
      2.1.4 Assessing bond of reinforcing bars to concrete 31
         2.1.4.1 Bond development in flexural member 31
         2.1.4.2 Bond development in member subjected to direct pull-out 35
         2.1.4.3 Bond development in tension member 36
         2.1.4.4 Discussion on the bond mechanisms 40
   2.2 CRACKING PREDICTIONS AND BOND-DEPENDENT COEFFICIENT 41
      2.2.1 General design considerations 41
      2.2.2 Equations for cracking control of GFRP-reinforced concrete members 43
         2.2.2.1 Modified Gergely-Lutz equation 43
         2.2.2.2 Modified Frosch equation 44
         2.2.2.3 Indirect flexural crack control approach 44
      2.2.3 Review of studies on bond-dependent coefficient 45
   2.3 Summary of the chapter 50
3. PARAMETRIC STUDY 52
   3.1 Experimental database 52
      3.1.1 Assumptions of experimental database analysis 54
   3.2 Discussion of the qualitative analysis 62
      3.2.1 k_b versus crack width 62
      3.2.2 k_b versus bar diameter 64

3.2.3 k_b versus clear cover and concrete compressive strength 66
3.2.4 k_b versus surface treatment 67
3.2.5 k_b versus service stress 70
3.2.6 Gergely-Lutz equation versus Frosch equation 71
3.3 Meta-analysis 73
3.4 Discussion of the quantitative analysis 75
3.4.1 Source-reported bond coefficients: $k_{b,F}$ 75
3.4.2 Normalising by crack width: k_b/w 75
3.4.3 Effects of bar surface treatment 79
3.5 Summary of the chapter 81
4. MATERIALS CHARACTERISATION 83
4.1 Concrete 83
4.2 Reinforcing bars 85
4.2.1 #5 sGFRP-s bars 86
4.2.2 Mechanical characterisation 86
4.2.3 Geometric characterisation 88
4.2.3.1 Area of bar 88
4.2.3.2 Deformation measurements 90
4.3 Summary of the chapter 93
5. PULL-OUT TEST 94
5.1 Introduction 94
5.2 Test details 95
5.2.1 Test specimens 95
5.2.2 Test set-up and procedure 97
5.2.3 Pull-out test results 98
5.3 Discussion of the pull-out experimental results 102
5.3.1 Statistical analysis 104
5.4 Experimental database 106
5.4.1 Statistical analysis 112
5.5 Summary of the chapter 114
6. PRISM TENSION TEST 118
6.1 Introduction 118

6.2 Test details 120
6.2.1 Test specimens 120
6.2.2 Test set-up and procedure 121
6.2.3 Prism test results 122
6.3 Discussion of the prism tension test results 128
6.3.1 Comparison of test methods 129
6.4 Summary of the chapter 132
7. SAND ADHESION TEST 133
7.1 Introduction 133
7.2 Test details 135
7.2.1 Test specimens and procedure 135
7.2.2 Sand adhesion test results and discussion 137
7.3 Summary of the chapter 141
8. FINAL REMARKS 142
8.1 Conclusions 142
8.2 Recommendations for future works 145
REFERENCES 146
APPENDIX A – CHARACTERISTICS OF THE SPECIMENS OF THE EXPERIMENTAL DATABASE 154
APPENDIX B – CALCULATION EXAMPLE: BOND-DEPENDENT COEFFICIENT FOR CRACK WIDTH EQUAL TO 0.70 mm 159
B.1 Geometric characteristics and mechanical properties of materials 159
B.2 Procedure for calculation of the bond-dependent coefficient 159
B.2.1 Tensile stress in GFRP reinforcement, f_f 160
B.2.2 Ratio of the distance from the neutral axis of the member to the extreme tension fiber to the distance from the neutral axis to the centroid of the tensile reinforcement, β 161
B.2.3 Longitudinal GFRP bar spacing, s 162
B.2.4 Bond-dependent coefficient for crack width of 0.70 mm, $k_{b,w=0.70}$ 162
APPENDIX C – CALCULATION OF TENSILE STRENGTH OF C3 CONCRETE 163
APPENDIX D – PULL-OUT TESTS RESULTS FOR ALL SPECIMENS 165
APPENDIX E – DETAILS OF THE COMPLETE EXPERIMENTAL DATABASE OF PULL-OUT TESTS 168

1

INTRODUCTION

1.1 Statement of the problem

Many reinforced concrete (RC) structures are subjected to deicing salts, salt water exposure, or to harsh environments that reduce the alkalinity of concrete, leading to corrosion of steel reinforcement and, consequently, affecting the service life of structures. Fiber-Reinforced Polymer (FRP) reinforcing bars are resistant to corrosion and have emerged as an alternative to steel as internal reinforcement in concrete structures to mitigate the problem of corrosion.

FRP is a composite material made of continuous fibers, usually glass (GFRP), carbon (CFRP), and more recently, basalt (BFRP), embedded in a polymeric (typically vinyl-ester) matrix. GFRP reinforcing bars have been most frequently used in RC structures due to their lower cost compared to the other FRP bars. The design of GFRP-reinforced concrete is standardized by ACI Committee 440 (ACI CODE 440.11-22, 2022) and specification standards for GFRP bars have been established (ASTM D7957). There is no current Brazilian document addressing utilization of FRP in civil construction. The Brazilian Committees "Special Study of Non-Conventional Materials as Reinforcement in Reinforced Concrete Structures" (CEE-193) – *Comissão de Estudo Especial de Materiais Não Convencionais para Reforço de Estruturas de Concreto*, in Portuguese – and "Studies for Fiber Reinforced Concrete Structures" (CE-002:124.026) – *Comissão de Estudos de Estruturas de Concreto Reforçado por Fibras*, in Portuguese – are responsible for the formulation of future Brazilian documents that will address requirements for testing GFRP bars and the utilization of these bars in RC structures, respectively.

GFRP bars are unidirectional composites; the glass fibers are oriented along the axis of the bar and exhibit essentially linear-elastic behaviour to rupture (i.e., no yield behaviour). They have tensile strength about 2 to 3 times greater than conventional steel reinforcing bars although their

modulus of elasticity is only about one quarter that of steel. Because of their high degree of anisotropy, GFRP bars exhibit poor shear strength (dominated by weak polymer matrix) and bond performance (affected by shear lag, weak polymer matrix and Poisson effects) (ACI PRC 440.1, 2015).

Although GFRP bars are established for use as concrete reinforcement, the mechanical properties of the bars lead to changes in the design paradigm for GFRP-reinforced concrete (GFRP-RC) structures (Ribeiro and Diniz, 2013). While conventional steel RC structures are typically designed based on the strength limit state and then checked for serviceability requirements, design of GFRP-RC members are often governed by deflection and crack control at the serviceability limit state (Tegola, 1998; Mota et al., 2006; Soltani et al., 2013; ACI PRC 440.1-15, 2015). Furthermore, whereas RC structures are designed to achieve their inherent ductility through steel yielding, GFRP-RC structures are designed to ensure that the GFRP does not rupture. GFRP-RC design is based on, and ductility attributed to, the concrete crushing limit state (ACI CODE 440.11-22).

Due to the differences in the material properties of GFRP and conventional reinforcing steel and their respective interactions with the surrounding concrete, the bond performance of GFRP differs from that of steel bars. Studies have been reported that show, in addition to the mechanical properties of GFRP bars, surface configuration, bar diameter, concrete strength, and service stress level in the reinforcement may all be expected to influence the bond performance of GFRP bars (Baena et al., 2009; McCallum and Newhook, 2012; Noel and Soudki, 2013). In order to improve bond characteristics in concrete, GFRP bars are manufactured with a variety of surface treatments, preparations and conditions. These include: a) bars that are continuously pultruded with deformations (typically resembling steel reinforcing bars); b) bars that have a post-pultrusion-applied helical GFRP wrap forming deformations; c) smooth bars that are sand-coated; and d) hybrids of these; typically of b) and c).

The bond behaviour between conventional steel and concrete is relatively well established and documented (e.g., ACI PRC 408-03(12), 2012). Nonetheless, provisions for bond are mostly empirical in nature and therefore calibrated to the ‘standard’ steel reinforcing bars used.

Deformation geometry is a critical parameter affecting bond. The so-called "relative rib area" (R_r), is often used (and will be adopted in this study) to quantify bar geometry as it affects the mechanical bond between reinforcing steel and concrete. By combining the minimum requirements for steel reinforcing bar deformations prescribed by ASTM A615, the *de facto* requirement that $R_r \geq 0.05$ is found – although not specifically stated. The condition that $R_r \geq 0.05$ is understood to be an indicator of "adequate bond performance" of steel reinforcing bars – meeting the minimum requirements of ASTM A615. Due to the different material properties and behaviour, extension of bond requirements for steel to GFRP is not necessarily appropriate and requires investigation.

The expanded use of GFRP in construction is dependent, among other factors, on a better comprehension of the bond interaction between GFRP bars and concrete. The bond performance affects cracking behaviour – including crack spacing and width – and ultimately deflections and durability. Permitted crack widths, w, for GFRP-RC elements are typically assumed to be greater than those for steel-reinforced concrete members due to the corrosion-resistance of GFRP. This is an arbitrary assessment that has come about because, to design with GFRP, one must accept larger crack widths; these have been justified by the improved durability of GFRP bars.

The mechanisms involved in bonding are described in terms of chemical adhesion, surface friction and mechanical interaction at the bar-concrete interface. The latter is the dominant component of bond strength and is affected by bar deformations. Due to the empirical nature of bond characterisation in design, it is necessary to consider the bond of GFRP in relation to that of steel. In order to normalise bond performance for GFRP bar types and permit the use of single design equations, a bond-dependent coefficient, k_b, is adopted which allows the designer to treat other materials or bar geometries in a manner similar to conventional deformed steel bars. Since bond behaviour models of conventional steel reinforcing bars embedded in concrete are relatively well-known and considered to be adequate, steel bars conforming to the geometry requirements of ASTM A615 are the 'norm' for which $k_b = 1.0$. For other bars, a factor $1/k_b$ is applied to normalise bond properties to those of deformed steel bars. That is, when FRP bars exhibit bond behaviour similar that to deformed steel bars, $k_b = 1.0$; for FRP bars having bond

behaviour inferior to steel bars, k_b is greater than 1.0; and for FRP reinforcement presenting bond performance superior to steel, k_b is less than 1.0 (ACI PRC 440.1-15).

1.2 Research significance

There are no agreed standards for determining k_b or for values of k_b itself. Research on assessment of the bond behaviour of GFRP in concrete through the estimation of a k_b factor is not extensive. ACI PRC 440.1-15 (2015) identifies the test method prescribed in Annex S of CSA S806-12 (2012) as a means for determining k_b of GFRP bars. This test consists of a beam measuring 200 mm wide x 300 mm deep x 3,000 mm long loaded in four-point bending. The test also requires a means of reliably maintaining a constant load for 24 hours. The dimensions of the beam make handling difficult and are a barrier to performing such tests with the large number of specimens required to establish reliable results. Thus, it is necessary to establish practical protocols for establishing and verifying (for quality assurance/quality control – QA/QC – purposes) bond performance and values of k_b for the large variation of GFRP bars available in the market. Additionally, confirming crack control performance of these bars is required for improved design standard recommendations.

In this context, this thesis proposes two relatively simple tests – the ASTM D7913 pull-out and non-standard prism tension tests developed further as part of this work – to assess the bond performance and cracking behaviours of GFRP bars, respectively. This work presents the evaluation of k_b using ASTM D7913 and confirming bond performance using a smaller number of prism tension tests. Data from the seven GFRP bar types considered in this study are used to supplement and extend an earlier database of 36 GFRP bar types reported by Sólyom and Balázs (2020). Additionally, this work presents a parametric study based on data available in published literature in order to analyze the influence of different parameters in the estimation of k_b.

1.3 Objectives

The objective of this work is to investigate the bond behaviour of GFRP bars in concrete including the estimation of the bond-dependent coefficient k_b, and determining how the bond performance affects the cracking behaviour (crack spacing and width) of GFRP-reinforced concrete elements.

For these purposes, the following specific tasks were undertaken:

— literature review on the estimation of k_b through experimental tests to identify how different factors were involved in the prediction of k_b;
— investigate, through a parametric study, the main parameters that could affect the estimation of k_b from an assembled database of published works;
— experimentally investigate the bond behaviour and estimation of k_b of GFRP bars in concrete using ASTM D7913 pull-out tests;
— experimentally investigate the cracking behaviour and estimation of k_b of GFRP bars using prism tension tests;
— assemble and analyze a database from the experimental results obtained in this work and comparable results from a study reported by Sólyom and Balázs (2020).

1.4 Organization of the thesis

Chapter 2 provides a literature review on the main mechanical properties of concrete and GFRP bars. A summary of cracking predictions and bond-dependent coefficient, k_b, for GFRP-reinforced concrete members is also presented. Additionally, a brief literature review of parameters that can influence the estimation of k_b is presented.

In Chapter 3, a parametric study of the k_b coefficient is performed. The influence of some parameters on k_b estimation is presented and discussed.

Chapter 4 describes the characterisation and details of the materials used in the experimental program carried out in this work.

Chapter 5 presents the pull-out test experimental program performed in this work. Details of the specimens and instrumentation are reported. A database including the results of the pull-out tests performed in this research and results of a study carried out by collaborators Sólyom and Balázs (2020) is assembled. Finally, a general discussion of the results is also presented.

Chapter 6 contains the description of the experimental prism tension tests performed in this study. The discussion of test results and their relationship to those reported in Chapter 5 are also included in this chapter.

Results from sand-coated bars reported in Chapters 5 and 6 exhibited inconsistent behaviour in some instances. Chapter 7 reports the details and results of additional “sand adhesion tests” used to evaluate the shear capacity of the sand-coated GFRP bars tested in an attempt to better understand the previous results.

Chapter 8 summarizes the main conclusions of this work. Recommendations for future research are also given.

Appendix A reports the characteristics of the specimens that are included on the experimental database presented in Chapter 3.

Appendix B shows an example of the calculation of k_b for crack width equal to 0.70 mm.

Appendix C shows the calculation of tensile strength for C2 concrete based on the appearance of the first crack in the concrete prisms tested by prism tension test.

Appendix D presents the results of the pull-out tests for the 80 specimens tested in the work.

Appendix E reports the details of the complete database of the pull-out tests results for the 80 specimens tested in this work and 137 specimens tested by Sólyom and Balázs (2020).

2

LITERATURE REVIEW

This chapter includes a review of the mechanical properties of concrete and of GFRP bars used as internal reinforcement in reinforced concrete structures. Next, an overview of the cracking behaviour of FRP-RC members and the bond-dependent coefficient, k_b, is presented. The main equations available in North American design codes and guidelines for cracking predictions are described in this context. A review of published studies related to the experimental prediction of k_b is also presented. Finally, a summary of the main aspects addressed in this chapter is reported.

2.1 Mechanical properties of materials

2.1.1 Concrete

Concrete is a brittle material that behaves well under compression but poorly in tension due to aggregate mortar interface that has low tensile strength. Although concrete members subjected to pure axial load do not often occur in practice, an assumed uniaxial stress condition can be justified in many cases (Park and Paulay, 1975) – at the tension face of a member subject to flexure, for instance. Tension behaviour of the concrete is critical when analysing bond behaviour of a member subjected to a tension load (as will be experimentally deployed in Chapter 6) and is therefore described below.

As show in Figure 2.1, concrete subjected to tensile stresses behaves linearly until it reaches its ultimate tensile strength (f_{ct}). For values of strain larger than that corresponding to the maximum tensile strength, the stresses decrease exponentially with an increase of the measured strain (MacGregor, 1997).

Figure 2.1 – Concrete uniaxial tensile stress-strain behaviour.

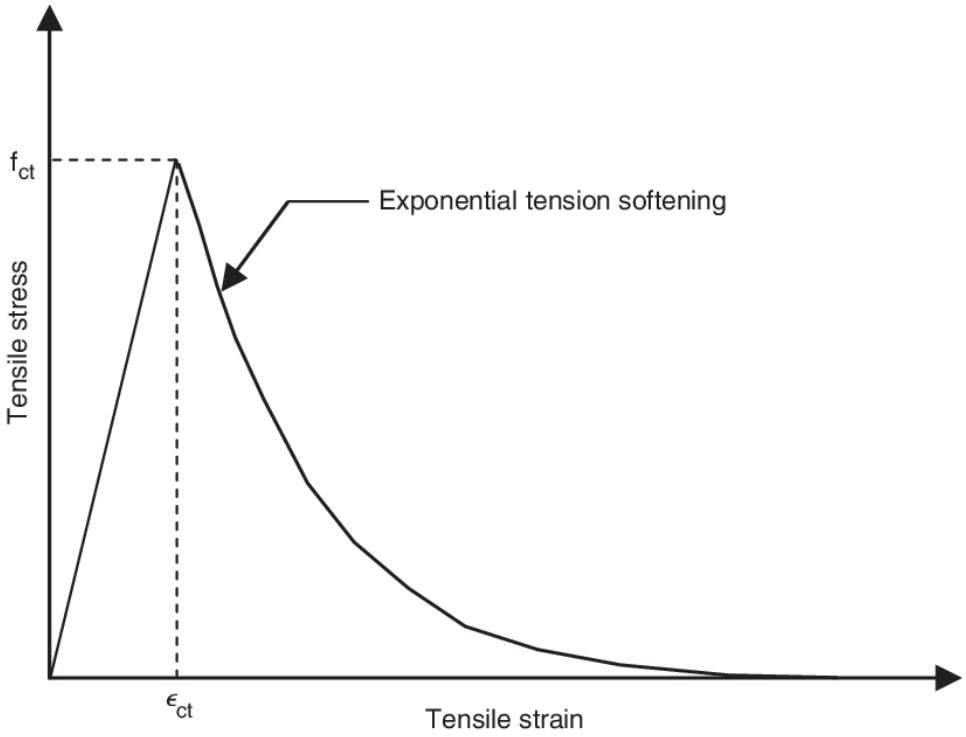

Source: Rafi et al. (2007).

In a steel or GFRP reinforced concrete member loaded gradually in pure tension, cracking will occur in one or more locations along the length of the member as the tensile stress exceeds the local tensile strength of the concrete. A primary crack will form and the stress crossing that crack is entirely transferred – by bond – to the reinforcement crossing the crack. In situ, primary cracks often form at internal stress raisors such as at the locations of transverse reinforcing bars. Between two consecutive primary cracks, the load carried by the reinforcement acting at the crack is transferred back into the concrete by bond. This phenomenon is known as *tension stiffening* and results in an increment of the stiffness of the member (Soltani et al., 2013). Assuming bond is sufficient to transfer stress, secondary concrete cracks will develop between primary cracks as the concrete tensile capacity is again exceeded. This process is described in greater depth in Section 2.1.4.3 in the context of the prism tests used in the present study.

2.1.2 Glass fiber-reinforced polymer bars

Glass Fiber Reinforced Polymer (GFRP) reinforcing bars consist of unidirectionally oriented glass fibers embedded in a vinyl-ester matrix. While S2-glass is typically used today, older GFRP bars used E-glass fibers. Early studies included the use of polyester matrices, although these were found to have significant durability concerns and are no longer permitted (ASTM D7957-22). Epoxy matrices are not known in practice.

GFRP bars exhibit some advantages compared to conventional steel bars that make them suitable for use as structural reinforcement: GFRP bars do not corrode (although they can degrade in certain environments) and present higher tensile strength. Tensile modulus, however, is on the order of 20% to 30% that of steel. In comparison to carbon FRP (CFRP) bars, GFRP is dominant in RC structures primarily because of its lower cost and availability of design guidance (e.g., ACI PRC 440.1-15) and, more recently, standards (ACI CODE 440.11-22).

While steel reinforcement exhibits ductile behaviour, GFRP is brittle. GFRP bars exhibit no plastic behaviour (yielding) prior to rupture and are characterized by a linear-elastic stress-strain relationship until failure. GFRP reinforcing bars are characterized by high tensile strength in the longitudinal direction of the fibers (ACI PRC 440.1, 2015). Due to internal shear lag effects, tensile strength of GFRP bars varies with diameter; for example, Faza and GangaRao (1993) observed a reduction of tensile strength of up to 40% as GFRP bar diameter increased from 9.5 mm to 22.2 mm for bars of three different manufactures. ASTM D7957-22 (2022) is the standard specification for GFRP reinforcing bars in the United States (and has been adopted elsewhere as it is the only extant standard specification). This standard prescribes minimum bar force (not strength) as a function of nominal diameter. For example, a 9.5 mm diameter bar has a prescribed minimum capacity of 59 kN (nominal stress = 831 MPa) whereas a 22.5 mm diameter bar has a minimum capacity of 241 kN (623 MPa), a 25% reduction in stress. ASTM D7957 also prescribes a minimum tension modulus of 45 GPa for GFRP reinforcing bars. The values prescribed by ASTM D7957 are minimum compliant values and most bars on the market exceed these. A new standard, ASTM 8505-23, now addresses GFRP and basalt FRP (BFRP) bars having a minimum modulus of 65 GPa and marginally greater tension capacities. Test

methods for determining tensile strength of a GFRP bar should conform to the methodology described in ASTM D7205-21 (2021), as referenced in ASTM D7957 and D8505.

The anisotropic behaviour of GFRP bars affects their shear strength and bond performance (Nanni, 2003). According to ACI PRC 440.1 (2015), GFRP bars exhibit little shear strength since this is governed by the polymer matrix behaviour. ASTM D7957-22 (2022) prescribes a minimum transverse shear strength of 131 MPa determined by the test method of ASTM D7617 (2017); ASTM D8505 prescribes 152 MPa. ASTM D7957 prescribes a minimum bond stress for GFRP bars of 7.6 MPa determined in accordance with ASTM D7913 whereas ASTM D8505 prescribes a minimum bond stress of 9.6 MPa. However, as will be established in the present work, these values are minimum standards appropriate for QA/QC (quality assurance/quality control), not appropriate values for use in design. Bond capacity of GFRP bars is affected by a number of factors including surface treatment, bar diameter, mechanical properties of the bar, compressive strength of concrete, the effects of confining reinforcement (if present), and concrete cover (Al-Dulaijan et al., 1996; Nanni et al., 1997; Bakis et al., 1998; Bank et al., 1998; Freimanis et al., 1998, Baena et al., 2009).

2.1.3 Mechanisms of reinforcing bar bond to concrete

Bond (or force transfer) mechanisms can be described in terms of: (i) chemical adhesion, in which the bond force is transferred by adhesion at the bar-concrete interface; (ii) frictional resistance of the interface against slip; and (iii) mechanical interlock arising from bearing of the surface deformations of the bar against the concrete (ACI PRC 408.3R-12) (Figure 2.2a). Adhesion and friction are rapidly overcome at very small strains. Mechanical interlock is the dominant mechanism of bond strength forming a resultant stress that can be decomposed into longitudinal and radial components (Figure 2.2b) (Platt and Harries, 2018). Thus, the geometry of the bar is an important parameter for determining bond behaviour.

Figure 2.2 – Transfer of forces from concrete to reinforcement.

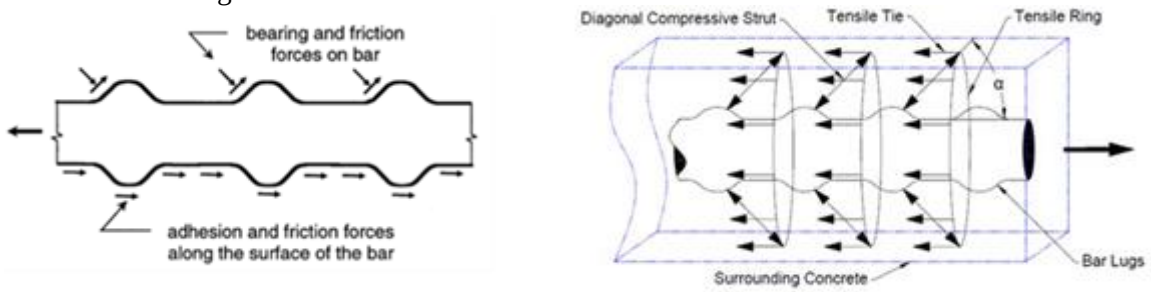

a) Bearing and frictional forces. b) Compressive and radial forces at angle α.
Source: (a) ACI PRC 408.3R-12; (b) Maekawa et al. (2003).

2.1.3.1 "Relative rib area" parameter

The so called "relative rib area" (R_r) is a ratio that can be used to quantify bar geometry as it relates to the mechanical component of bond between reinforcing bar and concrete. The "relative rib area", R_r, is calculated as (ACI PRC 408.3R-12):

$$R_r = \left(\frac{\delta}{s_r}\right) \times \left(1 - \frac{\sum gaps}{p}\right) = \left(\frac{\delta}{s_r}\right) \times \left(1 - \frac{\sum B_n}{360^o}\right) \quad (2.1)$$

where:

δ = average height of deformations;

s_r = average longitudinal spacing of deformations;

$\Sigma gaps$ = sum of the circumferential lengths of the gaps or chords between edges of deformations, plus the width of any continuous longitudinal protrusions used to represent the grade of the bar;

p = nominal perimeter of the bar;

ΣB_n = sum of the chord angles between edges of deformations relative to the bar axis inclusive of any continuous longitudinal protrusions used to represent the grade of the bar; thus, $\Sigma gaps/p = \Sigma B_n/360^o$.

Deformation geometry of A615 steel bars is shown in Figure 2.3.

Figure 2.3 – Definitions of A615 steel geometry.

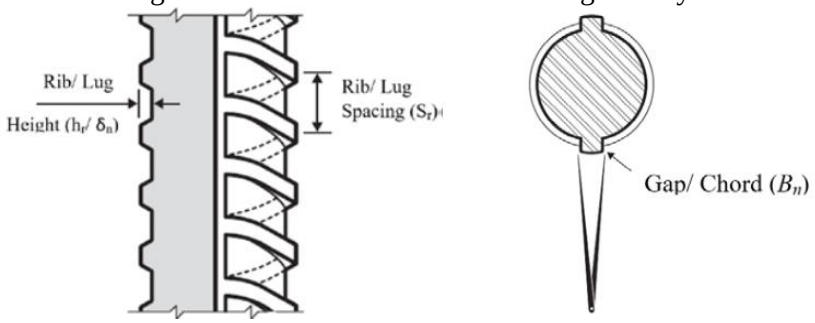

Source: Platt (2018).

Although R_r is not explicitly specified in ASTM A615, by combining the minimum ASTM A615 requirements for bar deformations, one infers a minimum required value of $R_r \geq 0.05$. It is important to recognize that ASTM A615 prescribes deformation geometry requirements intended for use with steel materials having a modulus of 200 GPa embedded in "conventional" concrete. Clark (1946, 1949), Soretz and Holzenbein (1979), Vos (1983), Choi et al. (1990), Lorrain et al. (2010), and Farshadfar et al. (2014) have demonstrated that steel reinforcing bars with $R_r \geq 0.05$ are considered to provide adequate bond performance with respect to the equations used for steel-reinforced concrete design. Hao et al. (2009) performed pull-out tests with bars of different rib geometries and suggested an optimal R_r equal to 0.06.

2.1.4 Assessing bond of reinforcing bars to concrete

2.1.4.1 Bond development in flexural member

In a reinforced concrete flexural member, the tension force in the bar is in equilibrium with the compression force in the concrete. The tension force is transferred to the bar from the surrounding concrete so that the tensile stress in the reinforcement varies over the length of the bar. Consider an incremental length, *dx*, of the simply-supported reinforced concrete beam shown in Figure 2.4.

Figure 2.4 – Simply-supported beam subject to flexure.

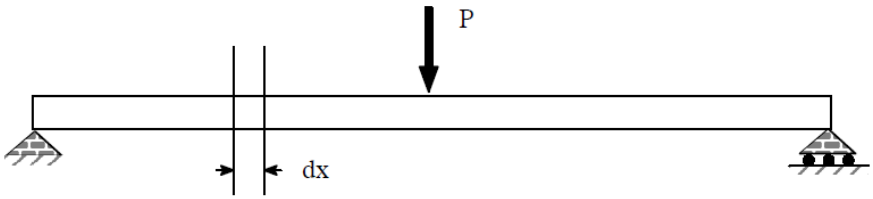

Source: Pezeshk (2008).

Figure 2.5 shows the equilibrium condition of the reinforced concrete element *dx* and reinforcing bar traversing this element.

Figure 2.5 – Equilibrium conditions.

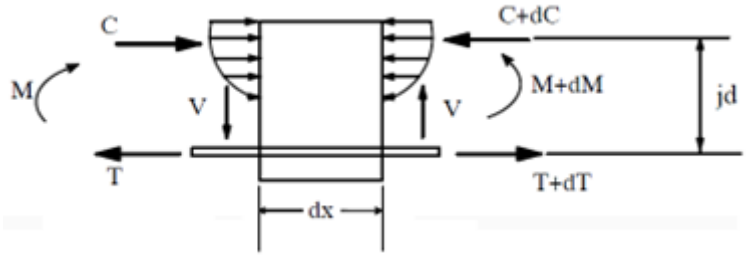

a) Concrete flexural member.

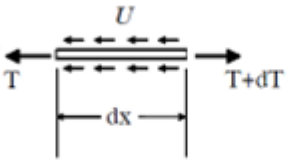

b) Reinforcing bar.
Source: Pezeshk (2008).

From Figure 2.5:

$$T = \frac{M}{jd} \tag{2.2a}$$

$$T + dT = \frac{M + dM}{jd} \rightarrow dT = \frac{dM}{jd} \tag{2.2b}$$

For equilibrium of the embedded bar (Figure 2.5b):

$$T + Udx = T + dT \tag{2.3a}$$

$$Udx = dT \tag{2.3b}$$

$$U = \frac{dT}{dx} = \frac{dM}{jd} \times \frac{1}{dx} \tag{2.3c}$$

$$\frac{dM}{dx} = V \rightarrow U = \frac{V}{jd} \tag{2.3d}$$

where:

U = bond force;

V = shear force; and

jd = moment arm between tension and compression force.

Equation [2.3d] is the "elastic cracked section equation" for flexural bond force and is applied to the tension bars in a concrete zone that is assumed to be fully cracked.

The average bond stress, τ, is calculated as:

$$\tau = \frac{U}{\sum_0} = \frac{V}{\sum_0 jd} \tag{2.4}$$

where $\sum_0$ is the sum of perimeters of the n bars at the section considered, e.g., $n\pi d_b$.

Considering a segment of a conventional beam subjected to pure bending shown in Figure 2.6: between adjacent cracks, the concrete resists tension (Figure 2.6a) transferred to it by the bond force acting along the interface concrete-reinforcement (Figure 2.6b); this reduces the tensile force in steel (Figure 2.6c). At a crack, the tensile force in steel reaches its maximum value (Equation 2.2a) and bond stress along the bar is zero (Figure 2.6d). The same behaviour is observed in a reinforcing bar embedded in a concrete prism subjected to tension, as described in Section 2.1.4.3.

Figure 2.6 – Variation of steel force and bond stress in reinforced concrete member subject to pure bending: (a) cracked concrete segment, (b) bond stress acting on reinforcing bar, (c) variation of tensile force in steel, and (d) variation of bond stresses along steel.

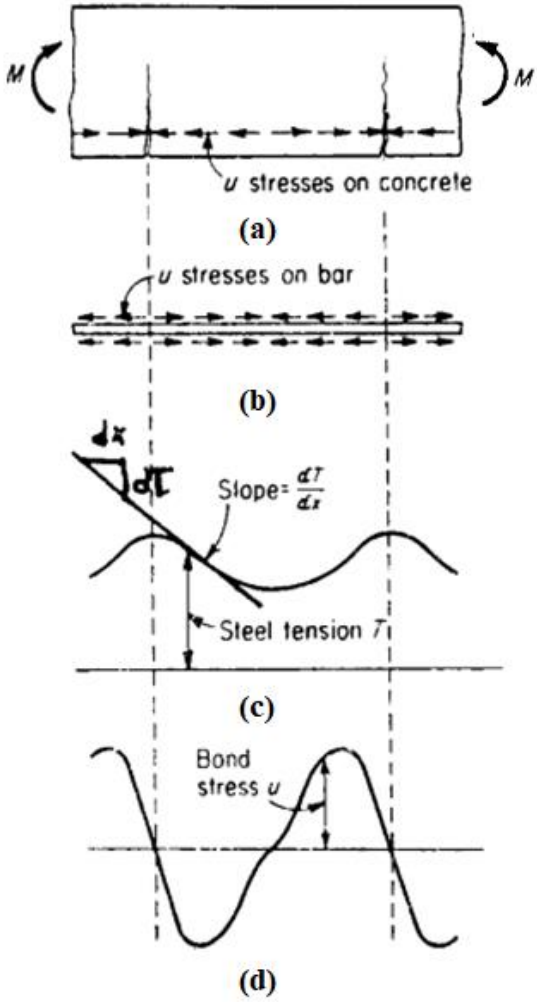

Source: Pezeshk (2008).

The approach described is idealized; in particular, a discrete crack location is shown in Figure 2.6 and bond is affected immediately adjacent to this. In situ, this is not exactly the case. There is a region of concrete to either side of the crack – typically assumed to extend approximately 5 bar diameters ($5d_b$) – to which more complex behaviour is attributed (CEB 1990). Additionally, bond stress varies between cracks and cannot be reliably determined experimentally. As a result, bond stress is most often described as an average value between adjacent cracks as given by Equation [2.4](2.4). The following sections describe means of assessing average bond stress.

2.1.4.2 Bond development in member subjected to direct pull-out

Pull-out tests are frequently used in the evaluation of bond characteristics of steel reinforcing bars. Although the stress conditions developed in the concrete pull-out specimen during the test do not reflect those in most reinforced concrete members, pull-out tests have been widely used due primarily to their ease of use and repeatability. Pull-out tests also offer an economical solution for evaluating the bond performance of reinforcing bars.

The ASTM D7913-14 (2020) pull-out test consists of a length of reinforcing bar cast into a concrete cube or cylinder with both ends exposed where one end is loaded in tension while the other is monitored for slip relative to the concrete (Figure 2.7).

Figure 2.7 – ASTM D7913-14 (2020) pull-out test set-up.

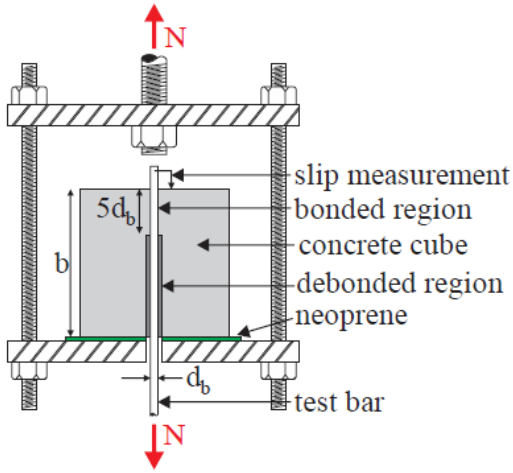

Source: Platt (2018).

The bonded length of the bar is set to only five bar diameters ($5d_b$). Such a short bonded length has been shown to overestimate the actual average bond stress for a corresponding full development length (Feldman and Bartlett 2005; Osofero et al. 2014). In addition, pull-out tests are less realistic because as the bar is loaded in tension, the surrounding concrete is placed entirely into compression; unlike a flexural member in actual service condition, whose reinforcing bar ***and*** adjacent concrete are in tension (see Section 2.1.4.1). The average bond stress over the $5d_b$ embedment, τ, is calculated as:

$$\tau = \frac{N}{\pi d_b l_b} = \frac{N}{5\pi {d_b}^2} \tag{2.5}$$

where:

N = tensile force applied to the bar;
d_b = nominal bar diameter;
l_b = bonded length ($5d_b$).

2.1.4.3 Bond development in tension member

When a reinforcing bar embedded in concrete is loaded in tension, the bar deformations engage the surrounding concrete and affect the rate at which force is transferred to the concrete along the length of the bar; this is the bond behaviour. Bond behaviour, in turn, affects the transverse crack spacing and therefore crack widths along the length of the bar. At a given bar elongation, improved bond will result in a greater number of cracks having a reduced spacing and smaller crack widths.

As shown schematically in Figure 2.8, bond stress can be idealized by loading in tension a single reinforcing bar embedded in a concrete prism (Figure 2.8a); critically, the external load is applied only to the bar. Conceptually, this arrangement is similar to the tension zone of a beam in flexure between two cracks: at each crack the reinforcing bar carries 100% of the load and the concrete immediately surrounding a reinforcing bar can be idealized as being in pure tension.

As the bar is loaded, a portion of the stress is transferred to the concrete through bond. Once the tensile stress in the concrete is exceeded, “primary” tensile cracks form in the concrete (Figure 2.8b). After cracking, the slip that occurs between the concrete and the reinforcing bar at the crack location relieves the tensile stress in the concrete adjacent to the crack. The transfer of tensile stress from bar to concrete between concrete cracks continues. As in a flexural member (see Section 2.1.4.1), at the crack locations the applied load is resisted entirely by the bar and the tensile stress in the bar (f_b) is:

$$f_b = \frac{N}{A_b} \tag{2.6}$$

where N is the applied load and A_b is the area of the embedded bar.

From the Hooke’s Law, the strain in the bar at the crack (ε_b) is:

$$\varepsilon_b = \frac{E_b}{f_b} \tag{2.7}$$

where E_b is the modulus of elasticity of the bar.

Figure 2.8 – Schematic representation of prism tension test and stresses in bar and concrete.

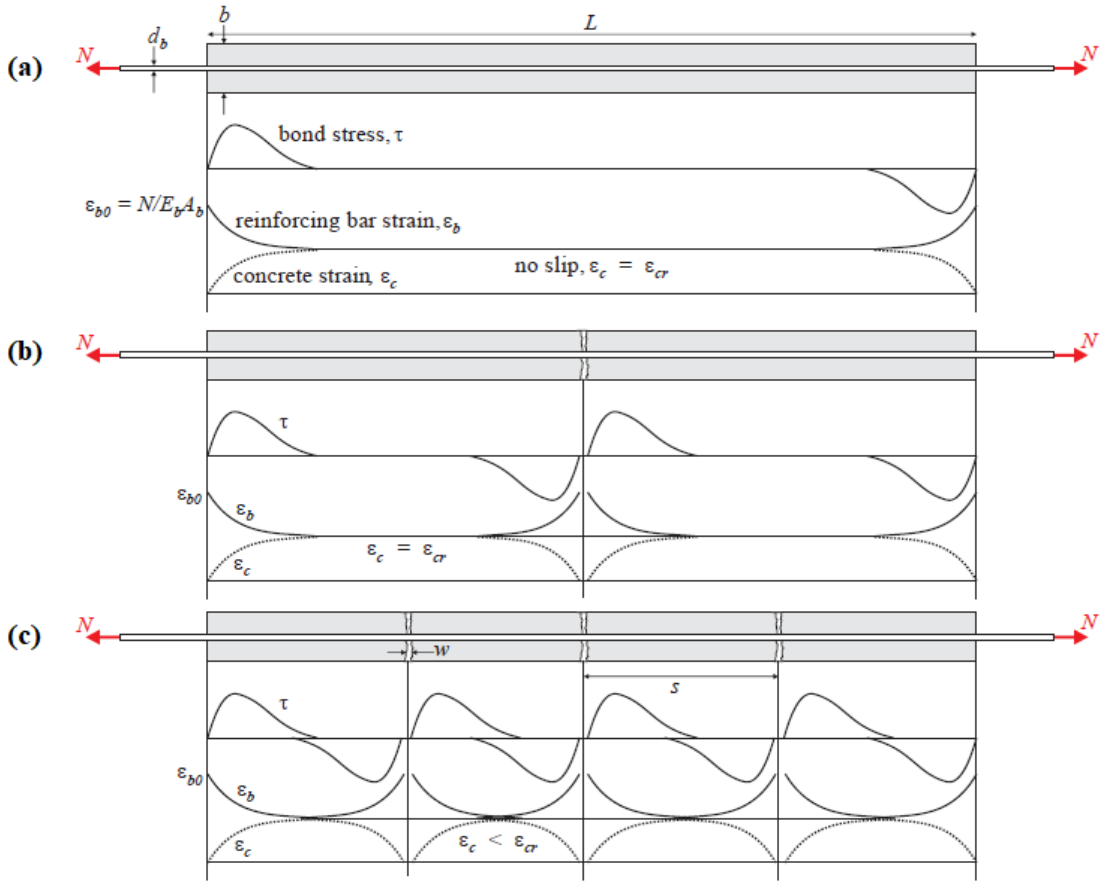

Source: Silva et al. (2022).

Between cracks – like at the initial condition – beginning at the crack location, a portion of the load is transferred to the concrete through bond and the process repeats between adjacent cracks (Figure 2.8c). No further cracks develop once the bond stress development between adjacent cracks is insufficient to develop the tensile capacity of the concrete (Reis et al., 1964). At this stage, additional load applied to the bar results in increases to existing crack widths and at higher loads some "secondary" cracks may appear.

The concrete between primary cracks carries less stress than its tensile capacity and the reinforced concrete prism response is stiffer than the response of the reinforcing bar alone. Since the concrete and reinforcement are composite, this results in lower bar strains between

the cracks than at cracks (Figure 2.8, parameter ε_b). At any load level, the difference in strain between the composite concrete member and the bar alone (at the cracks) is a measure referred to as “tension stiffening” which represents the contribution of the intact concrete between primary cracks to the member stiffness (Collins and Mitchell, 1997).

Considering two adjacent cracks in the schematic representation in Figure 2.9: at each crack, the stress in the concrete is zero and the concrete between the two primary cracks remains elastic while the load is resisted. At this point, the maximum concrete stress is less than the tensile strength of the concrete. The concrete tensile stress gradually increases as the distance from the cracks increases due to the bond stress developed between the bar and the concrete, reaching a maximum value between the two cracks. Bond stress is zero at the location of the cracks because the concrete and the bar are not in contact and is also zero midway between the adjacent cracks. Increased applied load that will result in a widening of existing cracks is associated with increasing slip.

Figure 2.9 – Schematic representation of concrete stress, bond stress, and slip between two primary cracks.

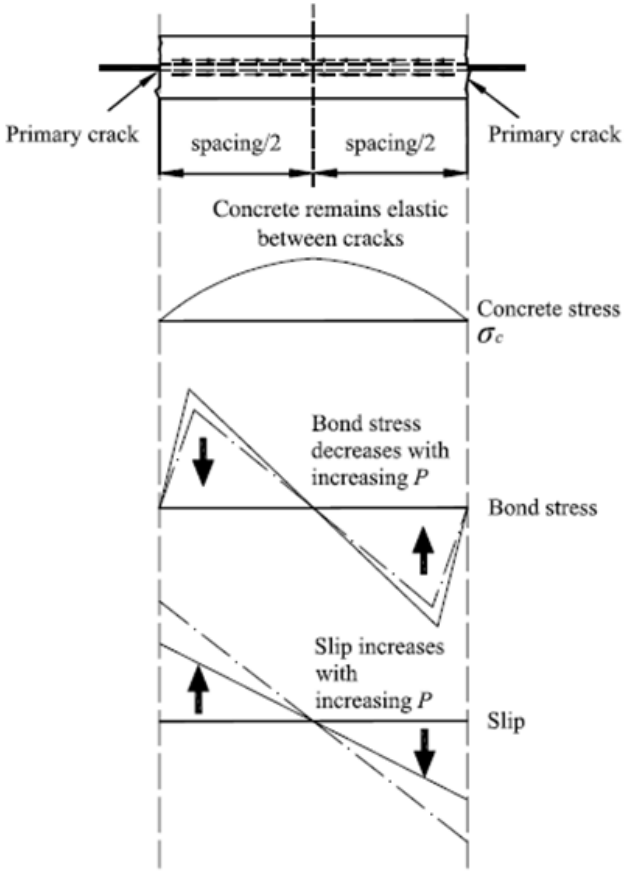

;

Source: Wu and Gilbert (2009).

The average bond stress, τ, from a prism tension test, therefore, can be calculated as:

$$\tau = \frac{A_c f_{ct}}{\pi d_b \frac{s_{avg}}{2}} \tag{2.8}$$

where:

A_c = area of concrete ($A_g - A_b$, where A_g is the gross area of concrete and A_b is the nominal area of the bar);

f_{ct} = tensile strength of concrete;

d_b = nominal bar diameter; and

s_{avg} = average crack spacing.

Once all cracks are established, for a given elongation of the reinforced concrete prism, the resulting deformation is the sum of the crack widths; strain between cracks is assumed to be

negligible. To ensure good serviceability, ductility and continued adequate bond, it is desirable that the member develop a large number of smaller cracks, thereby distributing strain along the member rather than concentrating it at a single dominant crack. Crack width is inversely proportional to bar modulus whereas crack spacing is inversely proportional to the stiffness of the initial bond-slip response – which can be obtained from ASTM D7913 tests described previously. Therefore, lower modulus of elasticity GFRP bars exhibit larger crack widths at a given applied tensile force, unless bond characteristics are improved proportionally. Average crack width, w_{avg}, can be estimated as:

$$w_{avg} = \frac{A_c f_{ct} s_{avg}}{E_b A_b} \tag{2.9}$$

where E_b and A_b are the modulus of elasticity and area of the embedded bar, respectively.

2.1.4.4 Discussion on the bond mechanisms

Bond between reinforcement and concrete can be assessed by means of a bond stress relationship as seen in Sections 2.1.4.1 – 2.1.4.3. Generally, the evaluation of such behaviour is performed through direct pull-out tests, that are characterized by a short embedment length ($5d_b$) and do not reflect the stress conditions of reinforced concrete members in practical construction. Unlike direct a pull-out test, a reinforced concrete prism in tension is suitable to predict stress values very close to those occurring in reinforced concrete members. Prism tests exhibit behaviour similar to that of the tension zone in flexural members.

2.2 Cracking predictions and bond-dependent coefficient

2.2.1 General design considerations

Serviceability Limit Sate (SLS) can be defined as satisfactory performance under service load conditions. Design guides for steel-reinforced concrete members are typically controlled by strength with the failure mode governed by steel yielding (ductile failure). The higher tensile strength and lower modulus of elasticity of GFRP reinforcing bars compared to conventional steel result in GFRP-RC elements governed often by serviceability requirements – allowable deflections and crack control. In GFRP-RC elements, concrete crushing failure (brittle failure) is more desirable compared to brittle rupture of FRP bars (Nanni, 1993; ACI CODE 440.11, 2022).

GFRP-reinforced concrete members have lower stiffness after cracking comparing to steel-RC elements having the same longitudinal reinforcement ratio; this results in wider crack widths. Although it is often argued that the corrosion-resistant property of GFRP bars enables a relaxation of crack width limits of GFRP-RC members, excessive crack width is undesirable for other serviceability criteria, such as aesthetic reasons or where water tightness is required (ACI CODE 440.11, 2022).

ACI PRC 440.1 (2015) recommendations propose limiting crack widths at SLS to the range of 0.40 to 0.70 mm for FRP-RC members in situations where crack widths are limited by aesthetic concerns. Likewise, Japan Society of Civil Engineers guidance (1997) establishes a maximum crack width equal to 0.50 mm considering aesthetics. Similarly, CAN/ CSA S6-06 guidelines adopt an allowable crack width of 0.50 mm for members subjected to aggressive environments and 0.70 mm for other members. For comparisons purposes, ACI 318 (2014) implies a maximum crack width that ranges approximately between 0.46 and 0.56 mm for steel-reinforced concrete structures.

Cracks can result from the shrinkage effect, flexural or direct tension stresses, or internal expansion resulting from the products of corrosion or deleterious aggregates. The embedded bars serve to control the opening of cracks once they appear. Serviceability checking of crack width requires evaluation of the bond behaviour. Since GFRP bars can be fabricated with

different types of surface treatments, the development of adequate bond is a critical aspect of the structural design. The combination of crack width and crack spacing is strongly influenced by, among other factors, bond properties of the reinforcing bar used (Salib and Abdel-Sayed, 2004; El-Nemr et al. 2013).

Cracking behaviour of GFRP-RC elements can be controlled in design through two means: (i) a direct method of calculating crack width and its comparison with acceptable limits (allowable crack width); or (ii) an indirect method of limiting bar spacing. ACI 318 (1999) replaced the previously prescribed '*z-factor*' (Gergely and Lutz, 1968) in which the cracking behaviour was assessed directly for steel-reinforced concrete members with an indirect approach, which controls flexural crack widths by prescribing a maximum reinforcing bar spacing. The latter method was calibrated, when developed, to the assumed crack widths used by the earlier approach.

Predictions for cracking behaviour of GFRP-reinforced concrete flexural members are generally based on similar formulations to that of conventional steel-RC members, although bond properties are different for steel and GFRP bars. In order to permit single design equations, bond capacity of GFRP bars is often normalized to that of steel bars using the so-called bond-dependent coefficient k_b. In another words, k_b is an adjustment factor that allows the designer to treat other materials or bar geometries in the same manner as conventional deformed steel bars. Since bond behaviour models of conventional steel bars in concrete are relatively well-known and considered to be adequate, steel bars conforming to the geometry requirements of ASTM A615 have k_b equal to 1.0. For other bars, a factor $1/k_b$ is applied in order to normalize bond properties to those of deformed steel bars. That is, when GFRP exhibits bond behaviour similar to that of deformed steel bars, k_b is equal to 1.0. For GFRP bars having bond behaviour inferior to steel bars, k_b is greater than 1.0 and for GFRP reinforcement presenting bond performance superior to steel, k_b is less than 1.0.

Many values of k_b are reported in literature in an attempt to encompass the different surface configurations of GFRP bars available, although there is no consensus. It is reported that k_b is influenced by factors such as bar type, bar diameter, concrete strength, and service stress level in the reinforcement (McCallum and Newhook, 2012; Noel and Soudki, 2013). The lack of

consensus on the nature of the k_b coefficient and its measurement makes it difficult to adequately model bond performance, and consequently, cracking behaviour of GFRP bars in concrete.

ISIS M-03 (2007) recommended k_b to be 1.2 in the absence of significant test data. The Canadian Highway Bridge Design Code CAN/ CSA S6-06 prescribed a bond coefficient equal to 0.8 and 1.0 for sand-coated and deformed FRP bars, respectively. ACI PRC 440.1R-01 (2001) recommended values of k_b by Gao et al. (1998) equal to 0.71, 1.00, and 1.83 for three types of GFRP bars and 1.2 for deformed FRP bars in the absence of experimental data. Bakis et al. (2006) recommended k_b values ranging from 0.60 to 1.72 – excluding smooth bars and grids – with a mean value of 1.10; this latter study is cited in ACI PRC 440.1-06 and -15 (2006, 2015). ACI PRC 440.1-15 (2015) recommends that in the event k_b is not known from experimental data, a value of 1.4 should be assumed. ACI CODE 440.11-22 (2022) specifies a value of k_b = 1.2 for all GFRP bars.

2.2.2 Equations for cracking control of GFRP-reinforced concrete members

2.2.2.1 Modified Gergely-Lutz equation

The Gergely-Lutz equation (1968) modified by the addition of the corrective coefficient k_b to account the bond behaviour of FRP bars was first introduced by ACI PRC 440.1 (2001) to estimate the crack width of FRP-RC members as:

$$w = 2.2\frac{f_s}{E_b}\beta k_b \sqrt[3]{d_c A} \quad \text{[SI units]} \tag{2.10}$$

where:

w = maximum crack width at tension face;
f_s = stress in reinforcement at service load;
E_b = modulus of elasticity of bar;
β = ratio of the distance from the neutral axis to extreme tension fiber to the distance from the neutral axis to the center of the tensile reinforcement;
k_b = bond-dependent coefficient; in the absence of experimental data, ACI PRC 440.1 (2001) recommended a value of k_b = 1.2;
d_c = thickness of concrete cover measured to from extreme tension fiber to center of bar; and

A = effective tension area of concrete surrounding the flexural tension reinforcement and having the same centroid as that reinforcement, divided by the number of bars.

2.2.2.2 Modified Frosch equation

The Canadian Highway Bridge Design Code, CHBDC (CSA/S6-06, 2006) and ACI PRC 440.1 (2006) adopted the Frosch equation (1999) adding the bond coefficient k_b to describe the bond behaviour between FRP bars and the surrounding concrete. The maximum crack width for FRP-RC members can be calculated as:

$$w = 2\frac{f_s}{E_b}\beta k_b\sqrt{{d_c}^2 + \left(\frac{s}{2}\right)^2} \tag{2.11}$$

where s is the longitudinal bar spacing.

In the absence of experimental data, a value k_b = 1.4 was recommended by (ACI PRC 440.1 2006).

2.2.2.3 Indirect flexural crack control approach

The '*z-factor*' or Gergely-Lutz (1968) approach of ***directly*** assessing cracking behaviour of steel-reinforced concrete beams was abandoned by ACI 318 in 1999 in favor of a simplified version of the alternative approach proposed by Frosch (1999) which prescribed spacing limits for longitudinal reinforcing steel, thereby ***indirectly*** controlling crack width. Rearranging the original proposed equation by Frosch to solve for the maximum permitted bar spacing, s:

$$s = 2\sqrt{\left(\frac{wE_b}{2f_s\beta}\right)^2 - d_c^2} \tag{2.12}$$

where $\beta \approx 1.0 + 0.08d_c$.

Equation [2.12] is simplified for steel reinforcing bars (E_s = 200,000 MPa) in ACI 318 by assuming crack width, w, equal to 0.45 mm, which was also the value assumed for interior exposure conditions when applying the ACI '*z-factor*' approach prior to 1999[1]:

$$s = 380\left(\frac{280}{f_s}\right) - 2.5c_c \leq 300\left(\frac{280}{f_s}\right) \text{ (f_s in MPa and c_c in mm)} \tag{2.13}$$

where c_c is the concrete clear cover.

Equation [2.13] may be recalibrated for reinforcing bar modulus, E_b, the crack width for which it is calibrated, w, and the performance of the bond relative to that of steel bars using the bond coefficient, k_b:

$$s = 380\left(\frac{280}{f_s}\right)\left(\frac{E_b}{200{,}000}\right)\left(\frac{w}{0.45}\right)\frac{1}{k_b} - 2.5c_c \leq 300\left(\frac{280}{f_s}\right)\left(\frac{E_b}{200{,}000}\right)\left(\frac{w}{0.45}\right)\frac{1}{k_b} \tag{2.15}$$

which is presented in ACI PRC 440.1 (2015) for FRP bars as:

$$s = 1.15\frac{E_b\, w}{f_s\, k_b} - 2.5c_c \leq 0.92\frac{E_b\, w}{f_s\, k_b} \tag{2.16}$$

Thus, the relationship between acceptable crack width, w, reinforcing bar strain, $\varepsilon = f_s/E$, and bar spacing, s, required to control cracking is demonstrated in a relatively simple format consistent with ACI practice. The relationship is independent of material, only assuming linear (elastic) behaviour is present.

2.2.3 Review of studies on bond-dependent coefficient

Lee et al. (2010) tested 16 beams reinforced with FRP or steel bars of different diameters. The specimens were tested under four-point bending and were fabricated with plain and fiber-reinforced concrete (FRC). They observed no clear correlation between bond-dependent

[1] In 1999, Frosch equation was calibrated using a crack width of 0.40 mm. Due to the recalibration of ACI load factors in 2002, the assumed service load stress, f_s, was increased from 0.60f_y to 0.67f_y, effectively changing the *de facto* assumed crack width: 0.40 (0.67/ 0.60) = 0.45 mm.

coefficient, k_b, and bar size or reinforcement ratio for a given bar type; on the other hand, the addition of polypropylene fibers to the concrete led to reduced values of k_b (improved bond) as would be expected. Analysing FRC beams, the k_b value decreased between 45 to 55% for the GFRP-reinforced beams, 45 to 75% for the CFRP-reinforced beams, and 1 to 15% for the steel reinforced beams, when compared to plain concrete.

Kassem et al. (2011) conducted 24 tests of RC beams loaded by four-point bending including two control beams reinforced with conventional steel. The dimensions of the beams were 200 mm width x 300 mm height x 3,300 mm length. Two types of GFRP reinforcement, sand-coated and ribbed-deformed bars, were used. Bond factor, k_b, was determined as the ratio of experimental to calculated crack width. The researchers estimated k_b by the modified Frosch equation (Equation 2.11) using the maximum crack width observed during tests at a service load equal to 30% of the nominal moment (M_n). The bond coefficient, k_b, ranged between 0.86 and 1.32. The results indicated that Equation [2.11] predicts crack width for FRP-reinforced beams very well. Additionally, Kassem et al. concluded that bar diameter, surface configuration and mechanical properties of the same type of bar had little effect on k_b values.

Ahmed et al. (2013) carried out an experimental investigation to evaluate the bond-dependent coefficient, k_b, of helically-deformed GFRP reinforcing bars. A total of four concrete beams measuring 200 mm wide x 300 mm deep x 3,100 mm long were constructed and tested in four-point bending following CSA S806 (2012) Annex S guidelines. The investigated parameter of this study was the diameter of the bars: 12, 16, 20, and 25 mm. The predicted k_b was calculated from the measured crack widths and strains at $0.30M_n$ and the measurements were taken based on the first three flexural cracks in the constant moment span. The calculated k_b coefficients ranged from 0.71 to 1.03 with a mean value of 0.90 and coefficient of variation (COV) equal to 0.16, which agreed with the recommendations of CSA S6-06 that set k_b equal to 1.0 for deformed FRP bars.

El-Nemr et al. (2013) tested 12 concrete beams reinforced with GFRP bars and another two reinforced with steel bars serving as control specimens. The specimens measured 200 mm wide x 400 mm deep x 4,250 mm long and were tested to failure in four-point bending over a clear span of 3,750 mm. The beams were reinforced with sand-coated and helically-grooved GFRP

bars, and were fabricated with normal- and high-strength concretes (NSC and HSC, respectively). The k_b coefficients were calculated using the experimental results and compared to the target values suggested by ACI PRC 440.1 (2006) and ISIS M-03 (2007), 1.4 and 1.2, respectively. The average k_b for sand-coated bars – 0.91 (Equation 2.10) and 1.15 (Equation 2.11) – indicated that the values recommended by both design guidelines appeared conservative. El-Nemr et al. observed no clear relationship for k_b variation for NSC and HSC beams.

McCallum (2013) performed an extensive experimental investigation to analyze the bond-dependent coefficient of GFRP-RC beams and slabs. Tested specimens included 14 beams, measuring 200 mm width x 300 mm height x 3,000 mm length, and 9 slabs, 600 mm wide x 3,000 mm long with different thicknesses – 150, 200 and 225 mm. The beams were tested in four-point bending while the slabs were loaded under three-point bending. Two types of GFRP bars were used: smooth sand-coated bars and deformed sand-coated bars. The beams were designed in order to analyze the effect of concrete cover and fiber addition on the concrete mix as well as the applicability of k_b equation to these variations. In turn, the slabs specimens were designed primarily to examine the effect of bar spacing and slab thickness on crack width and k_b by maintaining approximately the same reinforcement ratio in each specimen. Groups of specimens were assembled and compared depending on the bar diameter used. The results indicated that k_b varied according to service stress level. Taking a stress-level approach, k_b was calculated using the modified Frosch equation (Equation 2.11) and the crack widths were measured during the tests. Stresses ranging from 15 to 30% of the ultimate guaranteed tensile strength (f_u) were chosen to demonstrate the variability of the results. The coefficient of variation for the predicted k_b values decreased from 0.52 to 0.39 as data was calculated at bar stress that increased from $0.15f_u$ and $0.25f_u$. Little additional change in variation was observed for a service level increased from $0.25f_u$ (COV = 0.39) to $0.30f_u$ (COV = 0.36). At $0.30f_u$, the reported average values of k_b for smooth sand-coated and deformed sand-coated bars were 1.06 and 0.64, respectively.

El-Nemr et al. (2016) investigated the influence of FRP bar type (GFRP and CFRP), diameter and concrete type on k_b values. The study included 16 beams measuring 200 mm wide x 400 mm deep x 4,250 mm long tested under four-point bending and reinforced with sand-coated

GFRP and CFRP bars, and helically-grooved GFRP bars. The specimens were fabricated using normal- and high-strength concretes. The results demonstrated that: (i) k_b values varied with FRP bar diameter, although no trend was observed; (ii) increasing the concrete strength resulted in reduced k_b values for the same bar size and surface treatments, independent of surface configuration; and (iii) sand-coated GFRP bars presented smaller k_b coefficients than the helically-grooved GFRP bars, confirming that the surface configuration also affects the bond coefficient. At $0.30M_n$, the range of k_b values reported in this study varied from 0.60 to 1.50.

Morcous and Henin (2018) conducted an experimental investigation consisting of six beams reinforced with helically wrapped sand-coated GFRP bars. The dimensions of the beams were 203 mm wide x 304 mm deep x 3,050 mm long and the specimens were assessed using four-point bending. Three different diameters of GFRP reinforcing bars were used: 13, 19, and 25 mm. The average value of k_b increased with bar diameter: k_b = 0.92 for 13 mm bars, 1.08 for 19 mm bars, and 1.15 for 25 mm bars.

Tran et al. (2018) performed an investigation to predict k_b for different GFRP bar diameters in normal strength concrete. To this end, six concrete-reinforced beams measuring 200 mm width x 300 mm height x 3,000 mm length were constructed and tested under four-point bending. The beams were reinforced with GFRP bars of different diameters having helically wrapped surface configuration. They concluded that k_b values varied with GFRP bar diameter, but the results did not show a consistent trend. Tran et al. report k_b = 0.97 for 12.4 mm diameter bars, 1.15 for 14.8 mm bars, and 1.08 for 18.3 mm bars.

Abdelkarim et al. (2019) tested eight GFRP-RC beams fabricated with NSC and HSC having compressive strength of 35 MPa and 65 MPa, respectively. Four bar sizes – 12, 16, 20, and 25 mm – and two clear concrete covers – 38 and 50 mm – were considered. The beams were reinforced with deformed GFRP bars and tested under four-point bending. The tests followed the CSA S806 (2012) Annex S guidelines. The dimensions of the specimens were 200 mm width x 300 mm thickness x 3,100 length. The results showed that the average k_b of the HSC beams was lower than that of the NSC beams: 0.96 and 1.09, respectively. In addition, it was reported that k_b varied with bar diameter and clear cover: contrary to results reported by

Morcous and Henin (2018) and Shang (2019), k_b decreased with increasing GFRP bar diameter and decreasing concrete cover.

Shang (2019) conducted an experimental study evaluating the bond-dependent coefficient in relation to the influence of bar configurations, bar diameter and concrete cover. To this end, nine GFRP-RC beams were constructed with dimensions of 200 mm wide x 300 mm deep x 2,800 mm long and tested under four-point bending. Sand-coated and deformed/ribbed GFRP bars were used. The analysis of the experimental results showed that sand-coated GFRP bars presented smaller average k_b values (k_b = 0.84) compared to deformed/ribbed bars (k_b = 0.93), indicating better bond behaviour of the sand-coated bars. Increasing the concrete cover from 38 to 50 mm led to a reduction of the average k_b for GFRP bars regardless of bar treatment. Finally, the results indicated that for increasing the bar diameter – maintaining the same concrete cover – the k_b coefficient increased for both sand-coated and deformed/ribbed bars.

The studies described in this section are adopted in the parametric study presented in Chapter 3; additional details on each study are found in Chapter 3.

2.3 Summary of the chapter

In this chapter, the behaviour of concrete in tension and some of the main mechanical properties of GFRP bars has been presented. GFRP bars present higher longitudinal tensile strength compared to that of steel, linear stress-strain behaviour under tension until rupture and poor shear strength. In particular, GFRP bars exhibit low modulus of elasticity, resulting in large strains that lead to larger concrete crack widths. As a result, serviceability requirements often govern the design of GFRP-RC elements. A better understanding of the bond between GFRP bars and the surrounding concrete is a key feature for estimating crack width correctly. Equations available in North American codes for cracking predictions were also reported in this chapter.

Bond development in different concrete members was described. The stress conditions developed in the concrete specimen in the direct pull-out test are rarely encountered in practice and the bond stress is estimated for a short embedded length of five bar diameters ($5d_b$). Nonetheless, the pull-out test is felt to be a valid basis of comparing bars having different parameters (a so-called "A-B" test). The non-standard prism test was shown to capture *in situ* bond behaviour more realistically.

Despite the differences in bond properties of GFRP and steel bars, the design approach for GFRP-RC members is based on similar procedures used for steel-reinforced concrete members. To account for differences in bond behaviour, a bond-dependent coefficient, k_b, is adopted to describe the GFRP bar performance relative to the well-established bond behaviour of conventional steel bars. A range of values of k_b is reported in literature, although the lack of consensus of a k_b coefficient makes it difficult to permit its use in design equations without knowing *a priori* the bar type to be used for which k_b is explicitly determined by testing.

A summary of available studies that aimed to predict k_b from experimental tests was presented. In general, larger diameter bars have a larger k_b value indicating poorer bond although this conclusion was not universal. The k_b parameter is generally decreased (improved bond) with higher strength concrete, the inclusion of fibers in the concrete, and increased concrete cover.

In general, sand-coated GFRP bars exhibit lower k_b values (better bond behaviour) than deformed bars.

3

PARAMETRIC STUDY

This chapter provides a detailed quantitative and qualitative study performed based on published works that predicted the bond-dependent coefficient, k_b, from experimental tests. A complete and careful up-to-date review of these studies was performed in order to analyze the influence of different parameters in the estimation of k_b and is presented herein.

3.1 Experimental database

Tests of a large number of GFRP-reinforced concrete beams and slabs have been conducted in order to predict the bond-dependent coefficient, k_b, from experimental tests. An extensive database was assembled in order to analyze the influence of different parameters in the estimation of k_b, namely: bar diameter (d_b), clear cover (c), bar surface treatment, concrete strength (f'_c), and service load level. The database includes experimental results from 19 studies, designated in this chapter as follows:

a = Shang (2019);
b = Abdelkarim et al. (2019);
c = Tran et al. (2018);
d = Morcous and Henin (2018);
e = El-Nemr et al. (2016);
f = Barris et al. (2016);
g = Noel and Soudki (2013);
h = McCallum (2013);
i = El-Nemr et al. (2013);
j = Barris et al. (2013);
k = Ahmed et al. (2013);
l = Kassem et al. (2011);
m = Lee et al. (2010);
n = Zou and Huckelbridge (2007);
o = Kassem (2004);
p = El-Salakawy and Benmokrane (2004);
q = Newhook (2000);
r = Thériault and Benmokrane (1998);
s = Masmoudi et al. (1998).

Based on this review, Figure 3.1 shows that the number of experimental tests of GFRP-reinforced concrete members for estimation of k_b has increased in the last decade. The age of tests can be important since GFRP reinforcing bars have evolved considerably and should, since 2017, be compliant with ASTM D7957.

Figure 3.1 – Number of specimens tested *versus* year of publication work.

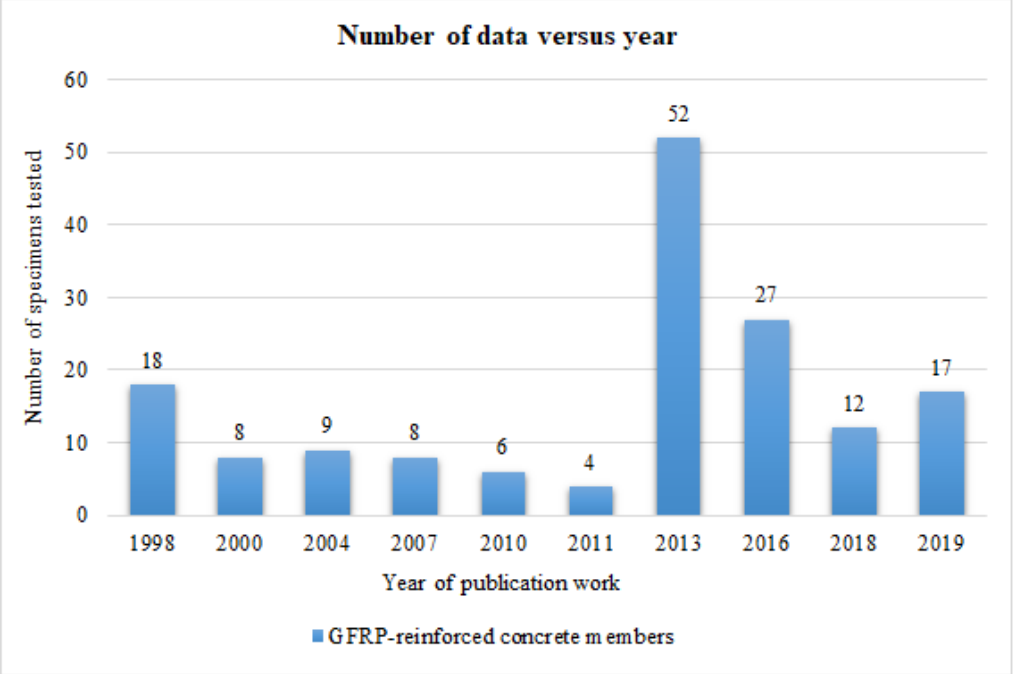

Source: author.

Most of the experimental predictions of k_b were based on four-point bending tests and some of the works followed the provisions of Annex S of CAN/ CSA S806-12 to determine k_b. The specimens were fabricated with normal- (NSC) and high strength concrete (HSC) with compressive strength values ranging from 25 to 97 MPa. This database includes GFRP-reinforced beams and slabs reinforced longitudinally with GFRP as bottom (tension) reinforcement and steel bars as top reinforcement. Beam specimens were reinforced with stirrups in their shear spans to prevent shear failure and had no confinement in the constant moment region to avoid affecting the cracking behaviour. Members were designed to be under- and over-reinforced.

Details of the specimens in the compiled database are present in Appendix A.

This study is carried out in two stages: the first considered only behaviour at a specific crack width, w, equal to 0.70 mm, the presumed crack width limit at the Service Limit State. For those specimens for which data at w = 0.70 mm is not available, the same analysis was conducted at a crack width that could be assessed for all specimens in a study.

3.1.1 Assumptions of experimental database analysis

The first part of the analysis is based on the following criteria:

(i) the maximum allowable crack width under service loads reported by guidelines for GFRP-reinforced concrete members is 0.70 mm (see Section 2.2.1). Thus, the bond coefficient, k_b, should be determined using data corresponding to a crack width of 0.70 mm;

(ii) bond coefficients reported by the investigators using both Gergely-Lutz (Equation 2.10) and Frosch (Equation 2.11) equations are reported in Table 3.1 (labelled columns 2 and 3). Lee et al. (2010) and Zou and Huckelbridge (2007) (references m and n in Table 3.1) estimated k_b using only Equation [2.10]; in these cases, values of k_b using a correlation between Equations [2.10] and [2.11] were calculated in this work from the data presented at a crack width equal to 0.70 mm and are reported in column 3;

(iii) in cases of specimens in which k_b is reported for a crack width other than 0.70 mm but for which data at w = 0.70 mm is available, the author made the calculation for k_b at w = 0.70 mm using Equation [2.11] (column 5). The deterministic procedure to back-calculate k_b based on Equation [2.11] is shown in Figure 3.2 and an example of the detailed calculation is presented in Appendix B.

(iv) for studies in which insufficient available data to permit the calculation of k_b for a crack opening of 0.70 mm is presented, the same calculation of k_b is made for a crack width that can be uniformly assessed for all specimens reported in the study (column 5). The crack width is reported in Table 3.1 as a value other than 0.70 in column 1; and

(v) the tensile stress in the reinforcing bars, f_f, is reported for bars comprising the extreme tension layer of reinforcement (column 4).

Figure 3.2 – Flowchart of deterministic procedure to back calculate k_b based on Frosch equation.

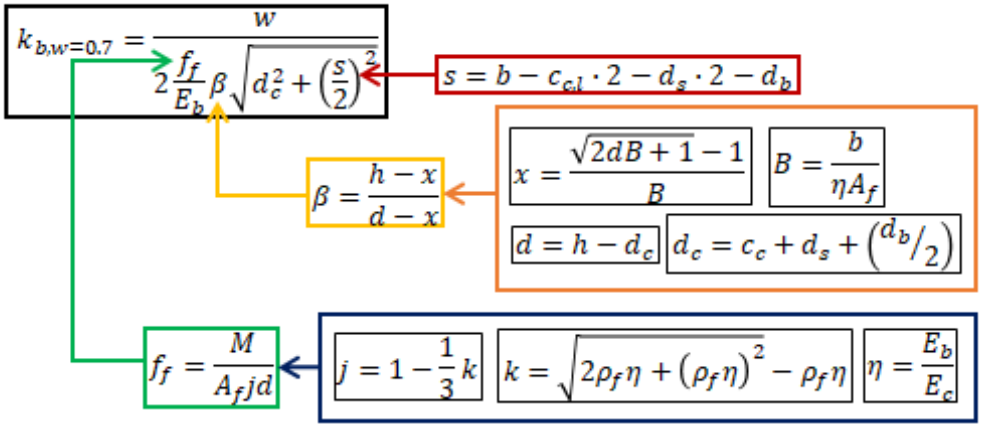

A_f = total area of GFRP reinforcement;
b = width of the section;
c_c = clear cover;
$c_{c,l}$ = lateral clear cover;
d = depth of the section;
d_b = bar diameter;
d_c = thickness of concrete cover measured from extreme tension fiber to center of bar
d_s = thickness of stirrup;
E_b = modulus of elasticity of GFRP bar;
E_c = modulus of elasticity of concrete;
w = crack width equal to 0.70 mm;
f_f = tensile stress in GFRP reinforcement;
h = height of the section;
jd = moment arm between tension and compression force;
M = applied moment corresponding to crack width of 0.70 mm;
x = depth of the neutral axis;
β = ratio of the distance from the neutral axis of the member to the extreme tension fiber to the distance from the neutral axis to the centroid of the tensile reinforcement;
η = modular ratio;
ρ_f = reinforcement ratio.

Source: author.

Table 3.1 shows results for k_b for both analysis – 0.70 mm fixed crack width and variable crack width (those for which k_b is not 0.70 mm) – for the specimens of the experimental database.

Table 3.1 – Summary of the results for k_b.

Reference (a)	Specimen nomenclature	Properties					1	2	3	4	5
								k_b reported by authors			
		f'_c (MPa) (b)	d (mm) (c)	d_b (mm) (d)	c_c (mm) (e)	Surface treatment (f)	w (mm)	Gergely-Lutz Equation [2.10]	Frosch Equation [2.11]	Calculated or reported f_f in extreme tension layer (MPa)	k_b calculated in present study for w (column 1)
a	S16-C38-I	46.4	254	15.9	26.7	iv	0.70	**0.50**	**0.80**	323	-
a	S16-C50-I	46.4	254	15.9	26.7	iv	0.70	**0.50**	**0.70**	369	-
a	S19-C50-I	46.4	253	19.1	26.7	iv	0.70	**0.50**	**0.80**	319	-
a	S22-C50-I	40.5	251	22.2	26.7	iv	0.70	**0.60**	**0.90**	292	-
a	R16-C38-I	43.6	254	16	26.7	iv	0.70	**0.80**	**1.20**	199	-
a	R16-C50-I	43.6	254	16	26.7	iii	0.70	**0.50**	**0.70**	341	-
a	R19-C50-I	43.6	252	20	26.7	iii	0.70	**0.50**	**0.80**	313	-
a	S16-C38-II	40.5	254	15.9	25.3	iv	0.70	**0.70**	**1.00**	262	-
a	R16-C38-II	40.5	254	16	25.3	iii	0.70	**0.70**	**1.10**	220	-
b	B1-35-12	34.1	246	12	38	v	0.70	-	1.46	251	1.02
b	B2-35-16	34.1	244	16	38	v	0.70	-	0.78	273	0.89
b	B3-35-20	34.1	230	20	50	v	0.70	-	1.22	246	0.92
b	B4-35-25	34.1	228	25	50	v	0.70	-	0.89	212	0.96
b	B5-65-12	67.5	246	12	38	v	0.70	-	1.10	374	0.69
b	B6-65-16	67.5	244	16	38	v	0.70	-	1.27	375	0.65
b	B7-65-20	67.5	230	20	50	v	0.70	-	0.73	418	0.55
b	B8-65-25	67.5	228	25	50	v	0.70	-	0.72	368	0.56
c	2D14-1	40.8	253	14	32	ii	0.70	-	1.09	165	-
c	2D14-2	40.8	253	14	32	ii	0.70	-	0.84	213	-
c	2D16-1	40.8	252	16	32	ii	0.70	-	1.22	151	-
c	2D16-2	40.8	252	16	32	ii	0.70	-	1.08	169	-
c	2D20-1	40.8	240	20	42	ii	0.70	-	1.06	163	-
c	2D20-2	40.8	240	20	42	ii	0.70	-	1.10	156	-
d	B2#4-1	45	250	13	38	i	0.70	-	0.85	267	-
d	B2#4-2	45	250	13	38	i	0.70	-	0.99	229	-
d	B2#6-1	45	234	19	51	i	0.70	-	0.86	243	-
d	B2#6-2	45	234	19	51	i	0.70	-	1.31	159	-
d	B2#8-1	45	231	25	51	i	0.70	-	1.01	206	-
d	B2#8-2	45	231	25	51	i	0.70	-	1.29	162	-
e	N2#15G1	38.9	343	15	40	iv	0.70	**0.70**	**0.80**	225	-
e	N2#15G3	33.8	343	15	40	iii	0.70	**1.00**	**1.10**	194	-
e	N3#20G1	42.1	340	20	40	iv	0.70	**1.00**	**1.40**	148	-
e	N2#22G1	38.9	339	22	40	iv	0.70	**0.50**	**0.70**	234	-
e	N3#20G2	48.1	340	20	40	iv	0.70	**1.00**	**1.30**	176	-
e	N2#25G1	48.1	338	25	40	iv	0.70	**0.50**	**0.70**	264	-
e	N2#25G2	48.1	338	25	40	iv	0.70	**0.70**	**0.80**	287	-
e	N2#25G3	33.8	338	25	40	iii	0.70	**1.10**	**1.40**	149	-
e	H3#20G2	81.5	340	20	40	iv	0.70	**0.70**	**1.00**	227	-
e	H2#25G1	81.5	338	25	40	iv	0.70	**0.60**	**0.80**	232	-
e	H2#25G2	81.5	338	25	40	iv	0.70	**0.40**	**0.50**	461	-
e	H2#25G3	76.5	338	25	40	iii	0.70	**1.00**	**1.20**	175	-
f	G1-212-25-150	33.1	203	12	25	iii	0.70	**1.21**	**1.20**	518	0.55
f	G1-212-40-150	33.1	188	12	40	iii	0.70	**1.21**	**1.20**	660	0.40

Reference (a)	Specimen nomenclature	Properties					1	2	3	4	5
								k_b reported by authors			
		f'_c (MPa) (b)	d (mm) (c)	d_b (mm) (d)	c_c (mm) (e)	Surface treatment (f)	w (mm)	Gergely-Lutz Equation [2.10]	Frosch Equation [2.11]	Calculated or reported f_f in extreme tension layer (MPa)	k_b calculated in present study for w (column 1)
f	G2-213-25-150	34.3	203	13	25	i	0.70	**1.31**	**1.35**	519	0.39
f	G2-213-25-000	34.3	203	13	25	i	0.70	**1.31**	**1.35**	563	0.36
f	G2-310-25-000	34.3	204	10	25	i	0.70	**1.31**	**1.35**	569	0.36
f	G2-213-25-150G	34.3	203	13	25	i	0.70	**1.31**	**1.35**	519	0.39
f	G1-216-25-150	33.1	201	16	25	iii	0.10	-	-	150	0.29
f	G1-216-25-250	33.1	201	16	25	iii	0.10	-	-	150	0.29
f	G1-216-25-000	33.1	201	16	25	iii	0.10	-	-	177	0.24
f	G1-212-25-150	33.1	203	12	25	iii	0.10	-	-	207	0.20
f	G1-212-40-150	33.1	188	12	40	iii	0.10	-	-	257	0.15
f	G1-212-55-150	34.3	173	12	55	i	0.10	-	-	244	0.13
f	G2-213-25-150	34.3	203	13	25	i	0.10	-	-	176	0.17
f	G2-213-25-000	34.3	203	13	25	i	0.10	-	-	185	0.16
f	G2-310-25-000	34.3	204	10	25	i	0.10	-	-	225	0.13
f	G2-213-25-150G	34.3	203	13	25	i	0.10	-	-	185	0.16
f	G2-213-25-250G	34.3	203	13	25	i	0.10	-	-	211	0.14
f	G2-216-25-150	34.3	201	16	25	i	0.10	-	-	142	0.22
f	G2-313-25-150	34.3	203	13	25	i	0.10	-	-	148	0.20
g	G1	58.1	262	16	30	iv	-	-	1.30	-	-
g	G1-ST	58.1	252	16	30	iv	-	-	1.30	-	-
g	G1	58.1	262	16	30	iv	0.50	-	-	148	1.11
g	G1	58.1	262	16	30	iv	0.40	-	-	118	1.11
g	G1	58.1	262	16	30	iv	0.35	-	-	115	1.00
g	G1-ST	58.1	252	16	30	iv	0.50	-	-	153	1.04
g	G1-ST	58.1	252	16	30	iv	0.40	-	-	134	0.95
g	G1-ST	58.1	252	16	30	iv	0.35	-	-	126	0.88
h	B1	31	243	15.9	38	i	0.70	-	1.39	190	0.93
h	B2	31	229	19.1	50	i	0.70	-	0.68	370	0.41
h	B3	36	243	15.9	38	i	0.70	-	0.81	290	0.61
h	B4	36	229	19.1	50	i	0.70	-	0.98	240	0.63
h	B5	36	231	15.9	50	i	0.70	-	1.37	185	0.85
h	B6	36	241	19.1	38	i	0.70	-	0.95	210	0.82
h	B7	32	243	15.9	38	i	0.70	-	1.09	225	0.78
h	B8	32	229	19.1	50	i	0.70	-	0.76	-	-
h	B9	32	243	15.9	38	i	0.70	-	0.98	243	0.73
h	B10	32	229	19.1	50	i	0.70	-	1.74	140	1.09
h	B13	28	243	15.9	38	i	0.70	-	1.21	200	0.88
h	B14	28	229	19.1	50	i	0.70	-	1.11	210	0.72
h	B15	28	243	15.9	38	i	0.70	-	0.84	275	0.64
h	B16	28	229	19.1	50	i	0.70	-	0.99	235	0.65
h	S1	31	107	9.5	38	iv	0.70	-	0.93	350	0.59
h	S2	31	106	12.7	38	iv	0.70	-	0.63	365	0.43
h	S3	36	104	15.9	38	iv	0.70	-	0.67	290	0.38
h	S4	36	102	19.1	38	iv	0.70	-	0.33	360	0.21
h	S5	30	157	9.5	38	iv	0.70	-	0.51	290	0.80

Reference [a]	Specimen nomenclature	Properties					1	2	3	4	5
								k_b reported by authors			
		f'_c (MPa) [b]	d (mm) [c]	d_b (mm) [d]	c_c (mm) [e]	Surface treatment [f]	w (mm)	Gergely-Lutz Equation [2.10]	Frosch Equation [2.11]	Calculated or reported f_f in extreme tension layer (MPa)	k_b calculated in present study for w (column 1)
h	S6	30	156	12.7	38	iv	0.70	-	0.44	-	-
h	S7	29	154	15.9	38	iv	0.70	-	0.90	200	0.63
h	S8	29	152	19.1	38	iv	0.70	-	0.73	190	0.46
h	S9	25	162	25.4	50	iv	0.70	-	-	1300	0.07
h	B1	31	243	15.9	38	i	0.40	-	-	153	0.66
h	B2	31	229	19.1	50	i	0.40	-	-	215	0.40
h	B3	36	243	15.9	38	i	0.40	-	-	195	0.52
h	B4	36	229	19.1	50	i	0.40	-	-	155	0.56
h	B5	36	231	15.9	50	i	0.40	-	-	148	0.61
h	B6	36	241	19.1	38	i	0.40	-	-	172	0.57
h	B7	32	243	15.9	38	i	0.40	-	-	163	0.62
h	B8	32	229	19.1	50	i	0.40	-	-	185	0.47
h	B9	32	243	15.9	38	i	0.40	-	-	185	0.54
h	B10	32	229	19.1	50	i	0.40	-	-	100	0.87
h	B13	28	243	15.9	38	i	0.40	-	-	143	0.71
h	B14	28	229	19.1	50	i	0.40	-	-	138	0.63
h	B15	28	243	15.9	38	i	0.40	-	-	188	0.54
h	B16	28	229	19.1	50	i	0.40	-	-	155	0.56
h	S1	31	107	9.5	38	iv	0.40	-	-	210	0.30
h	S2	31	106	12.7	38	iv	0.40	-	-	215	0.29
h	S3	36	104	15.9	38	iv	0.40	-	-	155	0.41
h	S4	36	102	19.1	38	iv	0.40	-	-	240	0.18
h	S5	30	157	9.5	38	iv	0.40	-	-	190	0.36
h	S6	30	156	12.7	38	iv	0.40	-	-	295	0.24
h	S7	29	154	15.9	38	iv	0.40	-	-	138	0.52
h	S8	29	152	19.1	38	iv	0.40	-	-	148	0.34
h	S9	25	162	25.4	50	iv	0.40	-	-	400	0.12
i	N2#13G2	33.5	344	13	40	iv	1.03	**1.04**	**1.14**	-	-
i	N3#13G1	33.5	344	13	40	iv	0.78	**1.10**	**1.41**	-	-
i	H2#13G2	59.1	344	13	40	iv	0.83	**0.93**	**1.02**	-	-
i	H3#13G1	59.1	344	13	40	iv	0.55	**1.58**	**2.09**	-	-
i	N5#15G2	29.0	322	16	40	iv	0.31	**0.83**	**1.13**	-	-
i	N6#15G1	33.5	319	16	40	iv	0.15	**0.35**	**0.46**	-	-
i	H5#15G2	73.4	322	16	40	iv	0.26	**0.55**	**0.75**	-	-
i	H6#15G1	73.4	319	16	40	iv	0.45	**0.87**	**1.16**	-	-
i	N5#15G3	33.8	322	16	40	iii	0.40	**1.40**	**1.91**	-	-
i	N2#25G3	33.8	337	25	40	iii	0.45	**1.28**	**1.55**	-	-
i	H5#15G3	73.4	322	16	40	iii	0.62	**1.43**	**1.95**	-	-
i	H2#25G3	73.4	337	25	40	iii	0.54	**0.85**	**1.03**	-	-
i	N2#13G2	33.5	344	13	40	iv	0.70	-	-	295	0.82
i	N3#13G1	33.5	344	13	40	iv	0.70	-	-	244	0.92
i	H2#13G2	59.1	344	13	40	iv	0.70	-	-	458	0.53
i	H3#13G1	59.1	344	13	40	iv	0.70	-	-	314	0.72
i	N5#15G2	29.0	322	16	40	iv	0.70	-	-	297	0.74

Reference [a]	Specimen nomenclature	Properties					1	2	3	4	5
								k_b reported by authors			
		f'_c (MPa) [b]	d (mm) [c]	d_b (mm) [d]	c_c (mm) [e]	Surface treatment [f]	w (mm)	Gergely-Lutz Equation [2.10]	Frosch Equation [2.11]	Calculated or reported f_f in extreme tension layer (MPa)	k_b calculated in present study for w (column 1)
i	N6#15G1	33.5	319	16	40	iv	0.70	-	-	335	0.46
i	H5#15G2	73.4	322	16	40	iv	0.70	-	-	500	0.45
i	H6#15G1	73.4	319	16	40	iv	0.70	-	-	238	0.65
i	N5#15G3	33.8	322	16	40	iii	0.70	-	-	251	0.76
i	N2#25G3	33.8	337	25	40	iii	0.70	-	-	173	1.20
i	H5#15G3	73.4	322	16	40	iii	0.70	-	-	213	0.90
i	H2#25G3	73.4	337	25	40	iii	0.70	-	-	184	1.14
j	N-212-D2-A	32.1	144	12	32	iii	0.70	-	0.84 -1.10	592	0.47
j	N-212-D2-B	32.1	144	12	32	iii	0.70	-	0.84 -1.10	592	0.47
j	N-216-D2-A	32.1	142	16	32	iii	0.70	-	0.84 -1.10	460	0.59
j	N-216-D2-B	32.1	142	16	32	iii	0.70	-	0.84 -1.10	345	0.78
j	N-316-D2-A	32.1	142	16	32	iii	0.70	-	0.84 -1.10	468	0.56
j	N-316-D2-B	32.1	142	16	32	iii	0.70	-	0.84 -1.10	483	0.55
j	N-212-D1-A	32.1	164	12	12	iii	0.40	-	-	502	0.41
j	N-212-D1-B	32.1	164	12	12	iii	0.40	-	-	571	0.36
j	N-216-D1-A	32.1	162	16	12	iii	0.40	-	-	403	0.52
j	N-216-D1-B	32.1	162	16	12	iii	0.40	-	-	504	0.41
j	N-316-D1-A	32.1	162	16	12	iii	0.40	-	-	396	0.52
j	N-212-D2-A	32.1	144	12	32	iii	0.40	-	-	355	0.45
j	N-212-D2-B	32.1	144	16	32	iii	0.40	-	-	375	0.42
j	N-216-D2-A	32.1	142	16	32	iii	0.40	-	-	218	0.71
j	N-216-D2-B	32.1	142	16	32	iii	0.40	-	-	241	0.64
j	N-316-D2-A	32.1	142	16	32	iii	0.40	-	-	312	0.48
j	N-316-D2-B	32.1	142	16	32	iii	0.40	-	-	234	0.64
k	N2#4	41.5	256	12	28	v	0.70	-	0.98	581	0.27
k	N2#5	41.5	254	16	28	v	0.70	-	0.71	587	0.27
k	N2#6	41.5	240	20	40	v	0.70	-	1.03	524	0.23
k	N2#8	41.5	238	25	40	v	0.70	-	0.88	415	0.28
l	G1-6	39.05	232	12.7	30	iv	0.47	-	1.07	-	-
l	G1-8	39.05	232	12.7	30	iv	0.38	-	1.08	-	-
l	G2-6	39.05	233	12	30	iii	0.51	-	1.04	-	-
l	G2-8	39.05	233	12	30	iii	0.42	-	1.02	-	-
l	G1-6	39.05	232	12.7	30	iv	0.70	-	-	169	0.60
l	G1-8	39.05	232	12.7	30	iv	0.70	-	-	246	0.42
l	G2-6	39.05	233	12	30	iii	0.70	-	-	190	0.49
l	G2-8	39.05	233	12	30	iii	0.70	-	-	221	0.43
l	G1-6	39.05	232	12.7	30	iv	0.50	-	-	130	0.56
l	G1-8	39.05	232	12.7	30	iv	0.50	-	-	147	0.50
l	G2-6	39.05	233	12	30	iii	0.50	-	-	146	0.46
l	G2-8	39.05	233	12	30	iii	0.50	-	-	127	0.54
m	G2N0	43	197	6.4	50	i	0.30	**1.57**	**1.99**	304	0.23
m	G3N0	39	195	9.5	50	i	0.30	**1.97**	**2.49**	-	-
m	G4N0	39	194	12.7	50	i	0.30	**1.04**	**1.30**	161	0.49
m	G2P1	31	197	6.4	50	i	0.30	**0.67**	**0.85**	531	0.13

Reference [a]	Specimen nomenclature	Properties					1	2	3	4	5
								k_b reported by authors			
		f'_c (MPa) [b]	d (mm) [c]	d_b (mm) [d]	c_c (mm) [e]	Surface treatment [f]	w (mm)	Gergely-Lutz Equation [2.10]	Frosch Equation [2.11]	Calculated or reported f_f in extreme tension layer (MPa)	k_b calculated in present study for w (column 1)
m	G3P1	33	195	9.5	50	i	0.30	**0.84**	**1.06**	-	-
m	G4P1	30	194	12.7	50	i	0.30	**0.57**	**0.71**	295	0.26
n	C3 X 8.5H5	27.9	182	15.9	25	i	0.15	**0.4**	**0.48**	283	0.18
n	C4 X 8.5H5	27.9	182	15.9	25	i	0.16	**0.4**	**0.44**	281	0.16
n	C5 X 8.5H5	27.9	182	15.9	25	i	0.17	**0.4**	**0.40**	279	0.14
n	C6 X 8.5H5	27.9	182	15.9	25	i	0.29	**0.4**	**0.37**	278	0.21
n	C3 X 8.5P5	27.9	182	15.9	25	iv	0.22	**0.4**	**0.48**	283	0.26
n	C4 X 8.5P5	27.9	182	15.9	25	iv	0.19	**0.4**	**0.44**	281	0.19
n	C5 X 8.5P5	27.9	182	15.9	25	iv	0.12	**0.4**	**0.40**	279	0.10
n	C6 X 8.5P5	27.9	182	15.9	25	iv	0.12	**0.4**	**0.37**	278	0.09
o	GIS-6	39.05	232	12.7	30	i	0.70	**0.83**	**1.10**	178	0.80
o	GIS-8	39.05	232	12.7	30	i	0.70	**0.83**	**1.10**	250	0.58
o	GCB-6	39.05	233	12	30	iii	0.70	**0.83**	**1.10**	183	0.71
o	GCB-8	39.05	233	12	30	iii	0.70	**0.83**	**1.10**	216	0.62
p	S-G1	40	162	15.9	30	iv	0.70	**0.60**	**0.67**	257	0.51
p	S-G2	40	159	22.2	30	iv	0.70	**0.60**	**0.67**	186	0.67
p	S-G3	40	159	22.2	30	iv	0.70	**0.60**	**0.67**	176	0.92
q	1A, 1B	44	179	15	35	iv	-	**0.76**	**0.84**	-	-
q	2A, 2B	36	179	15	35	iv	-	**0.76**	**0.84**	-	-
q	3A, 3B	42	179	15	35	iv	-	**0.76**	**0.84**	-	-
q	4A, 4B	46	179	15	35	iv	-	**0.76**	**0.84**	-	-
q	1A, 1B	44	179	15	35	iv	0.16	-	-	171	0.22
q	1A, 1B	44	179	15	35	iv	0.27	-	-	213	0.29
q	1A, 1B	44	179	15	35	iv	0.36	-	-	256	0.33
q	2A, 2B	36	179	15	35	iv	0.17	-	-	171	0.23
q	2A, 2B	36	179	15	35	iv	0.27	-	-	214	0.29
q	2A, 2B	36	179	15	35	iv	0.36	-	-	256	0.33
q	3A, 3B	42	179	15	35	iv	0.07	-	-	171	0.10
q	3A, 3B	42	179	15	35	iv	0.17	-	-	213	0.19
q	3A, 3B	42	179	15	35	iv	0.30	-	-	256	0.27
q	4A, 4B	46	179	15	35	iv	0.14	-	-	171	0.19
q	4A, 4B	46	179	15	35	iv	0.23	-	-	213	0.25
q	4A, 4B	46	179	15	35	iv	0.30	-	-	256	0.27
r	BC2NA	53.1	148	12.3	20	v	0.70	**0.58**	**0.60**	420	0.55
r	BC2NB	53.1	148	12.3	20	v	0.70	**0.58**	**0.60**	270	0.85
r	BC2HA	57.2	148	12.3	20	v	0.70	**0.58**	**0.60**	300	0.77
r	BC2HB	57.2	148	12.3	20	v	0.70	**0.58**	**0.60**	270	0.85
r	BC2VA	97.4	148	12.3	20	v	0.70	**0.58**	**0.60**	209	1.11
r	BC4HB	53.9	119	12.3	20	v	0.70	**0.58**	**0.60**	332	0.35
r	BC4VA	93.5	119	12.3	20	v	0.70	**0.58**	**0.60**	377	0.31
r	BC4VB	93.5	119	12.3	20	v	0.70	**0.58**	**0.60**	330	0.35
r	BC2NA	53.1	148	12.3	20	v	0.40	-	-	240	0.55
r	BC2NB	53.1	148	12.3	20	v	0.40	-	-	180	0.73
r	BC2HA	57.2	148	12.3	20	v	0.40	-	-	210	0.63

Reference [a]	Specimen nomenclature	Properties					1	2	3	4	5
								k_b reported by authors			
		f'_c (MPa) [b]	d (mm) [c]	d_b (mm) [d]	c_c (mm) [e]	Surface treatment [f]	w (mm)	Gergely-Lutz Equation [2.10]	Frosch Equation [2.11]	Calculated or reported f_f in extreme tension layer (MPa)	k_b calculated in present study for w (column 1)
r	BC2HB	57.2	148	12.3	20	v	0.40	-	-	210	0.63
r	BC2VA	97.4	148	12.3	20	v	0.40	-	-	119	1.11
r	BC4NA	46.2	119	12.3	20	v	0.40	-	-	262	0.25
r	BC4HA	53.9	119	12.3	20	v	0.40	-	-	285	0.23
r	BC4HB	53.9	119	12.3	20	v	0.40	-	-	225	0.29
r	BC4VA	93.5	119	12.3	20	v	0.40	-	-	259	0.26
r	BC4VB	93.5	119	12.3	20	v	0.40	-	-	200	0.33
s	CB2B-2	52	253	14.9	30	v	0.70	**1.00**	**1.14**	177	0.94
s	CB3B-1	52	253	14.9	30	v	0.70	**1.00**	**1.14**	224	0.75
s	CB3B-2	52	253	14.9	30	v	0.70	**1.00**	**1.14**	159	1.36
s	CB4B-1	45	230	14.9	30	v	0.70	**1.00**	**1.14**	167	1.30
s	CB4B-2	45	230	14.9	30	v	0.70	**1.00**	**1.14**	225	0.62
s	CB6B-1	45	230	14.9	30	v	0.70	**1.00**	**1.14**	254	0.55
s	CB6B-2	45	230	14.9	30	v	0.70	**1.00**	**1.14**	147	0.94
s	CB2B-2	52	253	14.9	30	v	0.70	**1.00**	**1.14**	167	0.83
s	CB2B-1	52	253	14.9	30	v	0.40	-	-	118	0.81
s	CB2B-2	52	253	14.9	30	v	0.40	-	-	124	0.77
s	CB3B-1	52	253	14.9	30	v	0.40	-	-	83	1.48
s	CB3B-2	52	253	14.9	30	v	0.40	-	-	119	1.04
s	CB4B-1	45	230	14.9	30	v	0.40	-	-	136	0.59
s	CB4B-2	45	230	14.9	30	v	0.40	-	-	142	0.56
s	CB6B-1	45	230	14.9	30	v	0.40	-	-	118	0.67
s	CB6B-2	45	230	14.9	30	v	0.40	-	-	101	0.78

[a] Reference list given in Section 3.1.
[b] f'_c = concrete compressive strength.
[c] d = depth of the section.
[d] d_b = bar diameter.
[e] c_c = clear cover.
[f] Surface treatment: i = helically wrapped with sand-coated; ii = helically wrapped; iii = grooved/ indented; iv = sand-coated; v = ribbed.

3.2 Discussion of the qualitative analysis

Gergely and Lutz (1968) proposed a crack prediction equation – widely used for steel reinforced concrete members – that was deducted from a regression analysis of a relatively limited number of reinforced concrete beam test results. This equation is reported to yield unconservative results compared to available experimental data for steel-RC members (Bischoff et al., 2009). The modifications to the Gergely-Lutz equation (Equation 2.10) for the calculation of crack width for GFRP-RC members were developed from theory and, therefore, replicate the unconservative nature of the equation; this is seen on the results in Table 3.1 for crack width of 0.70 mm. Frosch (1999) developed a physical model to estimate crack width, applying to both steel and FRP reinforcement, although ACI PRC 440.1 (2006) establishes a correction coefficient k_b – extensively discussed in Section 2.2 – to account for differences in FRP bond behaviour compared to steel. In this light, the present study is focused on the assessment of k_b estimated using the Frosch equation (Equation 2.11).

As described in Chapter 2, the influence of bond between GFRP bars and the surrounding concrete on cracking predictions is an aspect that requires further study for GFRP-RC members. The database assembled for this study demonstrates how much some factors can apparently affect k_b estimation calculated using the Frosch equation and thereby provides some guidance for future experimental study.

3.2.1 k_b versus crack width

Figure 3.3 (a) and (b) plots crack widths corresponding to reported and back-calculated k_b values, respectively, obtained from the database analysis.

The reported values of k_b vary from 0.45 to 1.40 and calculated values vary from 0.07 to 1.48. In both cases, most values fell below 1.0, indicating GFRP bond behaviour superior to that of steel reinforcement. As crack widths at which k_b is estimated increase, the range of k_b increases and more data tends to fall above 1.0 (Figure 3.3a). Bond is a highly localised phenomenon (e.g., Figure 2.8), whereas the predictions described make the assumption of an average bond stress between adjacent cracks. Thus, the calculation of k_b is a function of service load level and by extension crack width. To assess the k_b factor rationally, one must assign a crack width

dimension to consider – in this study, and many others, the behaviour at w = 0.70 mm, as described.

Figure 3.3 – Reported (a) and calculated (b) k_b (Equation 2.11) *versus* crack width.

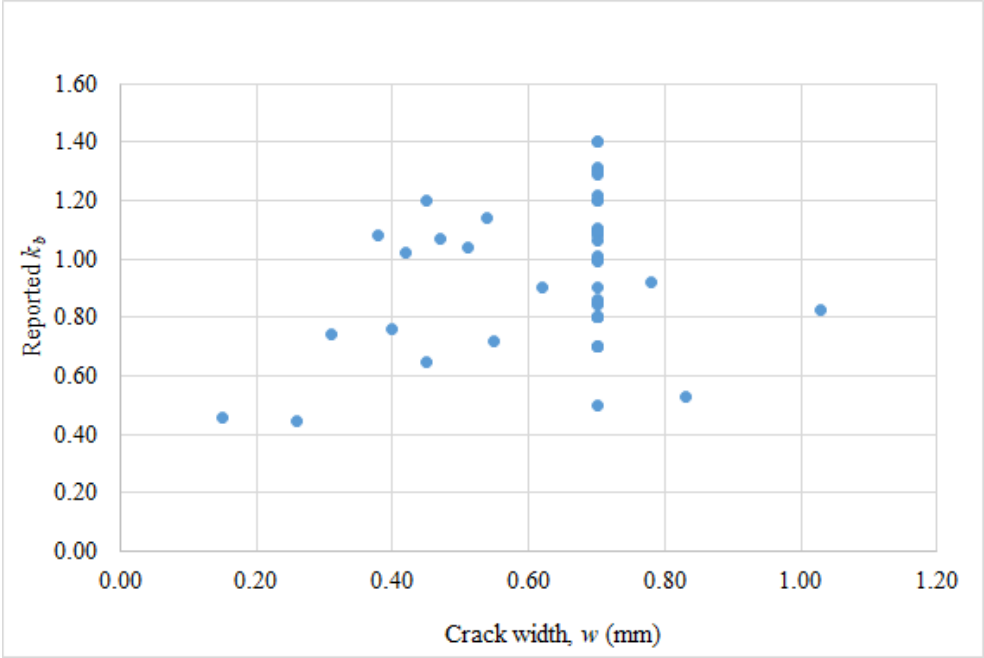

(a)

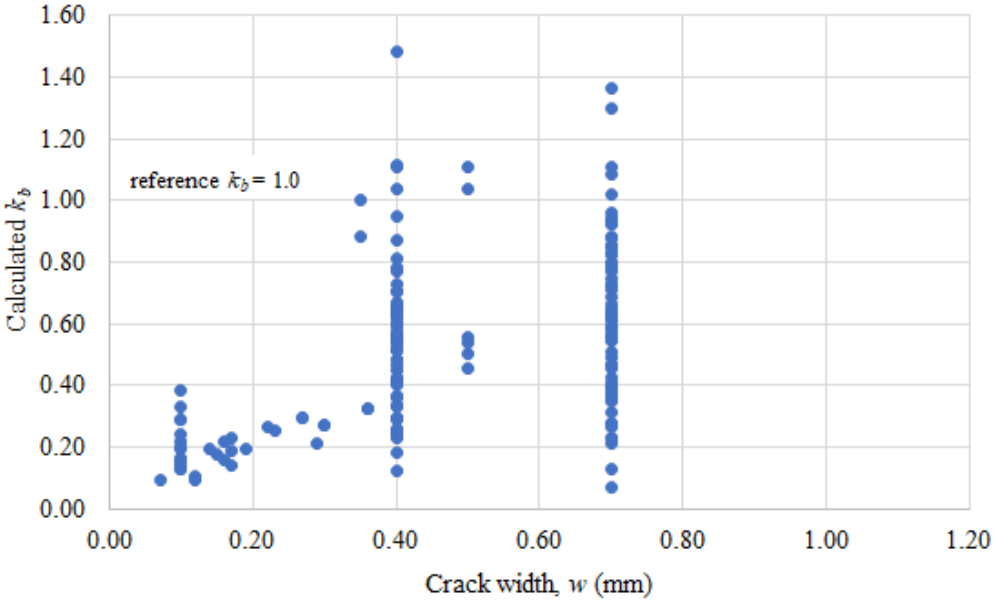

(b)

Source: author.

The following analyses were made using data for crack width equal to 0.70 mm in order to eliminate the influence of different values of crack width on the assessment.

The different colors used in the graphs of the following items means data from different studies.

3.2.2 k_b versus bar diameter

Figures 3.4 and 3.5 show bar diameter *versus* k_b values and bar diameter *versus* GFRP reinforcing bar stress, f_f, respectively. It is observed that there is no clear trend between the diameter of the GFRP bars and the predicted k_b. This conclusion was also reported by Tran et al. (2018) and is limited to the bar diameters considered: those between 12.7 and 25 mm. Once again, it is pointed out that the data in this analysis is dominated by bars having $k_b < 1$.

The very general trend shown in Figure 3.5 that larger bars have a lower stress at a crack width of w = 0.70 mm reflects the nature of GFRP bars, whose tensile strength falls as the diameter increases (see Section 2.1.2). Thus, at a specified service condition (w = 0.70 mm), one expects the bar stress to be inversely proportional to the diameter, indicating a constant proportional service stress level (some proportion of f_f).

Figure 3.4 – Reported and calculated k_b (Equation 2.11) *versus* bar diameter (for w = 0.70 mm).

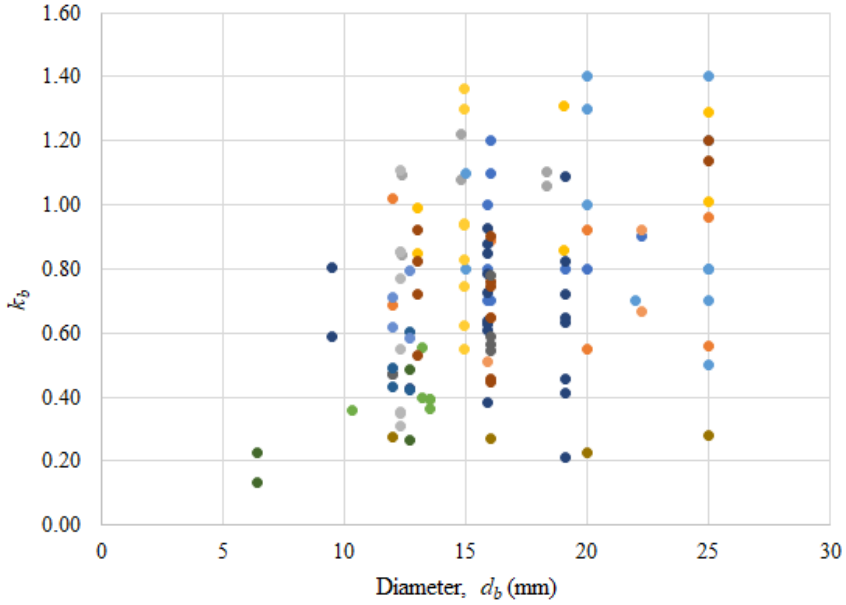

Source: author.

Figure 3.5 – GFRP reinforcing bar stress, f_f, *versus* diameter (for w = 0.70 mm).

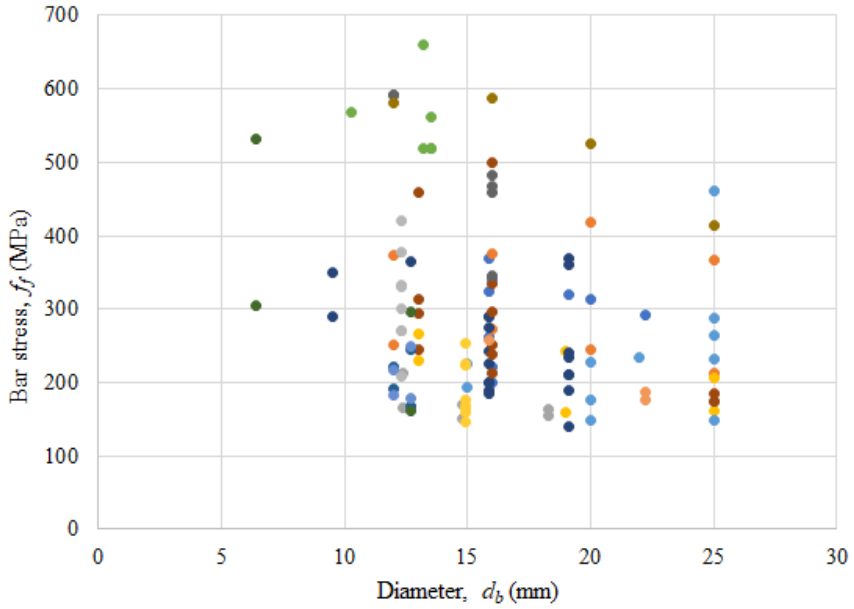

Source: author.

Figure 3.6 plots f_f *versus* bond coefficient k_b for the beams tested by Abdelkarim et al. (2019) as a representative example to demonstrate that the relationship between k_b and bar stress is inversely proportional and essentially linear in the range of expected service stress levels of 200 to 500 MPa, which corresponds in this study to $0.17f_{fu}$ to $0.42f_{fu}$ (where f_{fu} is the tensile strength of the GFRP bar). This conclusion was also reported by Shield et al. (2019).

Figure 3.6 – Representative example of calculated k_b (Equation 2.11) *versus* bar stress, f_f, (for w = 0.70 mm) for beams tested by Abdelkarim et al. (2019).

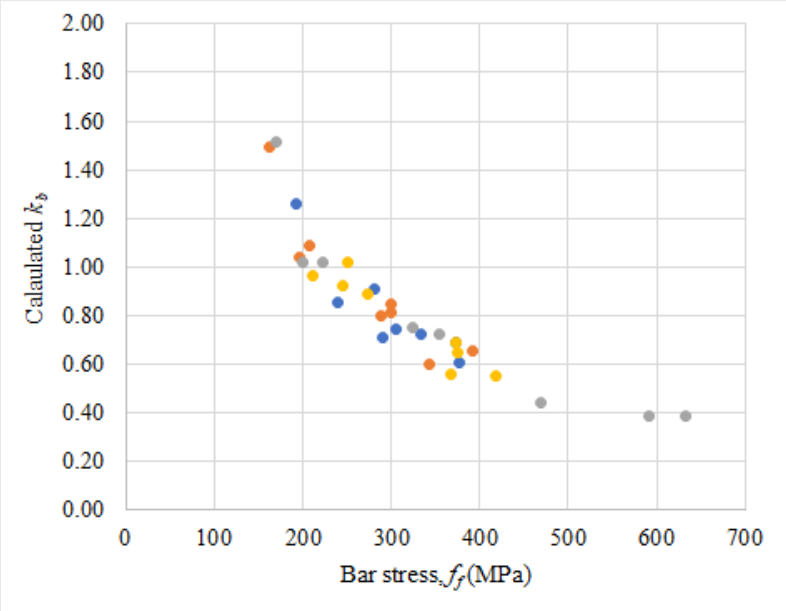

Source: author.

3.2.3 k_b versus clear cover and concrete compressive strength

Based on the available experimental data for crack width of 0.70 mm, no clear effect on the estimation of k_b is observed varying clear cover and concrete compressive strength as shown in Figure 3.7 and 3.8, respectively.

Figure 3.7 – Reported and calculated k_b (Equation 2.11) *versus* clear cover (for w = 0.70 mm).

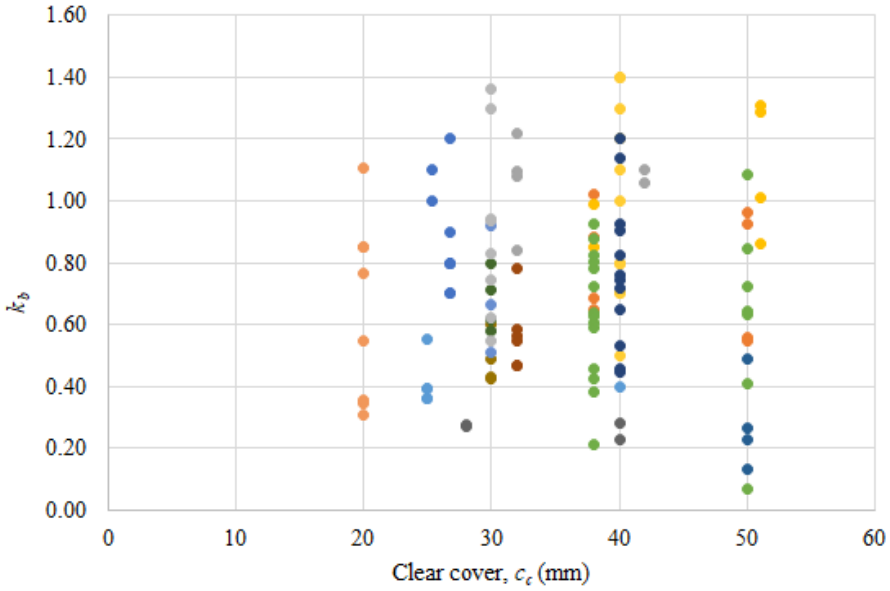

Source: author.

Figure 3.8 – Reported and calculated k_b (Equation 2.11) *versus* concrete compressive strength (for w = 0.70 mm).

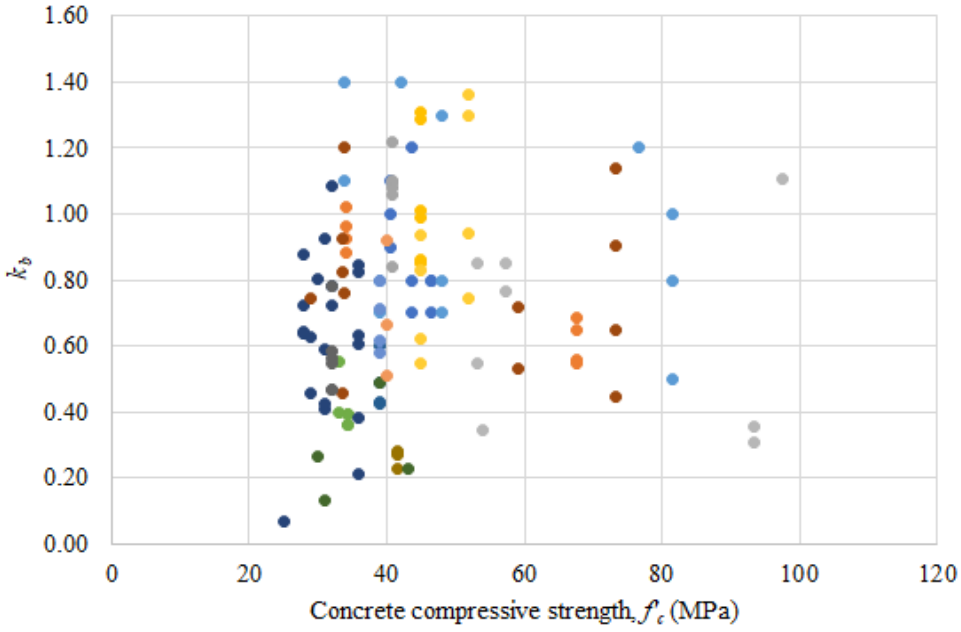

Source: author.

3.2.4 k_b versus surface treatment

Contrary to the assertions of some previous research, based on the database, there is no clear effect of surface treatment on k_b (Figure 3.9). El-Nemr et al. (2016) and Shang (2019) both reported that sand-coated GFRP bars presented lower values of k_b compared to deformed bars, indicating better bond behaviour of sand-coated bars. This trend is not apparent from the compiled database; although it is seen that most results fall below k_b = 1.0.

Figure 3.9 – Reported and calculated k_b (Equation 2.11) *versus* surface treatment (for w = 0.70 mm).

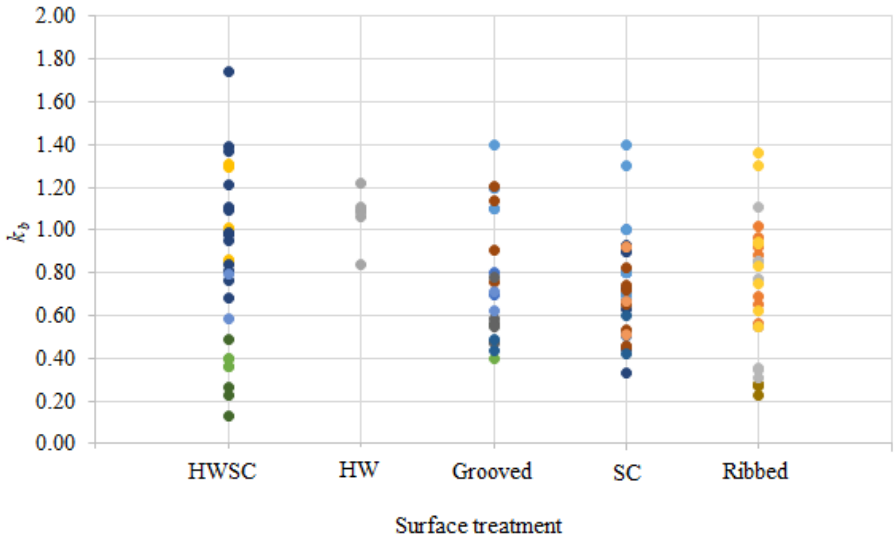

HWSC - Helically wrapped with sand-coated; HW - Helically wrapped; SC - Sand-coated.

Source: author.

Table 3.2 presents the measures of central tendency (minimum, maximum, average and median) of values of k_b for each type of surface configuration represented in the database. Analysing k_b in this manner, it is concluded that there is little difference in bond behaviour of grooved (average k_b = 0.79), sand-coated (average k_b = 0.74), and ribbed GFRP (average k_b = 0.70) bars across the entire dataset. It must be understood, however, that there is no way in this data to assess the quality of the bar fabrication itself. The presented data is a snapshot of bars available over the last two decades and the variability highlights the difficulty of assigning a single value to k_b.

Table 3.2 – Minimum and maximum k_b values for each type of surface treatment.

Bar type		Helically wrapped with sand-coated	Helically wrapped	Grooved	Sand-coated	Ribbed
Reference		Barris et al. (2016)	Sólyom and Balázs (2020)	Barris et al. (2016)	El-Nemr et al. (2013)	Abdelkarim et al. (2019)
Image of the bar (all images are not at the same scale)						
k_b (Frosch equation)	Minimum	0.13	0.84	0.40	0.33	0.23
	Maximum	1.74	1.22	1.40	1.40	1.36
	Average	0.84	1.07	0.79	0.74	0.70
	Median	0.86	1.09	0.71	0.72	0.72

In order to correlate the surface types of the bars assessed in this investigation, a two-tailed "*t-test*" was performed to assess whether the different surface configurations of GFRP bars behaved (statistically speaking) in the same manner. The "*p-values*" are reported in Table 3.3. The results marked in bold text indicate that the behaviour of the surface type of the referenced GFRP bars is similar, even across data from different studies. This analysis confirms that there is no significant statistical difference between the estimated k_b values attributed to the surface configurations of grooved, sand-coated, and ribbed GFRP bars (*p-value* > 0.05) (see Table 3.3). The only statistically different surface treatment is helically wrapped bars (without sand coating) which exhibit a statistically significant higher value of k_b (Table 3.2).

Table 3.3 – Correlation matrix of surface configuration of GFRP bars.

Surface type / P-value	Helically wrapped with sand-coated	Helically wrapped	Grooved	Sand-coated	Ribbed
Helically wrapped with sand-coated	1.0000				
Helically wrapped	**0.1658**	1.0000			
Grooved	**0.6125**	0.0353	1.0000		
Sand-coated	**0.2052**	0.0015	**0.4763**	1.0000	
Ribbed	**0.1376**	0.0076	**0.3004**	**0.5588**	1.0000

3.2.5 k_b versus service stress

Figure 3.10 shows that reported k_b varies with the service stress level in GFRP reinforcement at which k_b is estimated; similar data is reported by McCallum (2013). Service stress values for FRP-reinforced concrete members reported in the literature and design documents range from 15 to 30% of the tensile strength of FRP bar (f_{fu}), with the value of $0.30f_{fu}$ reported by many studies (e.g., Mota et al., 2006; Bischoff et al., 2009; Kassem et al., 2011; El-Nemr et al., 2016). This value is lower than the limit adopted for steel-reinforced concrete members: ACI 318 (2019) recommends a service stress equal to 0.67 of the specified yield stress of steel (f_y). The lower service level stress for GFRP bars reflects their lower modulus, brittle behaviour and susceptibility to creep effects (ACI PRC 440.1-15). Figure 3.10 indicates that for lower service levels, the estimated value of k_b tends to be lower; while for greater service limits, k_b tends to assume higher values. This observation is similar to that made in regard to Figure 3.3 since crack width and service load level are correlated. It is noted that there is no significant difference in k_b estimation for service limits of $0.25f_{fu}$ and $0.30f_{fu}$.

Figure 3.10 – Reported k_b (Equation 2.11) *versus* service stress level (for w = 0.70 mm).

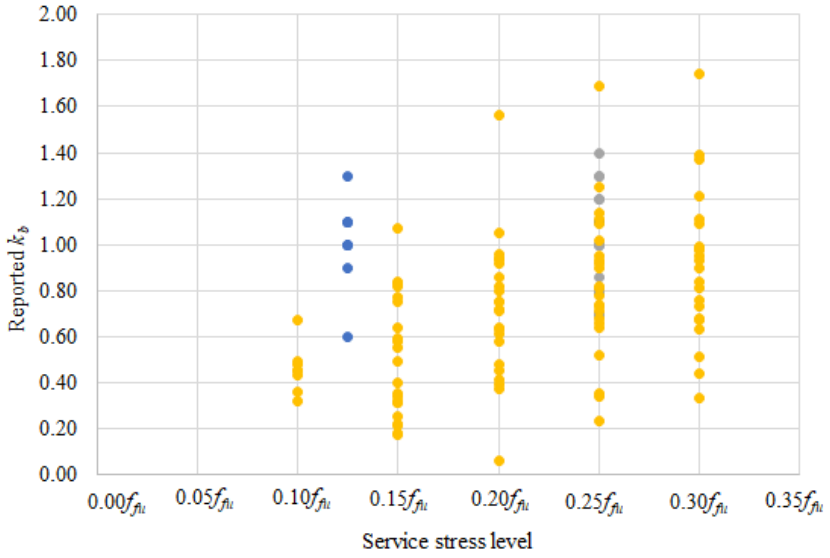

Source: author.

Figure 3.11 shows calculated and reported k_b coefficients over the past two decades determined for a crack width equal to 0.70 mm. No temporal trend is evident and, again, most data indicate

bond performance equal or better than steel reinforcing bars ($k_b \leq 1$). Thus, there is little incentive on the part of the manufacturers to improve bond performance.

Figure 3.11 – Calculated and reported k_b (Equation 2.11) *versus* year (for w = 0.70 mm).

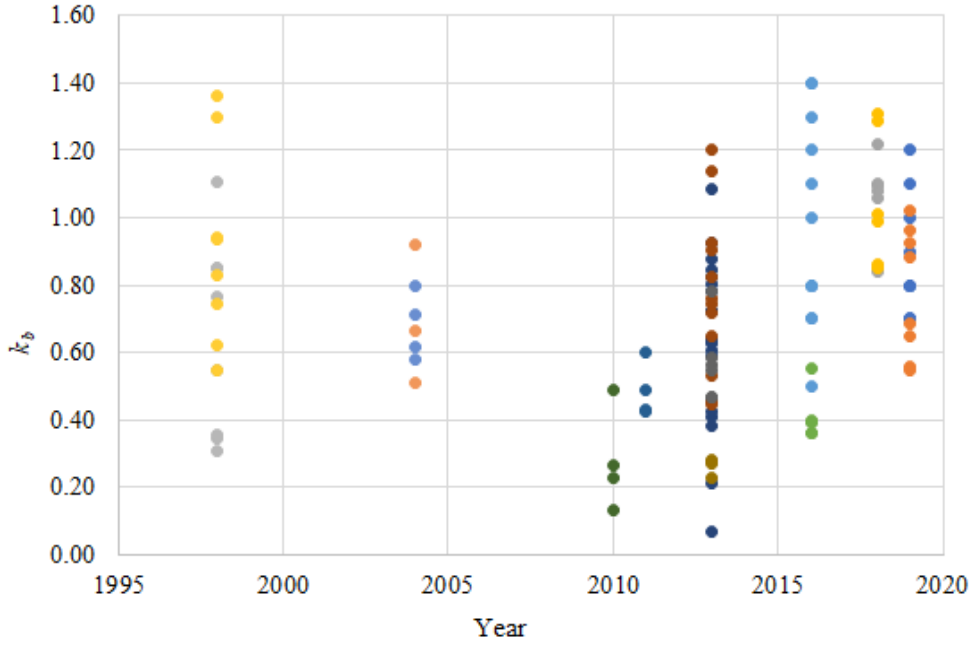

Source: author.

3.2.6 Gergely-Lutz equation versus Frosch equation

Although the analysis discussed on Section 3.2 was focused on the assessment of k_b estimated by the Frosch equation (Equation 2.11), a statistical analysis was used to verify whether or not there is significant difference between k_b estimated by Gergely-Lutz and Frosch equations (Equations 2.10 and 2.11, respectively). The analysis was based on k_b coefficients calculated using both equations for the same specimen whose values were reported by the authors (see the values marked in bold text on Table 3.1) and was carried out using RStudio software, version 2023.06.2-561 considering 5% level of significance.

The paired "*t-test*" showed that the mean value of k_b calculated by Gergely-Lutz equation was statistically different from the mean k_b calculated by Frosch equation ($t(79) = -0.78$; *p-value* < 0.0001). The mean k_b = 0.81 for Gergely-Lutz equation was less than the mean k_b = 0.98 estimated by Frosch equation.

The data analyzed refers to GFRP bars having helically wrapped with sand-coated, grooved and sand-coated surface types. Tukey's test, at a 5% significance level, showed that there is no statistical difference on k_b estimation by Gergely-Lutz equation for helically wrapped with sand-coated and grooved GFRP bars (Table 3.4). Additionally, Tukey's test confirmed that there is no statistical difference for any bars tested using Frosch equation (see Table 3.4; for results across the entire dataset, see Table 3.1).

As the paired "*t-test*" is a parametric test assuming the difference between two dependent variables has Normal distribution, a Shapiro-Wilk (S-W) normality test was used to confirm this hypothesis. The null hypothesis states that the data distribution is normally distributed, i.e., *p-value* is greater than 0.05; otherwise, the null hypothesis is rejected. Using the S-W test, *p-value* was found to be 0.0002, indicating that the variable representing the difference between k_b estimated by Gergely-Lutz and Frosch equations does not assume a Normal Distribution. Then, the Wilcoxon signed-rank test was used to confirm the conclusions made using the paired "*t-test*". The Wilcoxon test showed the k_b coefficients calculated by the Gergely-Lutz equation to be less than those calculated by the Frosch equation (the median of the differences is equal to -0.14), confirming that this difference is statistically significant ($V = 34$; *p-value* < 0.0001).

Table 3.4 – Mean k_b values.

Surface type / Mean k_b	Gergely-Lutz [Equation 2.10]	Frosch [Equation 2.11]
Helically wrapped with sand-coated	0.95	1.11
Grooved	0.88	1.05
Sand-coated	0.68	0.86

Sections 3.3 and 3.4 were developed collaboratively with Dr. Chase Rogers and co-advisor Dr. Kent Harries as reported in: Silva, E.M., Harries, K.A., Rogers, C., Ludvig, P. and Cabral de Azevedo, R. (in preparation) Meta-Study of Bond-Dependent Coefficient for GFRP Reinforcing Bars.

3.3 Meta-analysis

One-way ANOVA analysis was conducted on all variables presented in Table 3.1 with the intent of discerning the significance of experimental variables on the calculated values of k_b. Analysis was conducted using a bespoke Python (v3.8.13) code implementing NumPy (v1.22.3) statistical analysis tools. The variables considered, their definition, distribution of values represented in the data set (mean, COV, minimum and maximum values), and number of available data points for each (not all data is available for each test) are shown in Table 3.5. Only k_b values calculated using the Frosch equation are considered since these are consistently calculated across the database. Three calculations are reported in Table 3.5:

- $k_{b,F}$ is the value of k_b, reported to be calculated using Frosch equation (Equation 2.11), reported by the source study authors;
- $k_{b,0.7}$ is the value of k_b calculated in the present study for w = 0.70 mm as described in analysis step (iii) (Section 3.1.1); and,
- $k_{b,w}$ is is the value of k_b calculated in the present study for $w \neq 0.70$ mm as described in analysis step (iv) (Section 3.1.1).

As discussed later, the determination of k_b is sensitive to the crack width, w, at which it is calculated. For this reason, a normalised parameter, k_b/w is included in the analysis. Since bar surface treatment is a non-numeric variable, ANOVA considered all bar types together. Further, analyses addressing bar surface treatment is presented in Section 3.4.3.

Table 3.5 - Variables considered in one-way ANOVA analyses.

Variable	Description	Mean	COV	Min.	Max.	Count
c_c	concrete cover (mm)	34.2	0.26	12	55	234
f'_c	concrete strength (MPa)	42.6	0.34	25	97	234
d_b	bar diameter (mm)	15.7	0.24	6.4	25.4	234
f_f	calculated bar stress (MPa)	260	0.52	83	1300	216
$k_{b,F}$	k_b reported by original source based on Equation [2.11]	0.98	0.37	0.33	2.49	132
$k_{b,0.7}$	k_b calculated in present study for w = 0.70 mm	0.66	0.40	0.23	1.36	63
$k_{b,w}$	k_b calculated in present study for $w \neq 0.70$ mm	0.45	0.63	0.09	1.48	99
k_b/w	k_b normalised by crack width; $k_{b,0.7}/0.7$ or $k_{b,w}/w$	1.23	0.48	0.30	3.70	216

As seen in Figure 3.12, data, while monotonic, is nonlinear. Therefore, the Spearman correlation coefficient, r_s, is used to assess the statistical dependence of one variable with another. The resulting Spearman coefficients for all variables are shown in Table 3.6; incomplete sample pairs are neglected. By convention, $|r_s| > 0.7$ is a "strong" correlation; these are noted in bold font in Table 3.6. Values of $|r_s| < 0.2$ indicate "very weak" or negligible correlation; these are noted in italic font.

Table 3.6 – Spearman correlation coefficients, r_s.

	c_c	f'_c	d_b	f_f	$k_{b,F}$	$k_{b,0.7}$	$k_{b,w}$	k_b/w
c_c	1	*-0.12*	0.40	*-0.07*	0.32	*0.05*	*0.10*	*-0.04*
f'_c		1	*-0.06*	*-0.14*	*0.08*	*0.06*	0.36	*0.16*
d_b			1	*-0.10*	*-0.05*	*0.18*	0.22	*0.19*
f_f				1	-0.38	**-0.70**	-0.56	**-0.72**
$k_{b,F}$					1	0.30	no matching pairs	0.35
$k_{b,0.7}$						1		**1**
$k_{b,w}$							1	0.54
k_b/w								1

$\|r_s\| \geq 0.8$	**very strong**
$0.8 > \|r_s\| \geq 0.6$	**strong**
$0.6 > \|r_s\| \geq 0.4$	moderate
$0.4 > \|r_s\| \geq 0.2$	weak
$\|r_s\| < 0.2$	*very weak*

The most significant correlations evident are with calculated bar stress, f_f, indicating the sensitivity of the method of determination of k_b. By normalising k_b/w, as described below, all variables, except bar stress, are shown to be very weak correlations, leaving only bar stress, f_f, as a strong correlation. For this reason, bar stress, f_f, will be the primary focus of subsequent discussion.

3.4 Discussion of the quantitative analysis

3.4.1 Source-reported bond coefficients: $k_{b,F}$

Correlation between calculated $k_{b,0.7}$ and source-reported $k_{b,F}$ are weak (r_s = 0.30) indicating potential inconsistency in the manner in which $k_{b,F}$ is calculated and/or reported across the literature. This finding reinforces the need for desk studies such as that presented here to consolidate and curate data in a consistent manner. In the present study, k_b is calculated as shown in Appendix B based on reported experimentally-determined material properties and specimen geometries, and direct calculation of the reinforcing bar stress – something rarely reported in the literature. This direct calculation results in lower values of k_b than are generally reported (Table 3.5).

3.4.2 Normalising by crack width: k_b/w

There is no universally agreed "serviceability crack width" at which k_b should be determined. A preponderance of available data uses w = 0.70 mm (Table 3.1), although this is not possible for some reported studies. Figure 3.12a illustrates the relationship between bar stress, f_f, and k_b. The nonlinear monotonic relationship is seen, as is a marked difference between $k_{b,0.7}$ determined at w = 0.70 mm and $k_{b,w}$ determined at another crack width, in all cases less than 0.70 mm. The sensitivity of the calculation of k_b as a function of the crack width at which is determined is evident. As the crack width increases, the calculated value of k_b increases. Figure 3.12b shows the same data with k_b normalised by the crack width at which it was calculated: k_b/w. Equations for the trendlines shown in Figure 3.12 are given in Table 3.7. The normalisation – the author contend – allows k_b data to be combined regardless of the crack width at which it is determined. Data for hairline cracks (13 data points having w = 0.10 mm all reported by Barris et al., 2016), will naturally be more sensitive to the precision of the crack width measurement and will only include lower bar stresses. Excluding values of k_b/w determined from such hairline cracks, results in Equation [3.1] having a marginal improvement in correlation coefficient, R^2 = 0.59, over data that includes hairline cracks ("all data" in Table 3.7).

$$k_b/w = 61.4 f_f^{-0.74} \tag{3.1}$$

Shield et al. (2019) reported the 70th percentile for describing reinforcing bar bond coefficients; this value is that on which ACI CODE-440-11 (2022) provisions are based (see ACI CODE-440-11 §R24.3.2.3). For the present data, the 70th percentile value of k_b/w (excluding $w \leq 0.10$ mm) is described by Equation [3.2] and is shown in Figure 3.12c:

$$k_b/w = 76 f_f^{-0.74} \tag{3.2}$$

Table 3.7 – Equations of trend lines shown in Figure 3.12.

	Data pairs	Figure 3.12a		Figure 3.12b		Figure 3.12c	
		Equation	R^2	Equation	R^2	Equation	R^2
w = 0.70 mm	63	$k_b = 34.5 f_f^{-0.71}$	0.52	$k_b/w = 49.3 f_f^{-0.71}$	0.52	$k_b/w = 49.3 f_f^{-0.71}$	0.52
w = 0.40 mm	54	$k_b = 18.4 f_f^{-0.68}$	0.53	$k_b/w = 46.1 f_f^{-0.68}$	0.53	$k_b/w = 46.1 f_f^{-0.68}$	0.53
w = 0.10 mm	13	$k_b = 65.1 f_f^{-1.12}$	0.60	$k_b/w = 651 f_f^{-1.12}$	0.60	not shown	-
All data	162	$k_b = 5.90 f_f^{-0.467}$	0.17	$k_b/w = 78.8 f_f^{-0.783}$	0.57	not shown	
All data $w \geq 0.10$ mm	149	not shown	-	not shown	-	$k_b/w = 61.4 f_f^{-0.74}$	0.59
70th percentile	-	-	-	-	-	$k_b/w = 76 f_f^{-0.74}$	-

ACI CODE-440.11 (2022) §R24.3.2.2 limits FRP bar stress at the serviceability limit state based on a presumption of w = 0.70 mm:

$$f_f \leq 0.36 E_f / d_c \beta k_b \tag{3.3}$$

where, E_f is the elastic modulus of the bar, which is permitted (§20.2.2.2) to be taken as the minimum value specified by ASTM D7957, 44.8 GPa; d_c is thickness of concrete cover (in mm) measured from the extreme tension fiber to the center of nearest longitudinal tension reinforcing bar; and, β is the ratio of the distance from the neutral axis of the member to the extreme tension fiber to the distance from the neutral axis to the centroid of the tensile reinforcement (given by Equation [B.6] in Appendix B). ACI CODE-440.11 (2022) prescribes k_b = 1.2 (§24.3.2.3). Based on Equation [3.3], the typical range of f_f for design falls between about 180 to 250 MPa and marginally higher for slabs (having smaller d_c, typically). This range is shown in Figure 3.12c.

Using Equation [3.2] and a serviceability crack width of w = 0.70 mm, a characteristic bond coefficient suitable for design is determined as falling between k_b = 1.14 and 0.90 for typical service stresses of f_f = 180 to 250 MPa, respectively. These values are slightly below the ACI-prescribed value of k_b = 1.2.

Thus, the present treatment of the available data confirms the appropriate, and marginally conservative nature of the selection of k_b = 1.2 for design. The range of observed data reinforces the potential for individual bar manufacturers to develop test values that would allow a lower value of k_b to be adopted; however, no protocol or standard yet exists for this determination.

Figure 3.12 – Bar stress, f_f, versus bond performance parameters.

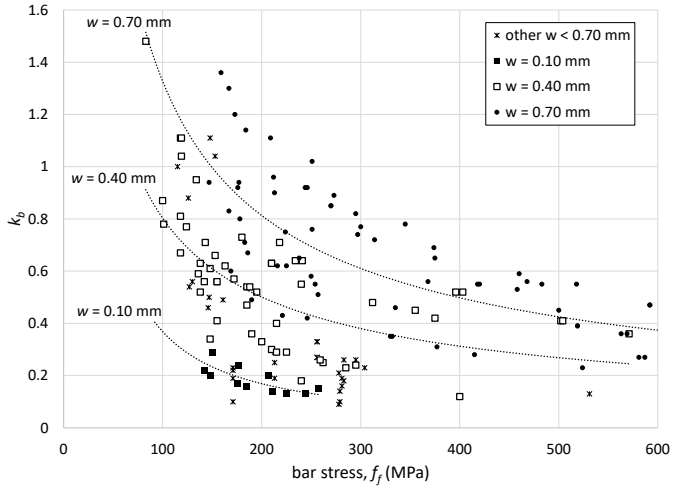

a) Bar stress, f_f, versus bond coefficient, k_b.

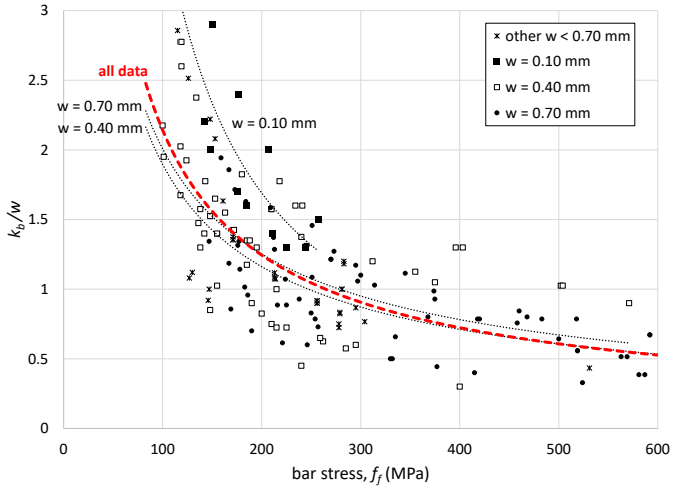

b) Bar stress, f_f, versus normalised bond coefficient, k_b/w.

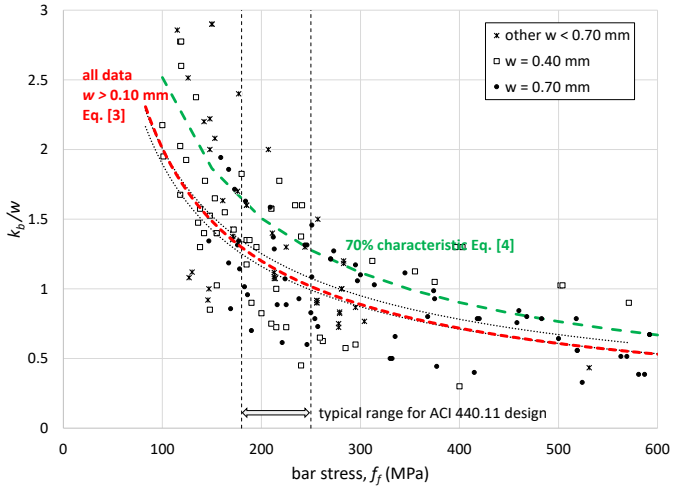

c) Bar stress, f_f, versus normalised bond coefficient, k_b/w, excluding data from $w \leq 0.10$ mm.
Source: Silva et al. (in preparation).

3.4.3 Effects of bar surface treatment

The dataset reported five FRP bar surface treatments as summarised in Table 3.8:

(i) helically wrapped bundles of longitudinal glass fibre having an external coating comprising sand embedded in the (typically vinyl ester) resin.

(ii) helically wrapped bundles of longitudinal glass fibre having no external coating beyond the resin [only six data points for this bar type from a single source are available – while this data is included in the previous discussion, there is insufficient data to include this bar type in the present discussion].

(iii) pultruded GFRP bars that have had grooves or deformations machined into them following resin cure.

(iv) otherwise, smooth GFRP bars that have an external coating comprising sand embedded in the resin.

(v) pultruded "ribbed" GFRP bars that are fabricated with deformations (rather than the deformation being machined afterward as in [iii]). Ribbed bars typically most closely resemble steel reinforcing bars.

Table 3.8 summarises k_b/w data separated by bar surface treatment. Figure 3.13 repeats the data shown in Figure 3.12c also separated by surface treatment; the equations for the best fit curves shown in Figure 3.13 are reported in Table 3.8. Bar types (i), (iii), (iv) and (v) are well-represented in the dataset reflecting the variation and distribution in the GFRP bar market.

A two-tailed t-test shows that the separating the data by surface preparation does not result in statistically significant difference in calculated k_b values between bar types or when compared to all bar types combined (as is presented previously). The large scatter (as measured by the coefficient of variation, COV, shown in Table 3.8) leads to the larger *p*-values.

As seen in both Table 3.8 and Figure 3.13, bar type (iii), having machined grooves, is not only the best performing bar type (k_b/w = 1.07), but also presents the least variation (COV = 0.32). Nonetheless, with the typical range of bar service stress, there is little difference in bar bond performance evident based on surface treatment.

Table 3.8 – Summary of bond parameters for w > 0.10 mm shown in Figure 3.13.

Designation in Table 3.1		i	ii	iii	iv	v	All
Bar type		Helically wrapped with sand coating	Helically wrapped only	Machined grooved	Sand-coated (otherwise undeformed)	Ribbed	Combined
Sources [1]		d, f, h, m, n, o	c	a, e, f, i, j, l, o	a, e, g, h, i, l, n, p, q	b, k, r, s	
Example image of bar type (source of image)		(f)	(Sólyom and Balázs 2020)	(f)	(i)	(b)	
Number in full dataset		58	6	46	86	46	242
	n	28	0	29	46	46	149
k_b/w	Average	1.15	-	1.07	1.15	1.25	1.18
	COV	0.39	-	0.32	0.50	0.55	0.47
Equation of trend line		$k_b/w = 118 f_f^{-0.87}$	-	$k_b/w = 6.0 f_f^{-0.31}$	$k_b/w = 142 f_f^{-0.92}$	$k_b/w = 300 f_f^{-1.04}$	$k_b/w = 61.4 f_f^{-0.74}$
R^2 of trend line		0.93	-	0.20	0.27	0.76	0.59
Correlation matrix (p-value from two-tailed t-test)	i	1	-	0.45	0.97	0.50	0.78
	iii	-	-	1	0.49	0.20	0.30
	iv	-	-	-	1	0.48	0.76
	v	-	-	-	-	1	0.49

[a] Reference list given in Section 3.1.

Figure 3.13 – Bar stress, f_f, versus normalised bond coefficient, k_b/w, for different bar surface treatments for w > 0.10 mm.

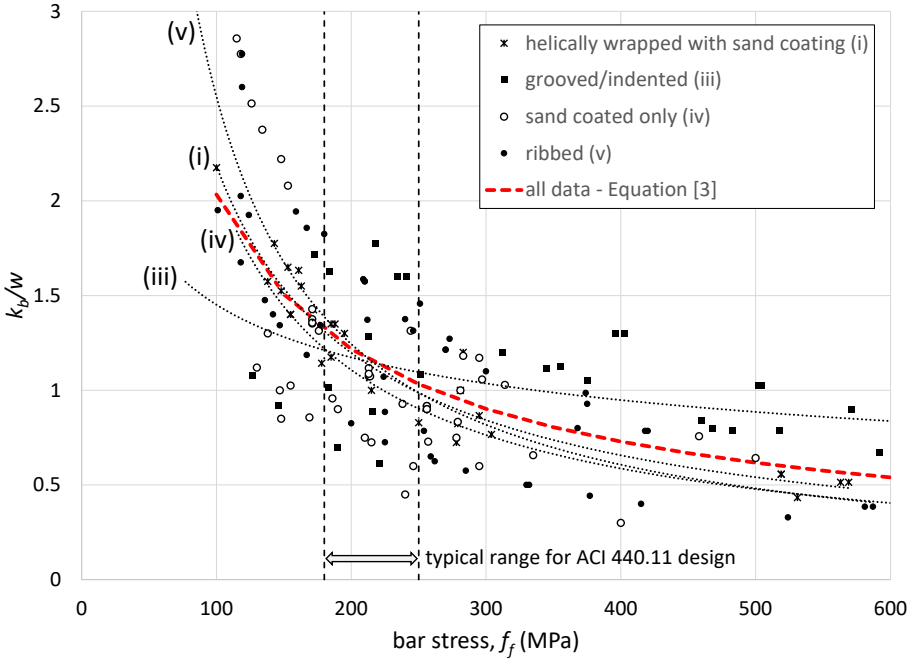

Source: Silva et al. (in preparation).

3.5 Summary of the chapter

This chapter reported a qualitative and quantitative study of the bond-dependent coefficient, k_b, based on data available in published literature in which k_b was predicted from experimental flexural tests using GFRP bars. Results from 19 studies were compiled and analyzed in order to demonstrate the influence of some parameters in the estimation of k_b. Crack with, w, equal to 0.70 mm was used to represent the Serviceability Limit State described by ACI PRC 440.1-15. Data for which k_b could not be calculated at w = 0.70 mm was used to estimate values of k_b at different stress levels and helped to illustrate how the determination of k_b is affected by the bar stress at which it is calculated.

In this study, k_b is calculated based on reported experimentally-determined material properties and specimen geometries, and direct calculation of the reinforcing bar stress – something rarely reported in the literature. Interestingly, direct calculation in this manner did not correlate well with literature-reported values of k_b. This finding reinforces the need for desk studies such as that presented here to consolidate and curate data in a consistent manner.

Both qualitative and quantitative analysis showed that:

— a key observation of this study is that k_b is sensitive to the concrete crack width at which it is calculated. This led to the adoption of a normalized value k_b/w which allows a broader range of available data to be included. Based on sensitivity to measurement precision, the authors propose that data for which k_b is calculated at crack widths $w \leq$ 0.10 mm be excluded;

— the value of k_b was found to be strongly correlated with the GFRP reinforcing bar stress, f_f, at which k_b is determined. Correlations with other factors including concrete strength, cover concrete (greater than 12 mm) and GFRP bar diameter (less than 25 mm) were weak, reinforcing that the k_b factor is a bond coefficient dependent on the reinforcing bar, not its embedment;

— the calculation of the bond coefficient, k_b, is relatively insensitive to the surface treatment of the bar: whether deformed (ribbed) or sand-coated. This finding may

partially reflect that all bars reported were commercially available and have therefore, presumably, undergone quality improvement and optimization during their development. That is, if the design standards adopt k_b = 1.2, commercially available bars will tend to coalesce around this value;

— equation [3.1] is proposed to represent the mean relationship between k_b/w and GFRP reinforcing bar stress, f_f, corresponding to w. Equation [3.2] captures the 70th percentile – that used by ACI 440.11-22 – of this data;

— based on current ACI 440.11-22 serviceability stress limits, the range of 70th percentile k_b values for design range between 0.90 and 1.14, marginally below the presently recommended default value of k_b = 1.2. The authors feel that maintaining the recommended value for design in the absence of bar-specific testing as k_b = 1.2 is appropriately conservative and reflects the still relatively small amount of available data. It is noted that as of this writing, there is no universally agreed test method or protocol for reporting k_b and that the expected scatter in such measurement would require a robust experimental program.

4

MATERIALS CHARACTERISATION

In this chapter, the properties of concrete and GFRP bars used in the experimental portions of this study are described. Steel reinforcing bars used for experimental control specimens are also reported.

4.1 Concrete

Three different concrete mixes having specified 28-day compressive strength of 35 MPa were used as shown in Table 4.1. Batches C1 and C2 correspond to tests conducted in Brazil, while C3 corresponds to tests conducted in the USA. Table 4.2 identifies which concrete was used with which bars. The mix compositions (per cubic meter) for each concrete type are detailed in Table 4.1.

Table 4.1 – Composition of concrete mixes and strengths (COV in parentheses).

Concrete batch	C1	C2	C3
Laboratory	CEFET-MG	CEFET-MG	PITT
Cement type	CP-V	CP-V	CP I/II
Coarse aggregate type	9.5 mm gravel	9.5 mm gravel	9.5 mm limestone
Cement content (kg/m³)	420	420	385
Water content (kg/m³)	277	277	150
Fine aggregate (sand) content (kg/m³)	827	797	733
Coarse aggregate content (kg/m³)	814	845	1077
Water/ cement (w/c) ratio	0.66	0.66	0.39
Additives (% w/cement)	-	-	Sika AE260: 0.06% Sika 10N: 0.1% SikaPlast 200: 0.2%
28-day compressive strength, f'_c, (MPa) ASTM C39	33.2 (0.03)	35.0 (0.01)	37.8 (0.06)
28-day tensile strength (MPa) ASTM C496	f_{sp} = 3.1 (0.16)	f_{sp} = 2.9 (0.39)	f_{ct} = 2.2 (0.24)

Concretes C1 and C2 were mixed in situ, using Brazilian cement type CPV-ARI, with a maximum coarse aggregate size of 9.5 mm and a water/ cement (w/c) ratio equal to 0.66. In an attempt to produce concrete batches with as little variability as possible, a rigorous quality

control was applied on the production of such concretes. A total of 10 concrete cube specimens for pull-out tests were fabricated using concrete C1 and 10 specimens using C2 concrete. The concrete compressive strength for each batch was determined at 28 days (f'_c) by testing three 100 x 200 mm cylinders in accordance with ASTM C39 (2021). Following the ASTM C496 (2017) guidelines, concrete splitting tensile strength (f_{sp}) was determined from split-cylinder testing on three 100 x 200 mm cylinders at 28 days.

Concrete C3 was obtained from a ready-mix plant located in Pittsburgh, PA; all the specimens tested in the USA were fabricated with the same batch of C3 concrete. The mixture was made of cement type CEM I/II with 9.5 mm maximum aggregate size and using a *w*/*c* of 0.39. 28-day compression tests (ASTM C39) were performed. The tensile strength (f_{ct}) of batch C3 was calculated based on the appearance of the first crack in the prisms tension tests and was found to be f_{ct} = 2.2 MPa (COV = 0.24). The detailed calculation of f_{ct} is presented in Appendix C. The direct tensile strength, f_{ct}, is not directly comparable with that determined from a split cylinder test, f_{sp}. The direct tensile strength will be lower: approximately $f_{ct} \approx 0.67 f_{sp}$ (Collins and Mitchell, 1997). Thus, the tensile strengths of C1, C2, and C3 batches are comparable (Table 4.1).

4.2 Reinforcing bars

Material properties, bar geometry and surface characteristics of the seven commercially available GFRP and four steel bars used in this study are presented in Table 4.2. The nomenclature #X indicates X eights of an inch nominal diameter (US designation).

Nominal (i.e., geometry used for design), and measured bar geometries are provided (see Section 4.2.3 for the detailed characterisation). Tension properties of the bars were determined experimentally (ASTM D7205-21) or obtained from mill certificates – these are mean properties, not "guaranteed" (i.e., characteristic) properties used for design.

Table 4.2 – Characteristics of bars used in this study.

Bar	#2 hGFRP	#3 hGFRP	#4 rGFRP	#6 rGFRP	#4 sGFRP	#5 sGFRP	#5 sGFRP-s	#2 steel	#3 steel	#4 steel	#6 steel
Deformation type	Helically wrapped		Machined ribs		Sand-coated		Most sand removed	Deformed steel reinforcement			
Image of the bar (Images are not same scale)										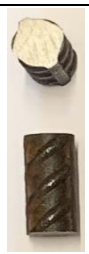	
Bar size	#2	#3	#4	#6	#4	#5	#5	#2	#3	#4	#6
Nominal bar diameter d_b (mm)	6.3	9.5	12.7	19.1	12.7	15.9	15.9	6.3	9.5	12.7	19.0
Nominal area of bar A_b (mm²)	31	71	127	284	127	199	199	31	71	127	284
Measured d_b (mm)	-	-	13.8	20.4	13.2	17.5	16.9	-	-	12.5	19.0
Measured A_b (mm²)	-	-	146	321	122	219	215	-	-	119	269
Modulus of elasticity of bar E_b (GPa)	28	37	60.3[m]	60.3[m]	46.9[m]	48.4[p]	48.4[p]	200	200	200	200
Tensile strength of bar f_{fu} (MPa)	590	973	962[m]	898[m]	927[m]	739[p]	739[p]	500[m]	500[m]	500[m]	500[m]
Yield strength of steel f_y (MPa)	n.a	n.a	n.a	n.a	n.a	n.a	n.a	400[m]	400[m]	400[m]	400[m]
Relative Rib Area R_r (Eq. 2.1)	0.035	0.050	0.030	0.024	n.a	n.a	n.a	0.049	0.086	0.074	0.089
Concrete batch	C2	C2	C3	C3	C3	C3	C3	C1	C1	C3	C3

[m] Values obtained from mill certificates; values are experimentally determined otherwise.
[p] Experimentally-determined values originally reported in Platt (2018).

4.2.1 #5 sGFRP-s bars

The bond behaviour of the bar-concrete interface is influenced, among other factors, by the surface treatment of GFRP bars. Bars with smooth surface present poor bond performance and are not recommended for structural applications (Cosenza et al., 1997; Yan et al., 2016; *fib*, 2013). Furthermore, ACI PRC 440.1 (2015) excludes smooth bars from the recommendation for bond coefficient k_b = 1.4 when k_b is not known from experimental data and highlights that further analysis is needed to determine a k_b value for such reinforcement.

In order to investigate the variation of k_b, a small number of samples of the #5 sand-coated bar (#5 sGFRP) were manually abraded (using a silicon carbide sanding belt) to remove much of the sand coating; these are designated as #5-sGFRP-s in this study. These bars have a very small amplitude deformation formed by the helical wrapping of the glass fiber bundle; this can be seen in the image in Table 4.2.

4.2.2 Mechanical characterisation

To determine the tensile strength of #2 hGFRP and #3 hGFRP bars, five specimens for each bar were tested in direct tension. All the GFRP bars tested had a total length of 1,000 mm and an anchoring length equal to 200 mm (Figure 4.1a). Since the anisotropic behaviour of GFRP bars is different from that of steel, the conventional method of gripping tends to crush GFRP bar ends and can cause premature tension failure. To prevent this, each end of the bar was anchored in steel tubes filled with “Viapoxi Adesivo Gel” epoxy resin (Figure 4.1b). The outer and inner diameters of the steel tube used for anchorage were 25.5 and 20.9 mm, respectively.

To avoid any flexural load during the test, the GFRP bars were axially aligned into the steel tube using a plastic cap on both ends of the tube (Figure 4.1c). The long clear span between anchors also helps to mitigate significant flexure-induced stress in the specimen. The anchoring was cast vertically and left to cure for at least 24 hours prior to casting the second anchorage for the bar. The bars were loaded in tension using an EMIC model DL 30 000 universal test machine with a capacity of 300 kN; load was applied at a displacement rate of 5 mm/min until failure (Figure 4.1d).

Figure 4.1 – Details of the mechanical characterisation of #2 hGFRP and #3 hGFRP bars.

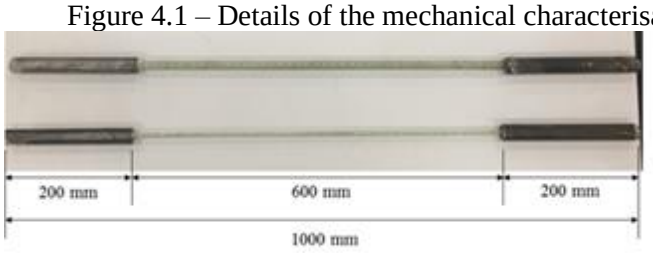

a) Tensile test specimens.

b) Bars anchored with steel tube.

c) Caps used to ensure GFRP bar alignment on the steel tube.

d) Tensile test set-up.

Source: author.

The applied load was measured through a load cell connected to a computer-monitored data-acquisition system and the displacements were captured using an axial extensometer with a gauge length of 50 mm. The extensometer was removed prior to bar rupture to avoid any damage to the equipment. Failure mode in the specimen gage length (i.e., unaffected by the anchorage) of #2 hGFRP and #3 hGFRP bars is shown in Figure 4.2. Average values of the mechanical properties obtained from uniaxial tension tests are reported in Table 4.2. Nominal diameters were used to calculate the mechanical properties of the GFRP bars in accordance with ASTM D7957-22 (2022). Other bars were not tested as part of this study and the provided values from the manufacturer or previously obtained strengths and modulus (from the same batch of bars) are reported in Table 4.2. Since the focus of this study is bond, the bars will not be loaded to their ultimate capacity; therefore, strength is not as important to determine as modulus.

Figure 4.2 – Failure mode of (a) #2 hGFRP and (b) #3 hGFRP bars.

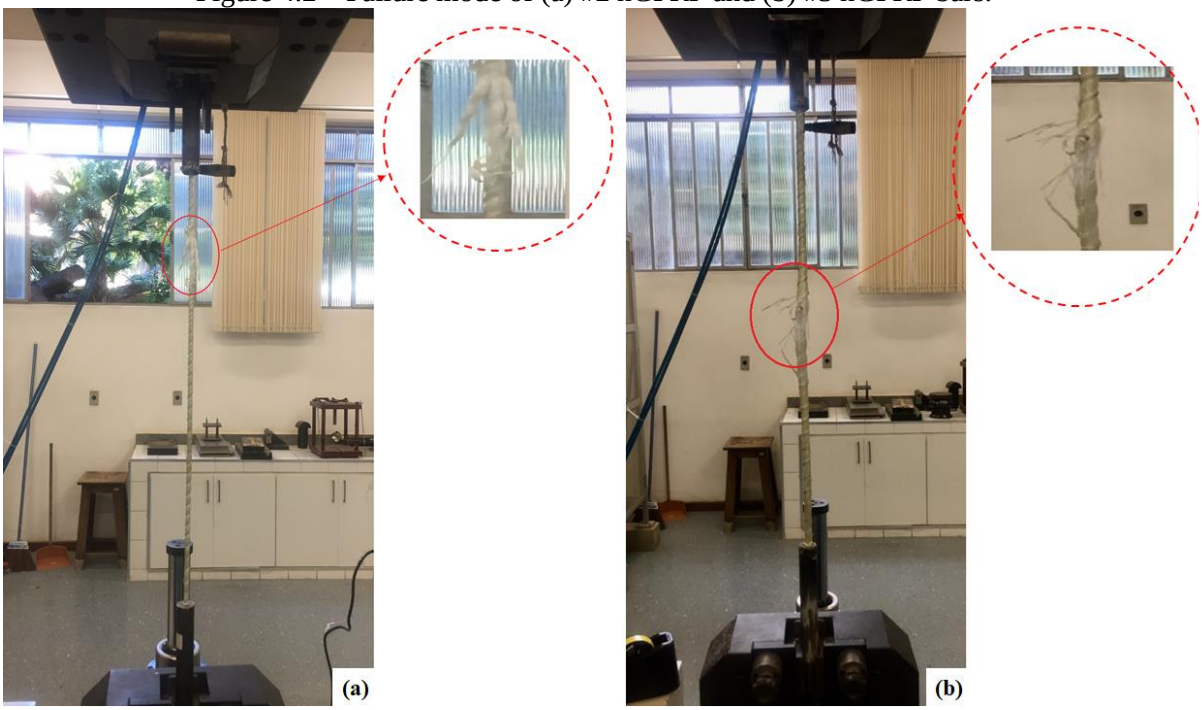

Source: author.

4.2.3 Geometric characterisation

4.2.3.1 Area of bar

The measured area of GFRP bars were obtained using the immersion method (Archimedes principle). Three specimens from each #4 rGFRP, #6 rGFRP, #4 sGFRP, #5 sGFRP, and #5 sGFRP-s bars were cut and tested. Steel bars (#4 steel and #6 steel) were used for comparison purposes. Specimens were suspended by a fine line into a beaker of water placed on a precision electronic scale. The specimens were first weighed before being immersed to determine their dry weight. Then they were immersed in water at 21^{o} C and the change in weight of water recorded after a few seconds of stabilization of the specimen. The volume of each specimen is calculated by dividing the change in weight of the water by the density of water at 21^{o} C. Finally, the measured area is calculated by dividing the volume by the measured length of the specimen. The density of the specimen is determined by its mass divided by the calculated volume. Measured diameter was estimated using caliper in four different points around each specimen. Resulting geometric properties of the tested bars are given in Table 4.3 and summarized in Table 4.2. The geometries of the #2 hGFRP and #3 hGFRP bars were not obtained in this

manner. Test results showed that all GFRP bars met the requirements for the measured area limits specified in ASTM D7957-22 (2022).

Table 4.3 – Geometric properties of bars.

Bar nomenclature	Specimen	Nominal diameter d_b (mm)	Measured d_b (mm)	Measured length (mm)	Measured A_b (mm²)	Density (g/ cm³)
#4 rGFRP	1	12.7	13.83	25.34	145.8	2.132
	2		13.84	25.94	146.2	2.132
	3		13.85	25.53	145.8	2.131
		Average	13.84	25.60	146.0	2.132
		COV	0.0007	0.012	0.002	0.0003
#6 rGFRP	1	19.1	20.32	25.84	321.0	2.157
	2		20.35	26.78	321.0	2.154
	3		20.39	26.05	320.8	2.154
		Average	20.35	26.22	320.9	2.155
		COV	0.002	0.019	0.0003	0.0008
#4 sGFRP	1	12.7	13.19	25.94	121.6	2.159
	2		13.21	25.65	122.0	2.154
	3		13.30	24.77	121.0	2.158
		Average	13.23	25.45	121.6	2.157
		COV	0.004	0.024	0.004	0.001
#5 sGFRP	1	15.9	17.33	25.43	219.1	1.934
	2		17.37	25.79	218.2	1.931
	3		17.70	25.94	219.6	1.93
		Average	17.47	25.72	219.0	1.93
		COV	0.012	0.010	0.003	0.001
#5 sGFRP-s	1	15.9	16.95	25.08	215.1	1.946
	2		16.74	24.50	214.8	1.948
	3		16.92	26.75	214.2	1.949
		Average	16.87	25.44	214.7	1.948
		COV	0.007	0.046	0.002	0.0008
#4 steel	1	12.7	12.50	25.05	120.0	7.843
	2		12.76	25.00	116.2	8.093
	3		12.19	25.02	120.5	7.738
		Average	12.48	25.02	118.9	7.891
		COV	0.023	0.001	0.020	0.023
#6 steel	1	19.1	19.05	25.20	270.4	7.824
	2		18.65	25.34	266.4	7.818
	3		19.25	25.24	271.3	7.796
		Average	18.98	25.26	269.5	7.813
		COV	0.016	0.003	0.009	0.002

4.2.3.2 Deformation measurements

As described in Section 2.1.3, the "relative rib area", R_r, is a geometrical parameter quantifying mechanical bond between steel reinforcing bars and concrete which permits some degree of direct comparison between bars having different deformation patterns. Deformation geometry of the ribbed GFRP and steel bars used in this study was assessed and the results compared against some requirements of ASTM A615-22 (2022). The rib ratio is determined from Equation [2.1]. The deformation measurements are shown in Figure 2.3 and the results for the bars are reported in Table 4.4 and summarized in Table 4.2.

By analysing the summary of the results in Table 4.5, it can be seen that the #2 hGFRP, #3 hGFRP, and #4 rGFRP bars did not meet the requirement of lug spacing. Among GFRP bars, only #2 hGFRP and #3 hGFRP bars satisfy the requirement for lug height, while all the steel bars meet this requirement – the latter is expected since these are ASTM A615 Grade 60 bars. The "relative rib area" is not mentioned in ASTM A615, although a minimum value of 0.05 is inferred for R_r indicating adequate bond performance. #2 hGFRP, #4 rGFRP, and #6 rGFRP bars did not comply with the $R_r \geq 0.05$ condition, although #4 rGFRP and #6 rGFRP bars presented the highest bond stresses among all the GFRP bars tested by pull-out tests (see Section 5.2.3). #5-GFRP deformed sand-coated bars are not included in Tables 4.4 and 4.5 as they have no deformation to measure. An alternate means of quantifying "deformations" for sand-coated bars is needed.

Table 4.4 – Deformation measurements (lug) of bars (undeformed sand-coated bars not included).

Bar nomenclature	Specimen	Nominal diameter d_b (mm)	Lug spacing (s_r) (mm)	Lug height (δ) (mm)	ΣB_n (deg.)	Relative rib area (R_r) Equation [2.1]
	1		15.2	0.50		0.032
#2 hGFRP	2	6.3	15.2	0.70		0.040
	3		15.2	0.40	0	0.032
			Average	0.53		0.035
			COV	0.29		0.130
	1		13.3	0.80		0.060
#3 hGFRP	2	9.5	13.3	0.60		0.045
	3		13.3	0.60	0	0.045
			Average	0.67		0.050
			COV	0.17		0.170
	1		10.2	0.29		0.029
#4 rGFRP	2	12.7	10.2	0.33		0.033
	3		10.2	0.27	0	0.027
			Average	0.30		0.030
			COV	0.10		0.100
	1		10.4	0.25		0.024
#6 rGFRP	2	19.1	10.4	0.24		0.023
	3		10.4	0.25	0	0.024
			Average	0.25		0.024
			COV	0.02		0.020
	1		4.4	0.30	81	0.053
#2 steel	2	6.3	4.4	0.30	76	0.054
	3		4.4	0.20	50	0.039
			Average	0.27	69	0.049
			COV	0.22	0.24	0.170
	1		6.2	0.60	53	0.082
#3 steel	2	9.5	6.2	0.70	61	0.094
	3		6.2	0.60	62	0.080
			Average	0.63	59	0.086
			COV	0.09	0.08	0.090
	1		8.6	0.82	69	0.077
#4 steel	2	12.7	8.6	0.76	73	0.071
	3		8.6	0.78	69	0.074
			Average	0.79	70	0.074
			COV	0.04	0.04	0.040
	1		11.8	1.30	78	0.086
#6 steel	2	19.1	11.8	1.35	71	0.092
	3		11.8	1.31	67	0.090
			Average	1.32	72	0.089
			COV	0.02	0.08	0.030

Table 4.5 – Summary of deformation measurements requirements.

Bar nomenclature	Requirement prescribed in ASTM A615				
	Section 7.3: $s_r < 0.7d_b$	Section 7.4: $\sum$chord < 25% perimeter, i.e., $\sum B_n < 90^o$	Section 7.5: average height of deformation less than limit prescribed in ASTM A615		$R_r \geq 0.05$
#2 hGFRP	X	✓	$\delta \geq 0.25$ mm[(a)]	✓	X
#3 hGFRP	X	✓	$\delta \geq 0.38$ mm	✓	✓
#4 rGFRP	X	✓	$\delta \geq 0.51$ mm	X	X
#6 rGFRP	✓	✓	$\delta \geq 0.97$ mm	X	X
#2 steel	✓	✓	$\delta \geq 0.25$ mm	✓	✓
#3 steel	✓	✓	$\delta \geq 0.38$ mm	✓	✓
#4 steel	✓	✓	$\delta \geq 0.51$ mm	✓	✓
#6 steel	✓	✓	$\delta \geq 0.97$ mm	✓	✓

[(a)] #2 bars are not included in ASTM A615 specification; based on limits for #3 and #4 bars, the implied limit for a #2 bar is $\delta \geq 0.25$ mm.

4.3 Summary of the chapter

Details of the concrete and reinforcing bars used in this work were described in this chapter. Three different concrete mixes with a specified 28-day compressive strength of 35 MPa were used, namely: C1, C2, and C3; the batches C1 and C2 corresponds to the mixes used to fabricate the specimens tested in the first series of tests (pull-out tests performed at CEFET-MG, Brazil) and the C3 batch was used to fabricate the specimens tested in the second series (pull-out and beam prism tests performed at University of Pittsburgh, USA). The concrete compressive and tensile strengths were determined for each mix. Although different concrete batches were utilized, the compressive and tensile capacities are quite similar.

The mechanical and geometrical properties of the GFRP and steel bars used in the tests were also reported in this chapter. Several published studies imply that bars having a "relative rib area" $R_r \geq 0.05$ present satisfactory bond behaviour. The ribbed #4 rGFRP and #6 rGFRP bars did not satisfy this requirement, although they ultimately presented better bond performance in the pull-out tests (detailed in Chapter 5) among all the GFRP bars tested.

5

PULL-OUT TEST

This chapter presents the details and results of the pull-out tests carried out in this work. From the experimental data, an examination of the bond behaviour of the reinforcing bars and the prediction of the bond-dependent coefficient, k_b, were performed. The preparation of specimens, test set-up, and testing procedure are detailed in this chapter. The data obtained in this experimental programme supplemented an extant database of 137 comparable pull-out test results reported by Sólyom and Balázs (2020) covering a greater range of GFRP bar and concrete parameters. Finally, the most relevant aspects of this section are summarized in the end of the chapter.

5.1 Introduction

Pull-out tests are widely used in the assessment of bond behaviour of steel bars embedded in concrete due to their simplicity and ease of application. Nonetheless, it must be noted that pull-out tests are A-B tests: permitting comparison between test parameters but not providing a value of bond relevant for design (see Section 2.1.4.2). The bar is bonded over only a length of five bar diameters ($5d_b$) and the concrete cube or cylinder is sized sufficiently large to avoid splitting failures. In this manner, the average bond performance of the bar over a length of $5d_b$ is assessed. The bond capacity obtained from this test is an extreme upper bound value which cannot be sustained over longer embedment lengths (see Section 2.1.4.4) (Feldman and Bartlett 2005; Osofero et al. 2014). Although continuous load-slip data is recorded, ASTM D7913 defines “control” values of bond strength at slips of 0.05, 0.10, and 0.25 mm. Details of the pull-out test method can be found in Section 2.1.4.2.

5.2 Test details

Two series of pull-out tests were conducted: the first was performed at CEFET-MG (Brazil) using #2 and #3 bars; the second series of tests was conducted at the University of Pittsburgh (USA) with larger #4, #5 and #6 bars. The following sections describe both test series. These tests are essentially compliant with ASTM D7913, although any differences in their conduct are noted.

5.2.1 Test specimens

All the concrete cubes are 200 mm on a side and formed in wood moulds (Figure 5.1a and b). The bars were placed horizontally in the center of the moulds and the debonded region was ensured by encasing the debonded portions of the bars with hose (#2 and #3 bars) or steel electrical conduit (#4, #5 and #6 bars) (Figure 5.1c and d, respectively). Concrete was placed in two lifts with each vibrated using a mechanical wand vibrator; special attention was taken to not disturb the bar (Figure 5.2). After casting, the specimens were covered with burlap and plastic and cured in ambient laboratory conditions. Details of the concrete used to cast the specimens are described in Table 4.1.

The 200 mm cube dimension was selected as this had been demonstrated previously (Platt 2018) to be sufficiently large to mitigate splitting failures for bars up to #6. ASTM D7913 requires that tests that exhibit splitting be excluded from bond evaluation. If splitting is regularly observed, increasing the concrete dimension is recommended.

Figure 5.1 – Details of ASTM D7913 test specimens: 200 mm cube moulds prior to concrete casting.

a) #2 and #3 bars tested at CEFET-MG.

b) #4, #5 and #6 bars tested at PITT.

c) Hose used as bond breaker.

d) Steel conduit used as bond breaker.

Source: author.

Figure 5.2 – ASTM D7913 test specimens after concrete casting at (a) CEFET-MG and (b) PITT.

Source: author.

5.2.2 Test set-up and procedure

All the pull-out tests were performed following the provisions of ASTM D7913. The concrete cubes with embedded reinforcing bars were placed in a steel frame that was positioned in the testing machine, so the bars were placed in tension to “pull-out” the reinforcement from the concrete (Figure 2.7 and Figure 5.3a and b). Servo hydraulic universal testing machines were used at CEFET-MG and PITT with load capacities of 300 and 600 kN, respectively. The slips of the bar at the unloaded (free) end were measured using a plate with a displacement transducer (CEFET-MG; Figure 5.3c) and a custom-fabricated collar with the linear position transducer (PITT; Figure 5.3d). Output data from the testing apparatus and the transducers were recording using an automatic data acquisition system.

Figure 5.3 – ASTM D7913 test set-up.

a) Testing machine used at CEFET-MG.

b) Testing machine used at PITT.

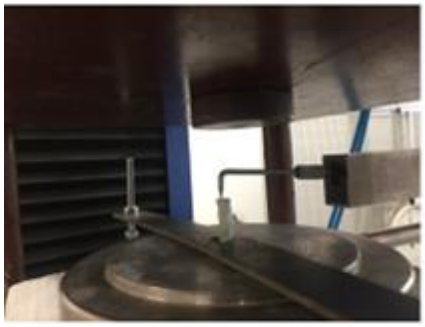

c) Plate with transducer.

d) Collar with transducer.

Source: author.

5.2.3 Pull-out test results

In total, 80 specimens were tested. All experimentally determined bond stress versus slip curves are shown in Figure 5.4. Bond stress, calculated using Equation [2.5], is reported at specific values of slip of 0.05, 0.10, and 0.25 mm (ASTM D7913-14, 2020). The maximum bond stress obtained and the slip corresponding to this stress are also reported. The test programme considered seven GFRP bar types and comparable steel bars (Table 4.2). Recognising the limitations of the ASTM D7913 test as an A-B comparison test, an approximation of the bond-coefficient, k_b, can be calculated as:

$$k_b = \frac{\tau_{steel}}{\tau_{GFRP}} \tag{5.1}$$

where τ_{steel} is the bond stress determined for the control steel bar and τ_{GFRP} is the bond stress of the GFRP bar considered.

The experimental pull-out test results for all 80 specimens tested are given in Appendix D. The results are summarized in Table 5.1. In addition to bond stress and slip values, energy absorption at slip values of 0.25 mm and 1 mm – defined as the area under the bond-slip curve up to these slip values – is also given in Table 5.1. The area under bond-slip curve represents the ability of the bond-slip system to absorb energy in the plastic phase, which is a measure of toughness. The value of slip of 1 mm was a convenient value which captures the behaviour of all specimens tested. Typically, five (CEFET-MG) or ten (PITT) specimens were tested for each condition. Specimens exhibiting splitting and some in which slip data was lost during the test are excluded from average data reported in Table 5.1; therefore, the number of specimens (n) reported for each value varies.

Table 5.1 – Pull-out tests results.

Bar type	ASTM A615 Gr. 60 steel		Helically wrapped GFRP		ASTM A615 Gr. 60 steel		GFRP with machined ribs		Sand-coated GFRP		Most sand removed GFRP
Test series	CEFET-MG						PITT				
Bar nomenclature	#2 steel	#3 steel	#2 hGFRP	#3 hGFRP	#4 steel	#6 steel	#4 rGFRP	#6 rGFRP	#4 sGFRP	#5 sGFRP	#5 sGFRP-s
Image of the bar (all images are not in the same scale)											
Concrete batch	C1	C2	C1	C2				C3			
Nominal d_b (mm)	6.3	9.5	6.3	9.5	12.7	19	12.7	19	12.7	15.9	15.9
Nominal A_b (mm²)	31	71	31	71	127	284	127	284	127	199	199
Measured A_b (mm²)	-	-	-	-	119	269	146	321	122	219	215
Density (g/ cm³)	-	-	-	-	7.891	7.813	2.131	2.155	2.157	1.932	1.948
E_b (MPa)	200	200	28	37	200	200	60.3	60.3	46.9	48.4	48.4
f_{fu} (MPa)	500	500	590	973	500	500	962	898	927	739	739
R_r (Eq. 2.1)	0.049	0.086	0.035	0.050	0.074	0.089	0.030	0.024	n.a.	n.a.	n.a.
s_r (mm)	4.4	6.2	15.4	13.3	8.6	11.8	10.2	10.4	n.a.	n.a.	n.a.
Cube size, b (mm)	200	200	200	200	200	200	200	200	200	200	200
Concrete batch	C1	C2	C1	C2				C3			
f'_c (MPa)	33.2	35.0	33.2	35.0	37.8	37.8	37.8	37.8	37.8	37.8	37.8
f_t (MPa)	3.1	2.9	3.1	2.9	2.2	2.2	2.2	2.2	2.2	2.2	2.2
$l_b = 5d_b$ (mm)	31.5	47.5	31.5	47.5	63.5	95	63.5	95	63.5	79.5	79.5
τ_{avg} at 0.05 mm slip (MPa)	1.90	3.44	1.90	1.77	7.22	8.35	3.31	4.89	5.39	7.64	5.07
COV	0.42	0.7	0.78	0.40	0.27	0.23	0.21	0.26	0.48	0.31	0.32
n	5	5	5	5	8	3	9	6	8	5	4
τ_{avg} at 0.10 mm slip (MPa)	3.25	4.99	3.87	2.28	8.85	10.78	3.97	5.82	5.83	8.96	6.27
COV	0.34	0.64	0.62	0.41	0.21	0.10	0.18	0.24	0.52	0.23	0.27
n	5	5	5	5	8	3	10	6	9	5	4
τ_{avg} at 0.25 mm slip (MPa)	6.36	8.66	8.95	3.89	13.00	15.60	5.80	8.04	6.66	9.98	7.79
COV	0.16	0.32	0.52	0.43	0.12	0.06	0.16	0.23	0.46	0.16	0.24
n	5	5	5	5	8	3	10	6	9	5	4

Bar type	ASTM A615 Gr. 60 steel		Helically wrapped GFRP		ASTM A615 Gr. 60 steel		GFRP with machined ribs		Sand-coated GFRP		Most sand removed GFRP
Test series	CEFET-MG						PITT				
Bar nomenclature	#2 steel	#3 steel	#2 hGFRP	#3 hGFRP	#4 steel	#6 steel	#4 rGFRP	#6 rGFRP	#4 sGFRP	#5 sGFRP	#5 sGFRP-s
Image of the bar (all images are not in the same scale)											
$\tau_{max,avg}$ (MPa)	11.39	14.92	18.40	11.94	16.45	20.47	12.51	14.35	7.33	10.78	10.87
COV	0.09	0.21	0.16	0.21	0.11	0.13	0.18	0.17	0.39	0.16	0.14
n	5	5	5	5	10	7	10	10	10	5	5
Average free end slip at τ_{max} (mm)	1.09	1.34	1.54	2.74	0.95	1.28	2.63	1.92	0.58	3.75	7.21
COV	0.11	0.15	0.19	0.10	0.22	0.24	0.11	0.18	0.53	0.89	0.22
n	5	5	5	5	10	7	10	10	10	5	5
Area under curve to 0.25 mm	0.92	1.37	1.18	0.62	2.26	2.74	1.00	1.48	1.36	2.08	1.49
COV	0.24	0.46	0.56	0.41	0.17	0.08	0.19	0.24	0.52	0.23	0.28
n	5	5	5	5	8	3	10	6	9	5	4
Area under curve to 1 mm	10.89	14.15	16.03	7.93	14.03	17.63	6.85	9.53	6.46	9.78	7.89
COV	0.10	0.27	0.27	0.33	0.12	0.13	0.16	0.22	0.44	0.16	0.21
n	5	5	5	5	7	3	10	6	9	5	4
k_b at τ_{max}	n.a.	n.a.	0.62	1.25	n.a.	n.a.	1.31	1.43	2.24	1.47[(a)]	1.45[(a)]

[(a)]Calculated based on average of steel bars results.

Figure 5.4 – Bond-stress slip curves for reinforcing bars: (a) #2 steel, (b) #3 steel, (c) #2 hGFRP, (d) #3 hGFRP, (e) #4 steel, (f) #6 steel, (g) #4 rGFRP, (h) #6 rGFRP, (i) #4 sGFRP, (j) #5 sGFRP, and (k) #5 sGFRP-s.

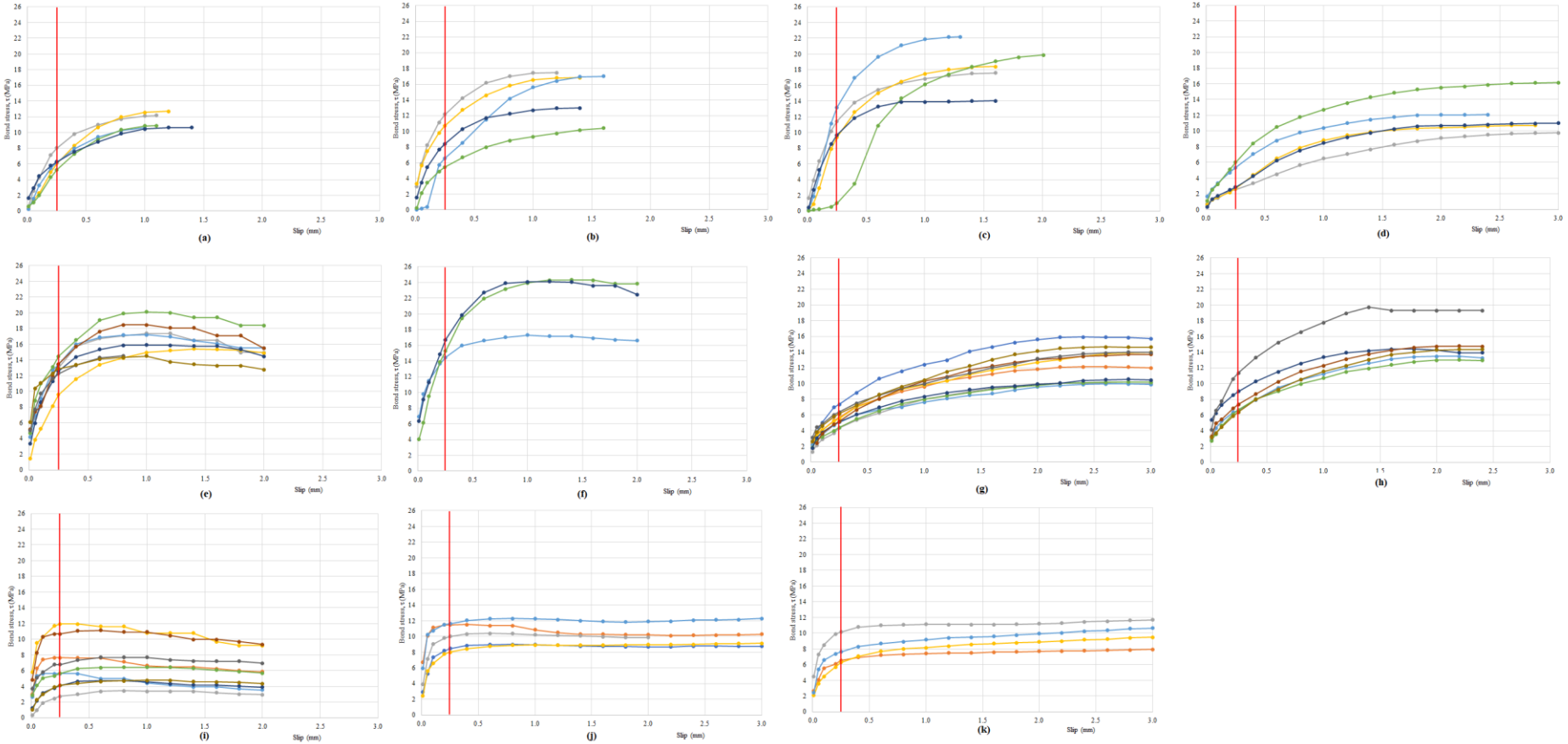

Source: author.

5.3 Discussion of the pull-out experimental results

The summary of the experimental ASTM D7913 pull-out test is presented in Table 5.1. Figure 5.5 shows a representative bond stress – slip curve for each type of bar. Stress-slip curves for all 80 tests are shown in Figure 5.4. All bars tested, except #4 sGFRP exceeded the minimum bond stress requirement of 7.6 MPa prescribed by ASTM D7957-22 (and 9.6 MPa prescribed by the ASTM D8505-23 for higher modulus bars) (see Section 2.1.2).

Figure 5.5 - Representative bond stress versus slip relationships from pull-out tests.

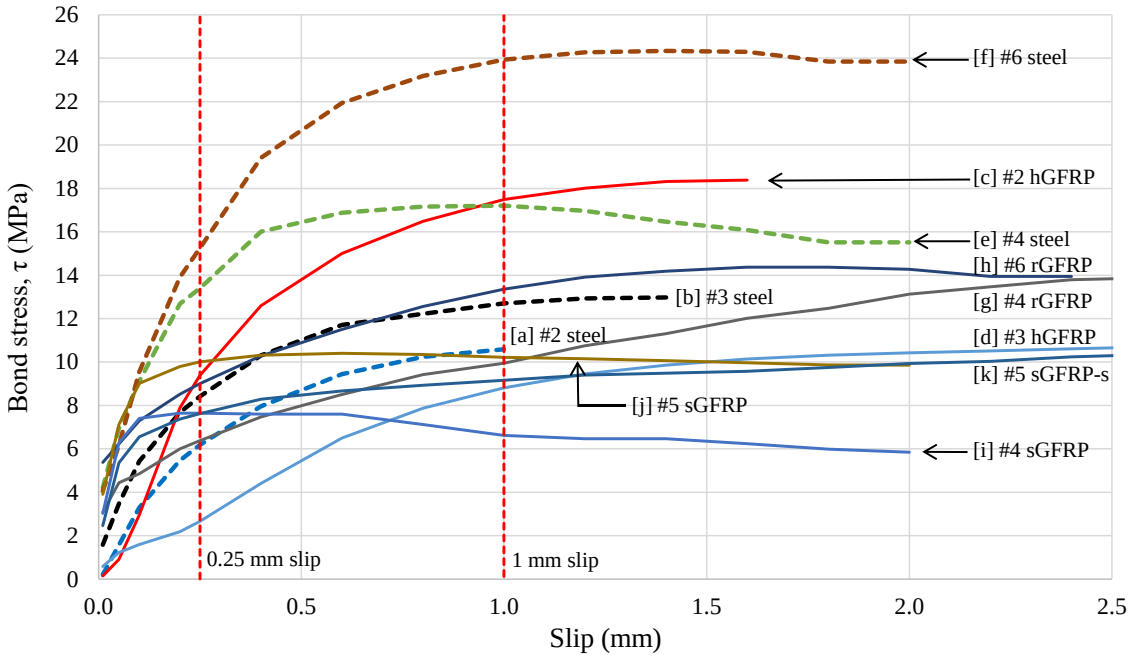

Source: author.

The fundamental bond stress-slip relationship is characterized by an initially stiff response followed by a softening behaviour until the maximum bond stress is achieved. Responses of the bars having deformations (steel, rGFRP, and hGFRP) exhibit a gradual degradation of stiffness followed until the maximum bond stress is achieved and maintained over a short plateau (Figure 5.5 curves a-h). Sand-coated, but otherwise undeformed bars, on the other hand, maintain their initially stiff response and achieve their peak bond stress at lower values of slip (Figure 5.5 curves i-k). After reaching their peak load, sand-coated bars exhibit a slight drop in bond capacity followed by a relatively long plateau at a lower residual bond capacity. Having some of the sand removed (#5 sGFRP-s; Figure 5.5 curve k), 'softened' the sand-coated behaviour to

an extent and the behaviour resembled more that of a ribbed bar, albeit with lower capacity (these bars had some helical deformation as seen in Table 5.1). The #5 bars having some sand coating removed (#5 sGFRP-s) exhibited similar average maximum bond stress to that of the #5 sGFRP bars (10.9 MPa and 10.8 MPa, respectively) but at approximately twice the ultimate slip: 7.2 mm for #5 sGFRP-s and 3.6 mm for #5 sGFRP (Table 5.1).

The average maximum bond stress, $\tau_{max,avg}$, of helically wrapped GFRP bars (#2 hGFRP and #3 hGFRP) and GFRP with machined ribs (#4 rGFRP and #6 rGFRP) was greater compared to the other GFRP surface types; the highest $\tau_{max,avg}$ value observed was 18.4 MPa for #2 hGFRP bar. By contrast, the value for $\tau_{max,avg}$ of the #2 steel bars tested was 11.4 MPa (Table 5.1).

The lowest bond stress among the GFRP bars was observed for the #4 sGFRP bar: 7.3 MPa (Table 5.1). This low bond capacity is attributed to the reduced mechanical engagement of sand-coated surface with the concrete. Sand coating has been reported to lead to an increase in the chemical bond component of bond (Chaallal and Benmokrane, 1993; Nanni et al., 1997); however, as most sand is embedded and encased in the vinyl-ester bar matrix material, it is unclear how chemical bond can be enhanced. Further investigation of the relatively poor performance of the sand-coated bars in the ASTM D7913 test, despite good performance in the prism tests (reported below) is reported in Chapter 7.

#4 and #6 steel, and #2 helically wrapped GFRP exhibited the ‘toughest’ behaviour: having the greater energy absorption through a slip of 1 mm. With the exception of the #2 helically wrapped GFRP bar, the GFRP bars, regardless of surface deformation, exhibited approximately one-half of the energy absorption of the corresponding diameter steel bars. The energy absorption behaviour may reflect service performance of bars in cases of fatigue loading, for instance. It is well-established that GFRP bars do not perform well in fatigue loads and that transient loads should be limited to 20% of the bar strength (ACI PRC 440.1R-15).

In all cases, except #2 bars, pull-out tests of steel bars of the same diameter exhibited greater bond stresses than GFRP bars, regardless of surface treatment. In addition, the slips corresponding to the maximum bond stress in steel bars were smaller than for the comparable GFRP bars despite the higher bond stresses achieved. This observation reflects the effect of the lower modulus of the GFRP material (Table 4.2).

Although it is implied that the bars having "relative rib area", $R_r \geq 0.05$ present adequate bond performance (Sections 2.1.2 and 4.2.3.2), the experimental results showed that bars that did not meet this requirement – #2 hGFRP, #4 rGFRP, and #6 rGFRP bars – presented satisfactory values of bond stress compared to the other bars (Table 5.1). For example: R_r for #2 hGFRP is only 0.035 and τ_{max} is 18.4 MPa, while for #2 steel bar R_r is 0.05 and τ_{max} is 11.4 MPa. Based on the experimental results, it is seen that the geometry of deformed bars has no significant influence on their maximum bond capacity. The geometry, however, does affect the shape of the bond-slip behaviour relationship.

The range of k_b values determined from the pull-out tests was broad. Only the #2 hGFRP bar showed better bond behaviour than comparable steel with k_b = 0.62. Other non-sand-coated GFRP bars tested exhibited k_b in the range of 1.25 to 1.43; similar to that recommended by ACI PRC 440.1R-15 and Shield et al. (2019). As noted above, the sand-coated bars performed poorly in the ASTM D7913 test and, contrary to recommendations from the literature, exhibited k_b values greater than non-sand-coated bars.

5.3.1 Statistical analysis

The one-way analysis of variance (ANOVA) was carried out to verify if there are statistically significant differences between the results obtained. ANOVA was performed using RStudio software, version 2023.06.2-561 considering 5% level of significance, where the null hypothesis (H_0) is that if there is no statistical difference between the bond behaviours of bars considered, otherwise, the alternative hypothesis (H_1) is attributed. Thus, if "*p-values*", (probability of accepting the null hypothesis [H_0]) is equal or greater than the level of significance (0.05), condition H_0 is selected, whereas if *p-value* < 0.05, then H_1 is considered.

Considering steel and GFRP bars having the same diameters, ANOVA showed that type of bar has influence on maximum bond stress, τ_{max}, for all bars analyzed: #2 steel and #2 hGFRP (*p-value* = 0.001); #3 steel and #3 hGFRP (*p-value* = 0.001); #4 steel, #4 rGFRP and #4 sGFRP (*p-value* < 0.0001); and #6 steel and #6 rGFRP (*p-value* = 0.0002).

For GFRP bars having same surface configuration and different diameters, ANOVA showed that there is statistical difference and bar diameter does affect the estimation of τ_{max} for #2

hGFRP and #3 hGFRP bars (*p-value* = 0.006) and #4 sGFRP and #5 sGFRP bars (*p-value* = 0.03); while for #4 rGFRP and #6 rGFRP, ANOVA showed that the bar diameter does not affect τ_{max} (*p-value* = 0.09).

Taking into account GFRP bars having the same diameter but different surface configurations, ANOVA confirms the experimental results for #5 sGFRP and the #5 sGFRP-s bars, indicating that there is no statistical difference between the bond behaviour of these bars (*p-value* = 0.93), while for #4 rGFRP and #4 sGFRP, ANOVA indicated that the surface deformation does affect the maximum bond stress (*p-value* = 0.0002).

The bond behaviour of the bars tested in this study was also statistically correlated using a two-tailed "*t-test*", which compares the means of two groups and determines if there is a statistically significant difference between them. The resulting "*p-values*" are provided in Table 5.2. Results for both maximum bond stress and bond stress at 0.25 mm slip are shown in opposing quadrants of the matrix in Table 5.2. The resulting *p-value* ≥ 0.05 (highlighted in bold) shows that the correlated bars have statistically similar values of bond stress; this is partially due to the high degree of variation inherent in bond testing.

Table 5.2 – Correlation matrix of bond behaviour of the bars tested.

Bar nomenclature / *p*-value	#2 steel	#3 steel	#2 hGFRP	#3 hGFRP	#4 steel	#6 steel	#4 rGFRP	#6 rGFRP	#4 sGFRP	#5 sGFRP	#5 sGFRP-s
#2 steel	1.0000	**0.1216**	**0.2620**	0.0216	0.0001	0.0001	**0.3023**	**0.1046**	**0.8385**	0.0030	**0.1812**
#3 steel	0.0418	1.0000	**0.9083**	0.0110	0.0040	0.0067	0.0098	**0.6688**	**0.2531**	**0.3884**	**0.6104**
#2 hGFRP	0.0011	**0.1099**	1.0000	**0.0524**	0.0423	**0.0569**	**0.0537**	**0.6705**	**0.2883**	**0.6553**	**0.6584**
#3 hGFRP	**0.6591**	**0.1335**	0.0061	1.0000	0.0001	0.0001	0.0119	0.0037	**0.0896**	0.0004	0.0124
#4 steel	0.0001	**0.2496**	**0.1419**	0.0016	1.0000	0.0261	0.0001	0.0001	0.0001	0.0063	0.0004
#6 steel	0.0001	0.0085	**0.2451**	0.0003	0.0020	1.0000	0.0001	0.0003	0.0007	0.0016	0.0013
#4 rGFRP	**0.3056**	**0.1045**	0.0008	**0.6588**	0.0004	0.0001	1.0000	0.0057	**0.4045**	0.0001	0.0183
#6 rGFRP	0.0220	**0.7004**	0.0141	**0.0943**	0.0422	0.0002	**0.0967**	1.0000	**0.3400**	**0.0990**	**0.8400**
#4 sGFRP	0.0099	0.0004	0.0001	0.0095	0.0001	0.0001	0.0003	0.0001	1.0000	0.0454	**0.5141**
#5 sGFRP	**0.5030**	0.0307	0.0011	**0.4142**	0.0001	0.0001	**0.1572**	0.0123	0.0288	1.0000	**0.0993**
#5 sGFRP-s	**0.5327**	0.0304	0.0010	**0.4348**	0.0001	0.0001	**0.1688**	0.0126	0.0237	**0.9324**	1.0000

Correlation for maximum bond stress, $\tau_{max.}$
Correlation for bond stress at 0.25 mm slip, $\tau_{0.25.}$

5.4 Experimental database

In addition to the 80 specimens tested in the present study, 137 comparable ASTM D7913 pull-out tests reported by Sólyom and Balázs (2020) are considered in order to capture a broader view of the bond characteristics of GFRP bars. Details of the complete database, including the bars reported in this study (for completeness and ease of comparison), are given in Appendix E. k_b factors are reported only where a direct comparison with steel bars tests (for which k_b = 1.0) is available. Sólyom and Balázs tested a range of sand-coated, helically wrapped and sand-coated, and machine-deformed GFRP bars. A summary of all bond stress results is shown in Figure 5.6. The vertical red dashed line in Figure 5.6 is 7.6 MPa, the minimum value of bond stress required by ASTM D7957. It is seen that, with the single exception of #4 sGFRP tested in this study, all bars exceed this value.

Sólyom and Balázs tested bars embedded in normal-strength concrete (NSC) and high-strength concrete (HSC), having f_c' = 35.3 MPa and 66.1 MPa, respectively. For the sake of comparison, the NSC is comparable to that used in the present study (Table 4.1). As expected, and clearly seen in Figure 5.6, the bond strength achieved in HSC exceeds that of NSC approximately in the proportion of $(f_c')^{0.5}$. This validates the ACI PRC 440.1R-15 and ACI CODE 440.11-22 bond development length relationships that are proportional to $(f_c')^{0.5}$. In North American practice, concrete tensile capacity is expressed as a function of $(f_c')^{0.5}$, illustrating the correlation between bond capacity and local cracking in the vicinity of the embedded bar (see Figure 2.2b).

With the exception of 6 mm bars (#2 bars) embedded in NSC, there are no clear trends with respect to bond stress found in pull-out tests. Steel (dashed entries in Figure 5.6) and GFRP (solid entries) bars exhibit comparable behaviour and there is little to differentiate sand-coated GFRP bars (shaded entries) from other GFRP deformation types. Apart from the smallest 6 mm bars reported, k_b is generally greater than unity. Excluding 6 mm bars, the average value of k_b reported is 1.37.

Bars smaller than 10 mm or #3 bars are rarely used in structural reinforced concrete practice. Nonetheless, the 6 mm (#2 bars) exhibit a different trend with GFRP bars outperforming steel bars, and sand-coated GFRP bars being generally superior to non-sand-coated GFRP bars. It is

noted however, that the bond stress reported for 6 mm steel bars is lower than that for other steel bars tested; this leads to lower calculated k_b values.

The high degree of variability (one standard deviation error bars are shown in Figure 5.6) is also apparent and must be considered when drawing comparisons between bars or assessing apparent trends.

Figure 5.6 – Bond stress from ASTM D7913 test (MPa).

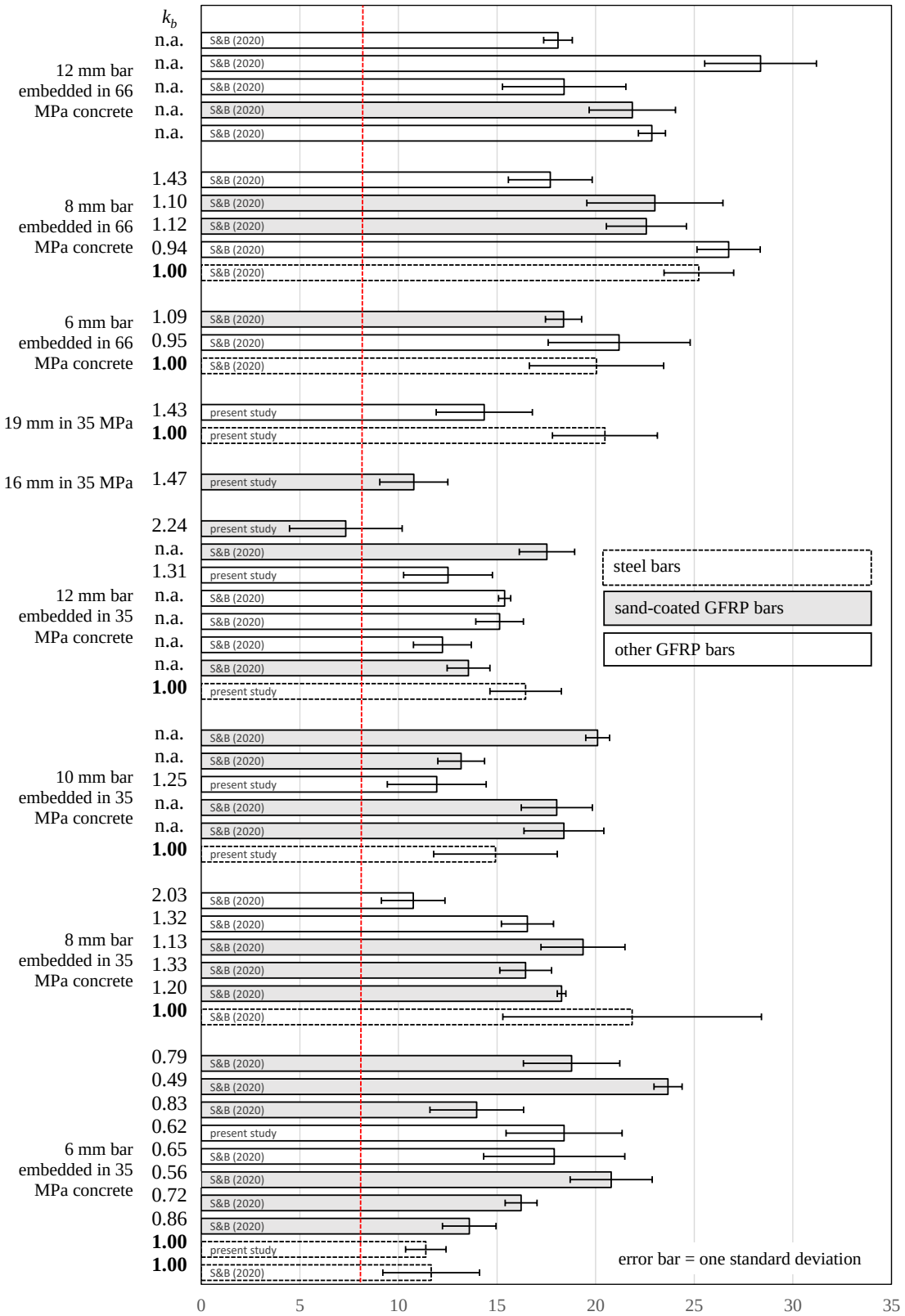

Source: author.

Figure 5.7 shows the maximum bond stress, τ_{max}, *versus* "relative rib area", R_r, for the specimens assessed in this study and in the study performed by Sólyom and Balázs fabricated with NSC. As a reference, the lower limit of R_r, i.e., $R_r \geq 0.05$ – indicating satisfactory bond behaviour – is highlighted. Bond-dependent coefficient, k_b, *versus* R_r is plotted in Figure 5.8. The thresholds of $k_b < 1.0$ and $R_r \geq 0.05$ suggest bars with improved bond performance. It is seen that there is no trend that can be established between τ_{max} and R_r, and k_b and R_r.

Figure 5.7 – Maximum bond stress *versus* relative rib area.

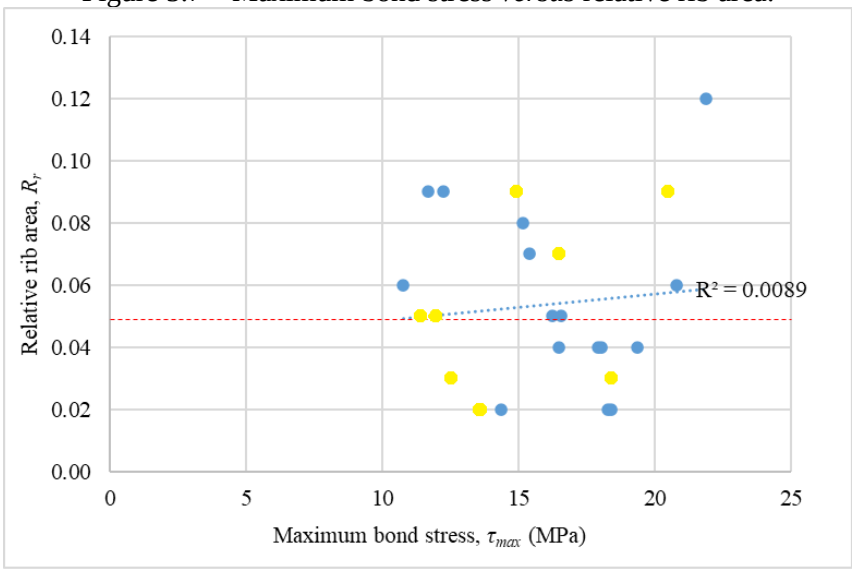

This study.
Sólyom and Balázs (2020) for f'_c = 35.3 MPa.

Source: author.

Figure 5.8 – Relative rib area *versus* bond-dependent coefficient.

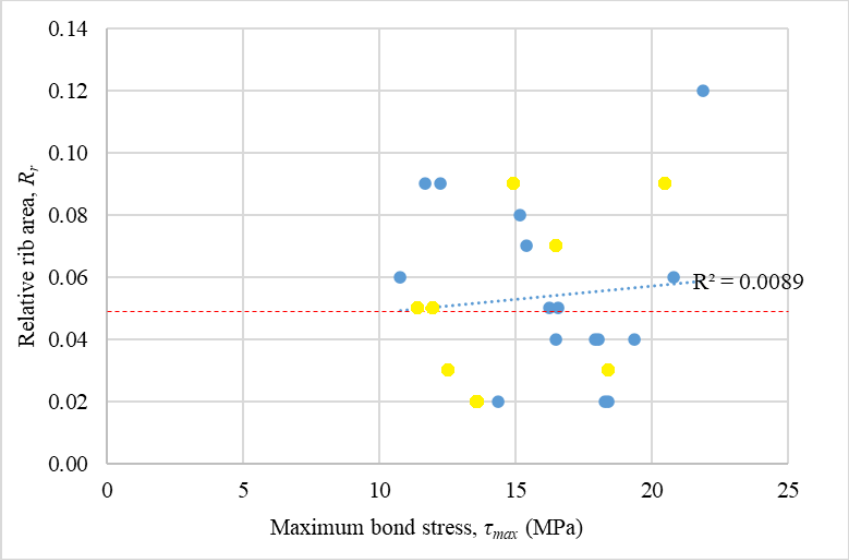

This study.
Sólyom and Balázs (2020) for f'_c = 35.3 MPa.

Source: author.

By comparing specimens fabricated with NSC and HSC in the study of Sólyom and Balázs, it is observed that there is no trend between τ_{max} and R_r (Figure 5.9), and R_r and k_b (Figure 5.10), independent of the concrete compressive strength. Plotting τ_{max} *versus* k_b, it can be concluded that GFRP bars presented improved bond behaviour in normal strength concrete (k_b < 1.0) (Figure 5.11). In total, 9 GFRP bar types – out of the 18 whose k_b was estimated – presented better bond behaviour than comparable steel bars (Table E.1); of these, 8 bar types were embedded in normal-strength concrete and 2 types in HSC (Figure 5.11).

Figure 5.9 – Maximum bond stress *versus* relative rib area for data of Sólyom and Bálazs study.

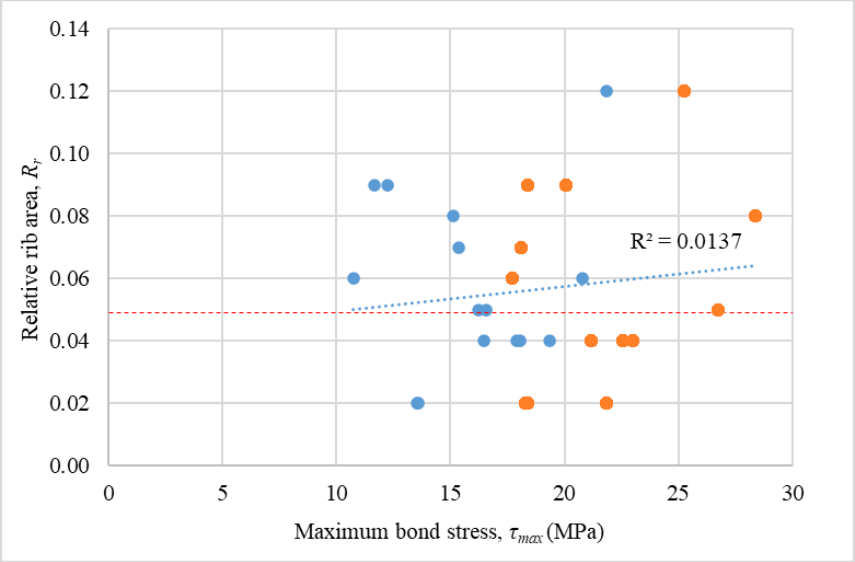

Normal strength concrete (NSC).
High strength concrete (HSC).

Source: author.

Figure 5.10 – Relative rib area *versus* bond-dependent coefficient for data of Sólyom and Bálazs study.

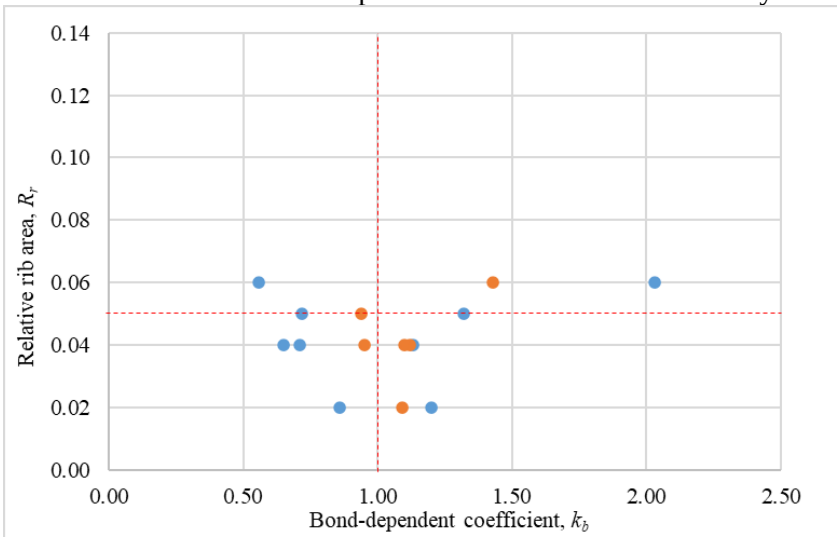

Normal strength concrete (NSC).
High strength concrete (HSC).

Source: author.

Figure 5.11 – Maximum bond stress *versus* bond-dependent coefficient for data of Sólyom and Bálazs study.

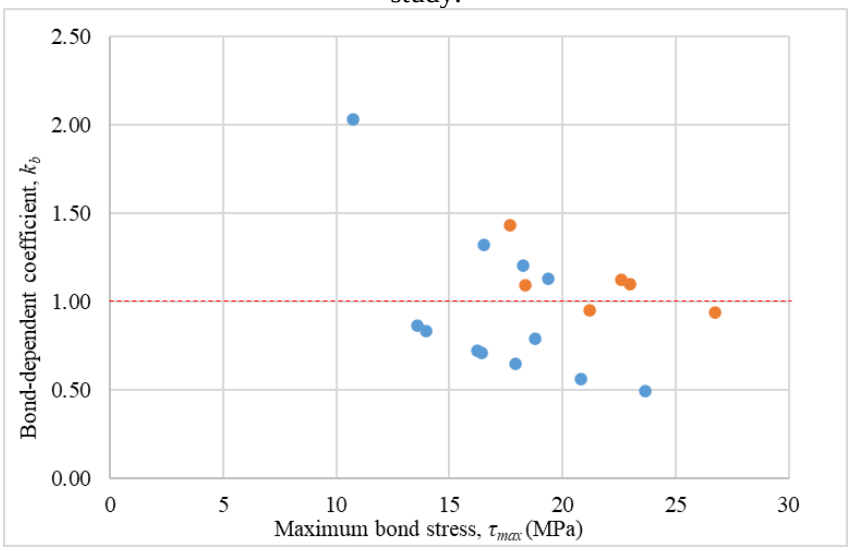

Normal strength concrete (NSC).
High strength concrete (HSC).

Source: author.

5.4.1 Statistical analysis

Analysis of Variance (ANOVA), also considered 5% of significance level, was used to assess the effect of some parameters and their interactions in the maximum bond stress, τ_{max}, response. A *p-value* lower than significance level of 0.05 indicates the presence of significant effects.

For all GFRP bars tested in NSC and HSC, the surface configuration and concrete compressive strength have been shown to influence maximum bond stress (*p-value* < 0.0001 in both cases). Tukey's test, at a 5% significance level, showed that there is no statistical difference for the obtained bond stresses for different bar diameters of GFRP bars. The greatest bond stresses were found for sand-coated GFRP bars, while the lowest were found for fine sand-coated GFRP bars. Tukey's test confirmed that the greatest τ_{max} are related to GFRP bars embedded in HSC (Figure 5.6).

Considering steel bars, helically wrapped, helically wrapped and sand-coated, and indented GFRP bars having 6- and 8-mm diameters in NSC and HSC, ANOVA showed that the bar diameter (*p-value* = 0.001), surface configuration (*p-value* < 0.0001), and concrete strength (*p-value* < 0.0001) does affect the maximum bond stress, although the bar diameter has less influence. Tukey's test confirmed that the greatest τ_{max} were found for 8mm GFRP bars (Figure

5.6). No statistical differences on bond stress were observed between steel bars, helically wrapped, and helically wrapped and sand-coated GFRP bars. Analysing the influence of rib ratio and concrete strength for these bars, ANOVA indicated that both parameters have influence on the maximum bond stress (*p-value* < 0.0001 in both cases). It is worth noting that Sólyom and Balázs estimated the rib ratio differently from Equation [2.1] used in this study. Sólyom and Balázs estimated R_r as the ratio between the projected rib area to the nominal bar perimeter multiplied by the rib spacing. Tukey's test showed that the greatest bond stresses were found for bars having R_r = 0.12, although bars having R_r equal to 0.02, 0.04, and 0.05 presented values of bond stresses varying from 13 to 30% of that determined when R_r = 0.12.

Comparing the results of this study and the study of Sólyom and Balázs: for steel bars of 6.3 mm diameter in normal-strength concrete considering different cube sizes (150 and 200 mm), ANOVA showed that the size of the specimen did not affect the maximum bond stress (*p-value* = 0.85); in the same way, for helically wrapped GFRP bars of 6.3 mm in NSC and 150 and 200 mm cube sizes, ANOVA also indicated that different specimen sizes have no effect on estimated bond stress (*p-value* = 0.84). This result is expected: provided the specimen was adequate to mitigate splitting, the pull-out strength is not expected to be affected by the dimension of the concrete specimen.

5.5 Summary of the chapter

In this chapter, the bond behaviour of different types of GFRP were presented – including the estimation of the bond-dependent coefficient, k_b. Eighty ASTM D7913 pull-out tests were performed in this study in two stages: #2 and #3 bars were tested at CEFET-MG (Brazil) and #4, #5 and #6 bars were tested at University of Pittsburgh (USA). The primary conclusions are as follows:

— the pull-out bond-slip behaviour of deformed bars (steel, ribbed GFRP, and helically wrapped GFRP) exhibited a gradual degradation of stiffness until the maximum bond stress which was maintained over a short plateau;

— the pull-out bond-slip behaviour of sand-coated GFRP bars exhibited an initially stiffer response with the maximum bond stress being achieved at lower values of slip followed by a relatively long plateau at a lower residual bond capacity;

— having some of the sand removed 'softened' the sand-coated behaviour to an extent and the behaviour resembled more that of a ribbed bar, albeit with lower capacity. The #5 bars having some sand coating removed (#5 sGFRP-s) exhibited similar average maximum bond stress to that of the sand-coated #5 sGFRP bars but at approximately twice the ultimate slip;

— among the GFRP bars tested, the greatest average bond stress was 18.4 MPa for #2 helically wrapped GFRP bar, while #4 sand-coated GFRP bars exhibited the lowest bond stress: 7.3 MPa;

— only the #2 helically-wrapped GFRP bar showed better bond behaviour than comparable steel with $k_b = 0.62$. Other non-sand-coated GFRP bars tested exhibited k_b in the range of 1.25 to 1.43;

— #4 sand-coated bars performed poorly in the ASTM D7913 test and, contrary to recommendations in the literature, exhibited k_b value greater than non-sand-coated bars: $k_b = 2.24$;

— considering steel and GFRP bars having the same diameter, ANOVA showed that type of bar has influence on maximum bond stress for all bars analyzed (*p-value* < 0.05);

— for GFRP bars having the same surface configuration and different diameters, i.e., #2 and #3 hGFRP and #4 and #5 sGFRP bars, ANOVA showed that bar diameter does affect the estimation of maximum bond stress (*p-value* < 0.05). On the other hand, bar diameter has been shown to not affect bond stress of #4 and #6 rGFRP bars (*p-value* > 0.05);

— ANOVA indicated no statistical difference between the bond behaviour of #5 sGFRP and the #5 sGFRP-s bars (*p-value* = 0.93);

— for #4 rGFRP and sGFRP, ANOVA showed that the surface deformation does affect the maximum bond stress (*p-value* = 0.0002).

To supplement pull-out test data and assess the utility of the test method, a complementary dataset of 137 tests reported by Sólyom and Balázs (2020) was analysed alongside the present data. The Sólyom and Balázs tests were conducted in normal- and high-strength concretes using 36 bar types. The conclusions are as follows:

— the greatest bond stresses were found for specimens fabricated with high strength concrete, independent of the surface configuration of the bar - bond strength was proportional to $(f_c')^{0.5}$;

— with the exception of 6 mm bars (#2 bars) embedded in normal strength concrete, there are no clear trends with respect to bond stress found in pull-out tests. Steel and GFRP bars exhibit comparable behaviour and there is little to differentiate sand-coated GFRP bars from other GFRP deformation types. Excluding 6 mm bars, the average value of k_b reported is 1.37;

— considering only the specimens fabricated with normal-strength concrete, no trend between maximum bond stress and “relative rib area”, or “relative rib area” and bond-dependent coefficient was observed;

— comparing specimens in NSC and HSC, no trend was observed between maximum bond stress and “relative rib area”, and “relative rib area” and bond coefficient, independent of the concrete compressive strength;

— 7 out of 11 GFRP bars embedded in NSC whose k_b could be estimated exhibited improved bond behaviour ($k_b < 1.0$); and 9 out of 18 GFRP bar types – including NSC and HSC – presented better bond behaviour than comparable steel bars ($k_b < 1.0$);

— for all GFRP bars tested in NSC and HSC, the surface configuration and concrete compressive strength have been shown to influence maximum bond stress (*p-value* < 0.05);

— Tukey’s test showed that the greatest bond stresses were found for sand-coated GFRP bars and for 8 mm diameter GFRP bars;

— considering steel bars, helically wrapped, helically wrapped and sand-coated, and indented GFRP bars having 6- and 8-mm diameters in NSC and HSC, ANOVA showed that the bar diameter, surface configuration, and concrete strength does affect the maximum bond stress (*p-value* < 0.05);

— analysing the influence of rib ratio and concrete strength of steel bars, helically wrapped, and helically wrapped and sand-coated GFRP bars, ANOVA indicated that both parameters have influence on the maximum bond stress (*p-value* < 0.05). Tukey’s test showed that the greatest bond stresses were found for bars having $R_r = 0.12$, although bars having R_r equal to 0.02, 0.04, and 0.05 presented values of bond stresses varying from 13 to 30% of bond stresses for these bars.

Performing statistical analysis to compare the results obtained in this experimental program with the results presented by Sólyom and Balázs, it is possible to conclude that:

— for steel bars of 6.3 mm diameter in normal-strength concrete considering different cube sizes (150 and 200 mm), ANOVA showed that the size of the specimen did not affect the maximum bond stress (*p-value* = 0.85); and

— for helically wrapped GFRP bars of 6.3 mm in NSC embedded in 150 and 200 mm cube sizes, ANOVA also indicated that different specimen sizes have no effect on the estimated bond stress (*p-value* = 0.84).

6

PRISM TENSION TEST

An experimental series of prism tension tests is described in this chapter. The non-standard prism tension test has the advantage of providing qualitative, in addition to quantitative comparison of cracking behaviour as it is affected by reinforcing bar type. Conventional steel bars were included in the experimental program as control specimens; this permits a direct comparison of performance controlling for concrete details and any experimental set-up bias.

The results of the prism tests are compared to the results of the pull-out tests presented in Chapter 5 to better understand overall bond performance. This chapter begins with a description of the non-standard prism tension test. The test details are then described. Finally, the observed cracking behaviour is analyzed and discussed.

6.1 Introduction

The cracking response of a reinforced concrete member is affected by the interaction between the reinforcing bar and the concrete, i.e., the bond behaviour. Such interaction allows the concrete between cracks to contribute to resisting tensile forces and provides additional stiffness – the so-called *tension stiffening* effect (see Section 2.1.1). In a reinforced concrete prism in tension, the applied load – applied only to the bar in this case – is, nonetheless, shared between the reinforcement and the concrete according to their respective elastic stiffness. At cracking, both steel and concrete are resisting tension in a linear manner: $f_s < f_y$, and concrete tensile stress has just reached f_{ct}. Once the tensile stress in the concrete is exceeded, "primary" cracks appear; their spacing is a function of bond as described in Section 2.1.4.3. After cracking, slip occurs between the reinforcement and concrete at the crack, relieving the tensile stress in the concrete adjacent to the crack. At a crack location, concrete tensile stress is zero and the transfer of tensile stress from bar to concrete between cracks continues until the tensile capacity of the concrete is exceeded again and new cracks appear. This process repeats until the final cracking

configuration is attained. From the final crack pattern, bond characteristics can be inferred as described in this chapter. Details of the development of bond stresses in a prism specimen are presented in Section 2.1.4.3.

6.2 Test details

All the prism tension tests were conducted at University of Pittsburgh (USA) using C3 concrete (see Section 4.1).

6.2.1 Test specimens

In total, 12 long prism specimens were tested. The bars were positioned horizontally in the center of the wood forms and were long enough to have sufficient exposed length to permit gripping in the testing frame (Figure 6.1a). The concrete was cast in two layers and vibrated by a mechanical wand vibrator, with care taken to avoid displacement of the positioned bar (Figure 6.1b). After casting, specimens were covered to cure. The concrete used is that reported as C3 in Table 4.1.

Figure 6.1 – Details of prism forms.

a) Prism forms pior concrete casting. b) Prism forms after concrete casting.

Source: author.

Because cracking is highly variable, long prismatic specimens are desirable to permit multiple primary cracks to form from which an average crack spacing, s_{avg}, can be determined. The length of the specimens was selected to be 150 times the bar diameter ($150d_b$). To better compare results and represent typical steel reinforced concrete details, the reinforcement ratio, ρ_f, was set equal to 0.013. As a result, the square prism section dimension, b, and length, L, vary

with the bar size tested. Details of the specimens are given in Table 6.1. Two or three repetitions of each prism were performed.

6.2.2 Test set-up and procedure

The test set-up, arranged as a self-reacting system using a steel girder as a reaction bed is shown in Figure 6.2. The reinforcing bar embedded in the long concrete prism was subjected to tension applied only to the protruding portions of the bar using a 200 kN capacity hollow-core hydraulic ram. Because it is not necessary to yield the reinforcing bar, commercially available bar anchors were used to secure both ends of the bar. These anchors are designed for use with steel reinforcing bars, but with some preparation of the bar, were adequate to anchor the GFRP bar to the stresses required to fully develop the prism cracking. Caution is noted: the anchors are not adequate to develop the ultimate capacity of the GFRP bars and should not be used for this purpose.

During testing, the prism is fully supported on the reaction frame (web of the W24 section shown in Figure 6.2). Fine sand is broadcast on the steel to minimise friction between the concrete prism and steel supporting surface.

Figure 6.2 – Prism tension test set-up (#6 steel shown).

Source: author.

Load was applied monotonically to develop a cracking history; as the cracks appeared, they were marked on the concrete prism and labeled as to their order of appearance. Due to the variability of both concrete tensile and bond properties, the primary crack pattern will establish itself over a small range of applied load, *N*. Once the primary crack pattern is established, increasing *N* will only widen the existing cracks. Secondary cracks may appear between established primary cracks although these are of little interest in terms of serviceability

behaviour. To provide meaningful data, the bars tested must remain elastic – which they do in all instances. The prisms tests used were adopted and refined from pilot tests reported by Silva et al. (2021) and Platt (2018).

6.2.3 Prism test results

Twelve concrete prisms reinforced with GFRP and steel bars were tested. The average crack width, w_{avg}, was computed using Equation [2.9], while the average bond stress, τ, and the bond-dependent coefficient, k_b, were calculated according to Equations [2.8] and [5.1], respectively. The occurrence of the initial crack was also used to directly calculate the concrete tension strength (Section 4.1 and Appendix C). The experimental results for all the specimens tested are presented in Table 6.1.

Table 6.1 – Prism tension test results (COV in parentheses).

	Prism	#4 steel		#6 steel			#4 rGFRP		#6 rGFRP			#4 sGFRP	
	Specimen	1	2	1	2	3	1	2	1	2	3	1	2
Prism size	Nominal d_b (mm)	12.7		19.1			12.7		19.1			12.7	
	b (mm)	100		150			100		150			100	
	L (mm)	1905		2860			1905		2860			1905	
	$A_c = b^2 - A_b$ (mm^2)	9873		22213			9873		22213			9873	
Bar	Nominal A_b (mm^2)	127		287			127		287			127	
	E_b (GPa)	200		200			60.3		60.3			46.9	
First crack	P_1 (kN)	22.2	23.7	46.3	39.8	52.8	20.0	31.5	49.9	33.3	49.7	28.1	32.8
	Bar stress (MPa)	175	187	162	139	184	158	249	174	116	173	222	259
	$1/f_y$	0.44	0.47	0.40	0.35	0.46	0.16	0.26	0.19	0.13	0.19	0.24	0.28
Final crack	P_2 (kN)	32.9	50.1	78.5	93.5	107.8	49.5	43.9	84.2	86.2	109.2	50.1	43.9
	Bar stress (MPa)	260	396	274	326	376	391	347	294	301	381	396	347
	$1/f_y$	0.65	0.99	0.68	0.82	0.94	0.41	0.36	0.33	0.33	0.42	0.43	0.37
End of test	P_3 (kN)	53.2	56.0	110.7	111.6	110.7	58.5	59.6	111.2	111.1	128.6	53.4	58.1
	Bar stress (MPa)	420	442	386	389	386	462	470	388	388	449	421	459
	$1/f_y$	1.05	1.11	0.97	0.97	0.97	0.48	0.49	0.43	0.43	0.50	0.45	0.50
Crack pattern	s_{avg} (mm)	173	146	191	204	239	173	190	286	260	205	89	127
	w_{avg} (mm)	0.15	0.13	0.17	0.18	0.21	0.50	0.55	0.83	0.75	0.59	0.33	0.47
Bond	τ (MPa)	6.42	7.58	8.70	8.14	6.96	6.42	5.83	5.81	6.39	8.12	12.41	8.75
	τ_{avg} (MPa)	7.00		7.93 (0.11)			6.13		6.77 (0.18)			10.58	
	k_b			1.0			1.14		1.17			0.66	

Figures 6.3 to 6.14 show final crack patterns and spacing of each tested prism. In these figures, the order of appearance of the cracks is shown on the sketch of the prism. The load at which

each crack appeared is shown to the left of the dimension line showing the location of the crack. In many cases, multiple cracks occurred at the same applied load.

Figure 6.3 – Prism test and crack pattern: #4 steel – specimen 1.

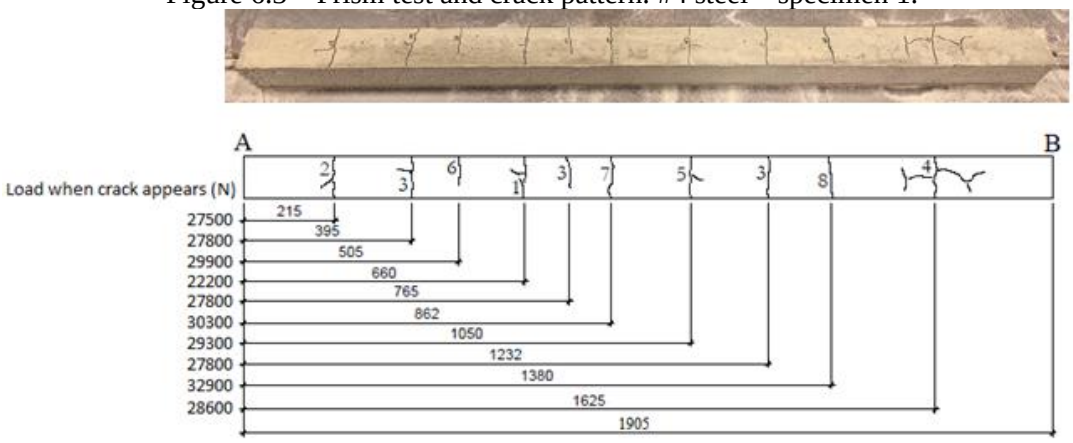

Source: author.

Figure 6.4 – Prism test and crack pattern: #4 steel – specimen 2.

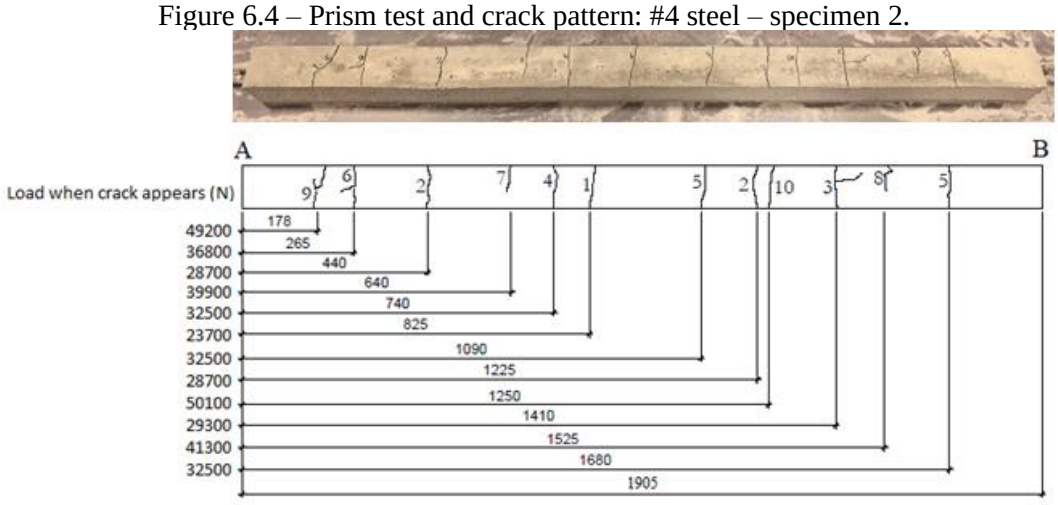

Source: author.

Figure 6.5 – Prism test and crack pattern: #6 steel – specimen 1.

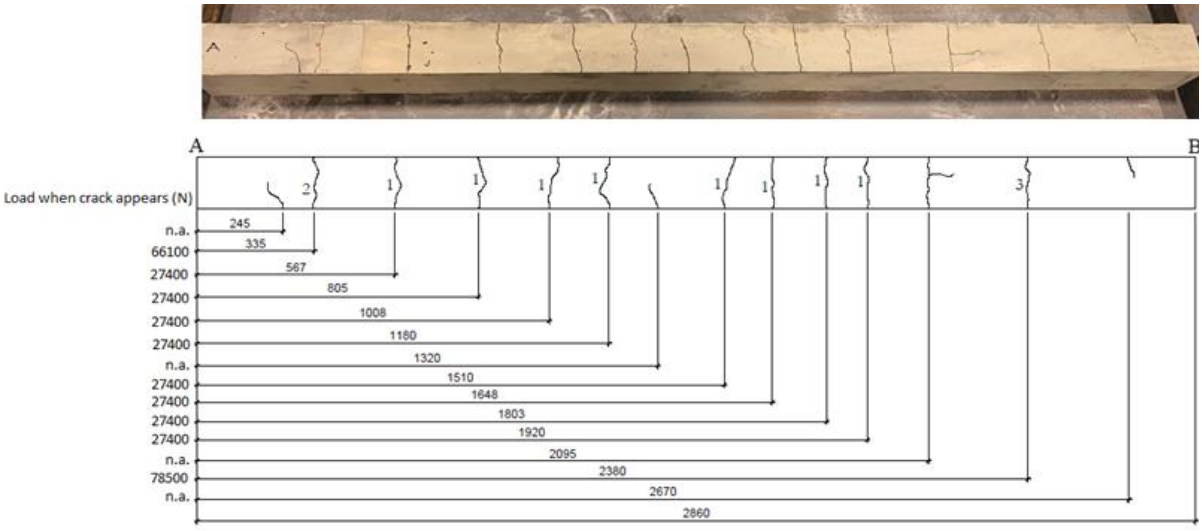

Source: author.

Figure 6.6 – Prism test and crack pattern: #6 steel – specimen 2.

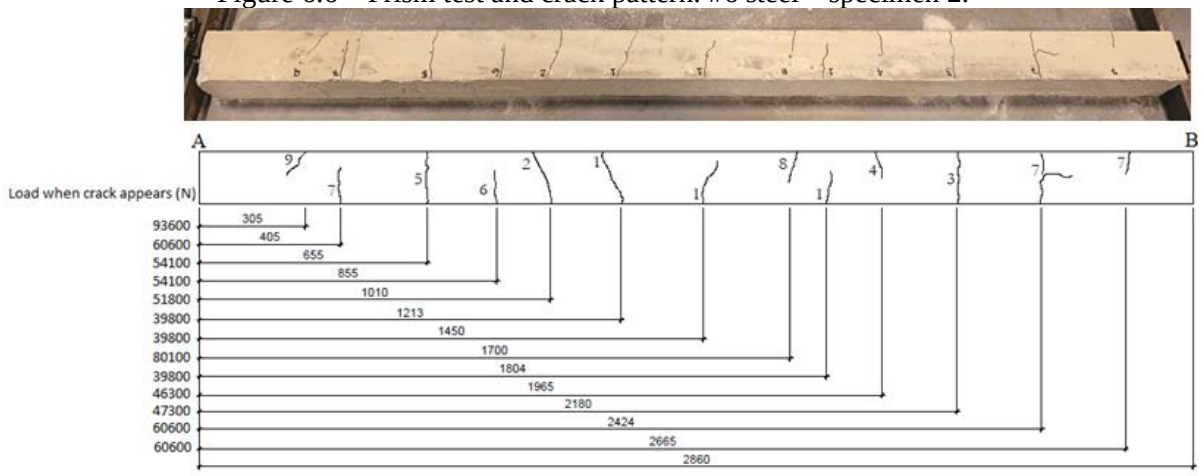

Source: author.

Figure 6.7 – Prism test and crack pattern: #6 steel – specimen 3.

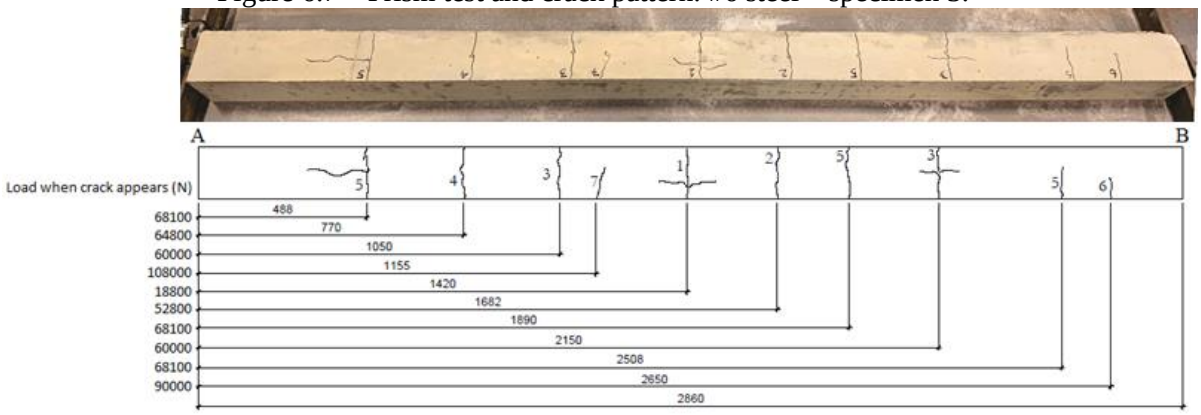

Source: author.

Figure 6.8 – Prism test and crack pattern: #4 rGFRP – specimen 1.

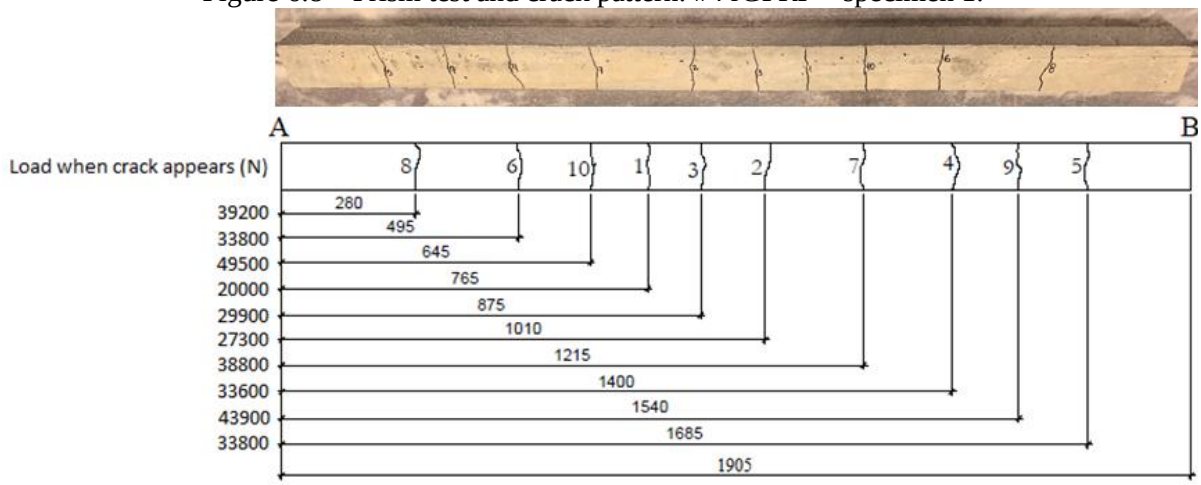

Source: author.

Figure 6.9 – Prism test and crack pattern: #4 rGFRP – specimen 2.

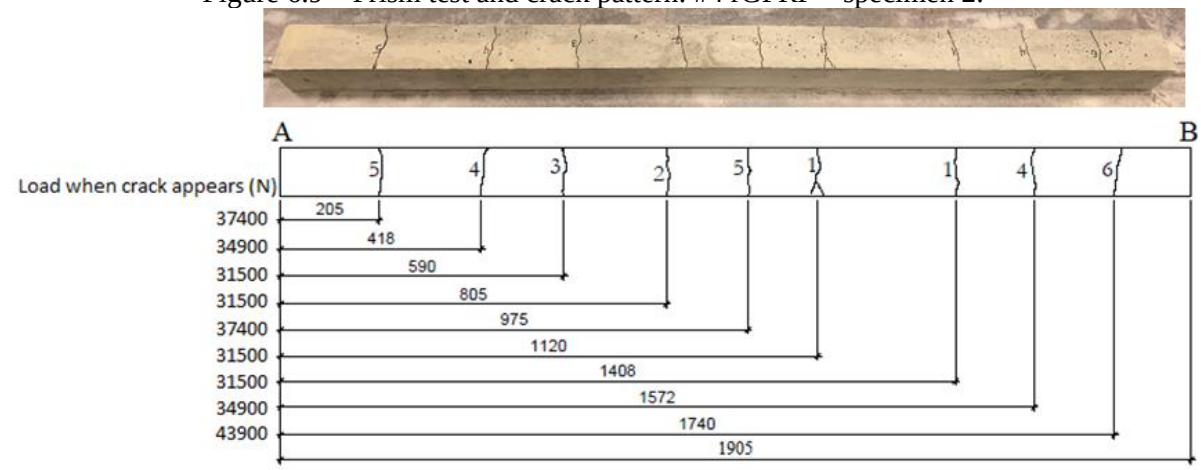

Source: author.

Figure 6.10 – Prism test and crack pattern: #6 rGFRP – specimen 1.

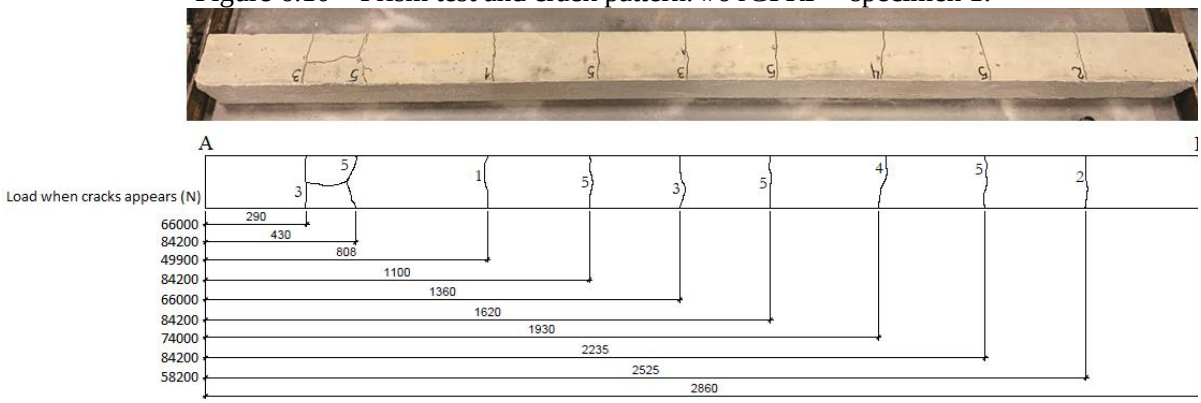

Source: author.

Figure 6.11 – Prism test and crack pattern: #6 rGFRP – specimen 2.

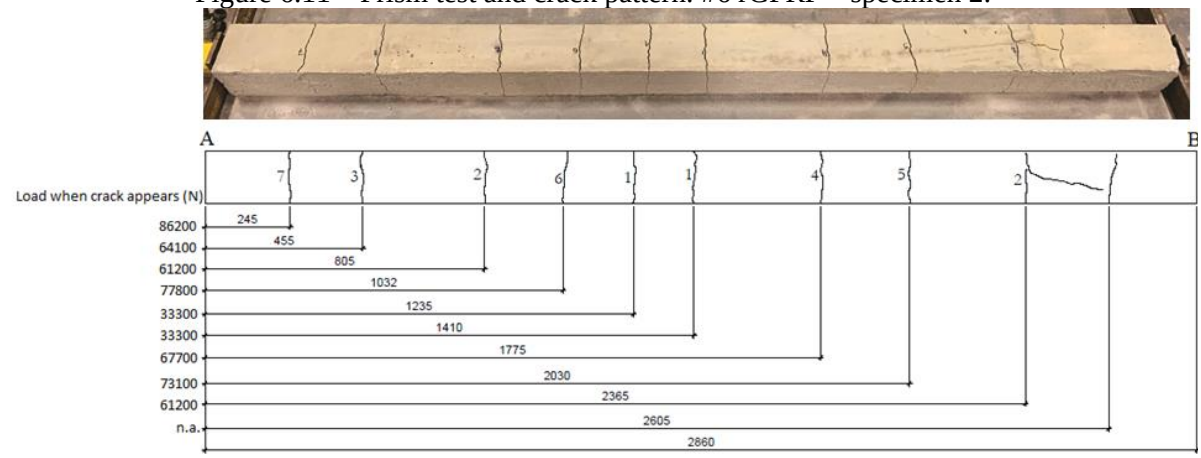

Source: author.

Figure 6.12 – Prism test and crack pattern: #6 rGFRP – specimen 3.

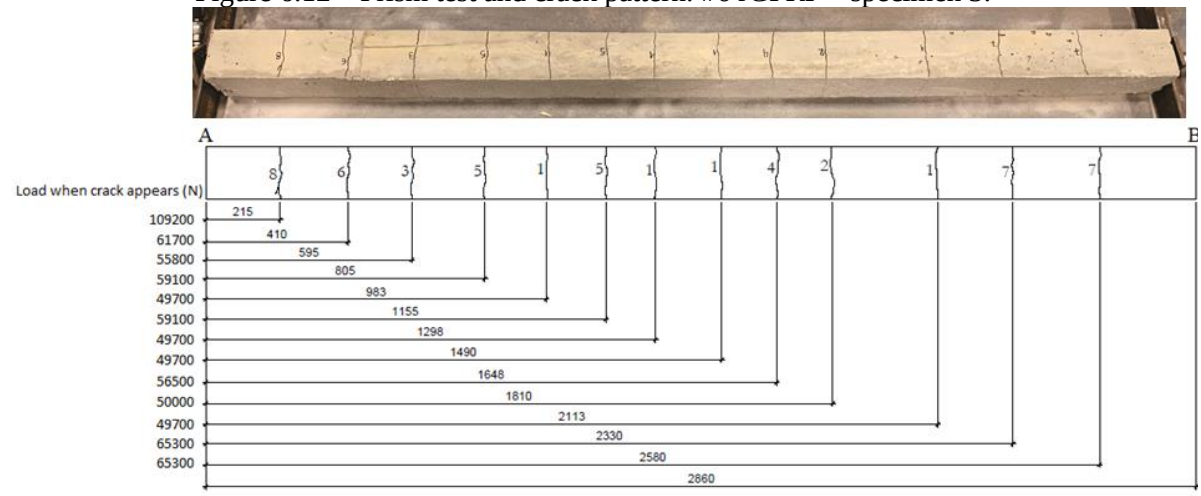

Source: author.

Figure 6.13 – Prism test and crack pattern: #4 sGFRP – specimen 1.

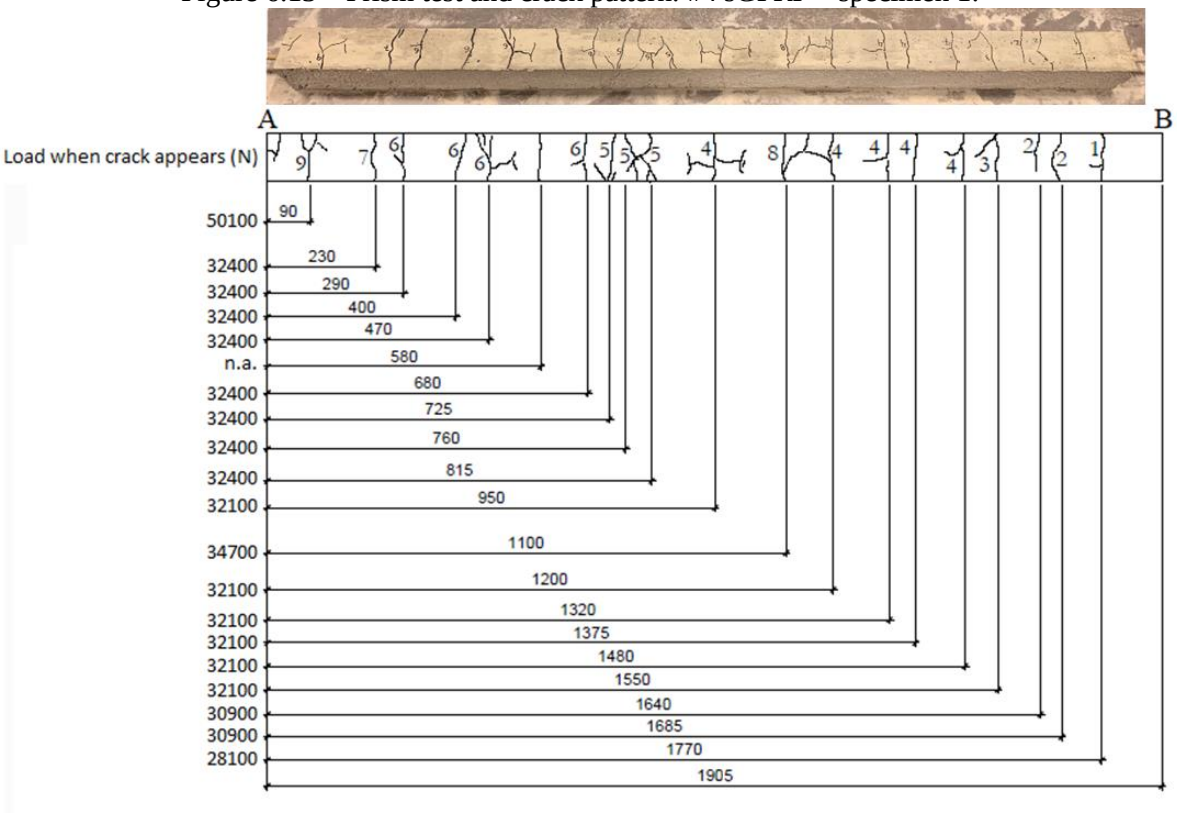

Source: author.

Figure 6.14 – Prism test and crack pattern: #4 sGFRP – specimen 2.

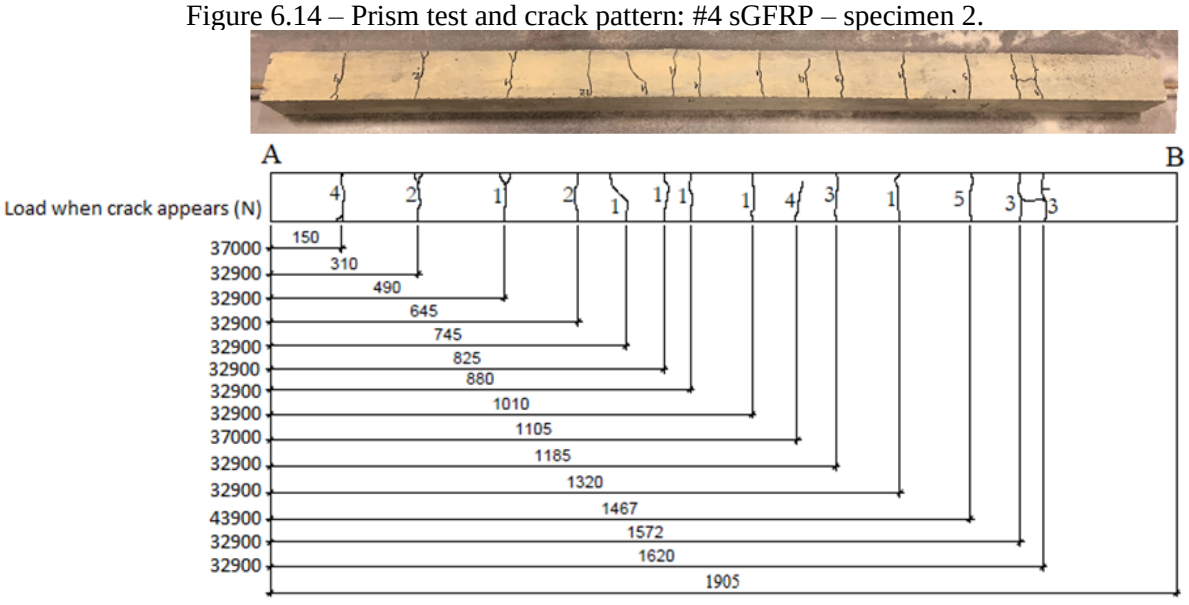

Source: author.

6.3 Discussion of the prism tension test results

The crack patterns of the prisms tested were recorded (Figure 6.3 to 6.14). In general, and as expected, first cracks appeared near to the middle of the prisms where the embedded bars are fully developed, having about $75d_b$ embedment length to either end of the prism. Subsequent cracks appeared across the length of the prisms between existing cracks. In this test, the prism ends are virtual cracks: locations having all force carried by the embedded bar. It was relatively easy to predict the appearance of subsequent cracks based on the distance between existing cracks: cracks appear between existing cracks that are further apart (longer embedment length). Eventually, no more cracks appear, and all additional strain results in existing cracks opening further. At this point, the distance between cracks, s, at all locations along the prism is inadequate to transfer sufficient stress to the concrete to result in an additional crack to form. The progression of the observed cracks corresponded with and confirmed the discussion of cracking summarized in Figure 2.8.

Cracks were primarily transverse to the prism. Small eccentricities were observed in some specimens resulting in some inclination of the cracks relative to the longitudinal axis; this likely occurred as a result of a small eccentricity in the bar location within the prism. As seen in Figure 6.3 to 6.14, these effects were minimal.

For all prisms, the bar stress at initial cracking (calculated using nominal bar area, A_b) averaged 183 MPa (COV = 0.23). From the bar stress at initial cracking and considering the transformed section properties of the prism, the concrete tensile capacity was estimated to be f_{ct} = 2.2 MPa (COV = 0.24) (see Appendix C). All cracks had developed fully at an average bar stress of 341 MPa (COV = 0.14), making clear that all bars remained elastic. Indeed, upon unloading the prisms, the crack widths closed dramatically.

In a few instances, as the loads increased, longitudinal splitting cracks formed – typically between two closely spaced cracks where bond stresses would be expected to be considerably larger. Such behaviour could be mitigated by testing larger prism dimensions (i.e., having a smaller reinforcing ratio).

The results for average crack spacing (s_{avg}) and width (w_{avg}) are summarized in Table 6.1. Final crack spacing is a function of bond capacity: the greater the bond capacity, the more rapidly stress may be redistributed from the bar to the concrete between adjacent cracks, resulting in an additional crack forming and closer final crack spacing. As the specimens reinforced with steel bars are taken as control specimens, the crack spacing for steel reinforced concrete members is considered the reference. The experimental final crack spacing includes secondary cracks.

For two #4 steel bar specimens $s_{avg} \approx 160$ mm. The #4 rGFRP bars exhibited a 'softer' bond stress-slip relationship (Figure 5.5 curve g) resulting in a larger crack spacing: $s_{avg} \approx 180$ mm. On the other hand, the #4 sGFRP bars exhibited a 'stiffer' bond response (Figure 5.5 curve i) and the resulting crack spacing is smaller, $s_{avg} \approx 110$ mm. For #6 steel bars, $s_{avg} \approx 210$ mm, while for #6 rGFRP bars the final crack spacing was $s_{avg} \approx 250$ mm.

The average crack width was computed by Equation [2.9]. Since GFRP bars have lower modulus than steel, they are expected to exhibit larger crack widths, unless bond characteristics are improved proportionally. Prisms reinforced with GFRP bars presented larger crack widths – approximately three-four times greater than that of prisms reinforced with steel bars – reflecting the modular ratio of the materials (Section 4.2). The members reinforced with #4 sGFRP bars exhibited a larger number of cracks having a smaller width compared to other GFRP bars tested and presented the greater bond stress: 10.6 MPa; this is reflected in their apparent superior bond performance resulting in $k_b = 0.66$ for these bars from the prism test.

Several previous studies concluded that sand-coated GFRP bars exhibit better bond behaviour among the surface types of GFRP bars (e.g., El-Nemr et al., 2016; Shang, 2019). The pull-out tests performed for #4 sGFRP bars did not capture such improved behaviour (Table 5.2).

6.3.1 Comparison of test methods

As mentioned in Section 5.1, the ASTM D7913 pull-out test is an A-B comparison test rather than a test to establish a design parameter. The short bonded length of the bar ($5d_b$) overestimates the average bond stress that may be developed *in situ* and is used in design. On the other hand, the prism tension provides values of bond closer to those of a reinforced concrete flexural member (see Section 2.1.4.4).

For the ribbed GFRP bars, k_b determined from pull-out tests for #4 rGFRP bar is 1.31, while from prism tension tests k_b is 1.14 for the same bar. For #6 rGFRP bar k_b is 1.43 (pull-out test) and 1.17 (prism tension test). As expected, the values of k_b predicted from pull-out tests were higher than those estimated from prism tests – except for #4 sGFRP (Table 6.2). The single data point for sand-coated bars showing the opposite trend is problematic. The k_b values provided from pull-out test are conservative – they were about 15 to 20% greater than that determined from the prism test. However, k_b values reported from both tests are similar and follow the same trends. This indicates that the prism tension test may be suitable to provide confident values of k_b as previously reported by Silva et al. (2021).

In a pilot study (Silva et al., 2021), the same #5 sand-coated bars as presented in this study tested in $100d_b$ long prisms having 127 mm square sections (ρ = 0.012) resulted in k_b = 0.68. In pull-out tests, the bond strength was observed to 11.9 MPa (Silva et al., 2021), whereas it was 10.8 MPa in this study. In the earlier study, the concrete strength was only 28.3 MPa, resulting in relatively lower bond strength for comparable steel bars (11.4 MPa) and a k_b = 0.96.

These results highlight the sensitivity of the pull-out test and therefore k_b when calculated from such a test. In this study, the rib ratios of the steel bars are relatively large (Table 4.2), indicating that good bond performance should be expected. This has the effect of decreasing the calculated k_b ratio.

Analysing k_b values estimated from both pull-out and prism tension test (Table 6.2), it is possible to conclude that for bars having same surface configuration (#2 hGFRP and #3 hGFRP, and #4 rGFRP and #6 rGFRP), larger k_b was obtained for larger diameters.

Table 6.2 – Bond-dependent coefficient (k_b) calculated ASTM D7913 from pull-out and prism tension tests.

Bar nomenclature	Calculated k_b Equation [5.1]	
	ASTM D7913 pull-out test	Prism test
#2 hGFRP	0.62	-
#3 hGFRP	1.25	-
#4 rGFRP	1.31	1.14
#6 rGFRP	1.43	1.17
#4 sGFRP	2.24	0.66

6.4 Summary of the chapter

In this chapter, a description of the 12 prism tension tests performed in this study was presented. The discussion of test results and their relationship to those of pull-out tests (reported in Chapter 5) were also presented.

Using the long prism tension test, crack spacing (s_{avg}) and width (w_{avg}) of embedded bars in tension can be investigated. The main conclusions are as follows:

— for deformed bars, crack spacing and crack width are inversely proportional to bar stiffness. Prisms reinforced with GFRP bars presented larger crack widths – approximately three-four times greater than that of prisms reinforced with steel bars – reflecting the modular ratio of the materials;

— sand-coated bars exhibited a larger number of cracks having smaller widths in comparison to other GFRP bars tested; this resulted in k_b = 0.66 for these bars from the prism test;

— for the deformed GFRP bars, k_b determined from the pull-out test is 15% to 20% greater than that determined from the prism test. The single data point for sand-coated bars showing the opposite trend is problematic, although the author is confident that the prism tests leading to k_b = 0.66 are representative;

— for the same surface configuration, the greatest k_b values were found for larger diameters of GFRP for both pull-out and prism tests.

7

SAND ADHESION TEST

In this chapter, an experimental test to investigate the adhesion of the sand coating to the sand-coated GFRP reinforcing bars tested in this study and thereby determine whether this may affect the bond performance of such bars is presented. The apparently contradictory results of the ASTM D7913 pull-out tests and prism tension tests for the #4sGFRP bars, that is, the average bond stress from the pull-out test being lower than that obtained from the prism test, led to one hypothesis explanation: a failure mode not considered, i.e., the loss of adhesion of the sand coating from the bar during pull out. This chapter documents an ad hoc test programme intended to test this hypothesis. The experimental set-up and testing procedure are described. The results led to the conclusion that the bond of the sand coating is superior to any bond capacity expected of the bar, although not by as great a margin as one may expect.

7.1 Introduction

GFRP reinforcing bars are manufactured with a variety surface deformation – indentations (machined ribs), sand coating, and helical wrapping, among others – in order to provide mechanical bond to the concrete in which the bars are embedded. Most of these surface treatments differ significantly from the surface deformations of conventional steel reinforcing bars.

Considering the GFRP bar geometry itself, surface deformations of GFRP bars usually present lower shear strength than the rolled-in surface ribs or lugs of steel bars. The shear capacity at the concrete-resin (i.e., concrete-GFRP bar) and resin-fiber interfaces (i.e., internal to the bar) in a bond failure are influenced by the deformation geometry of the GFRP bars (Al-Zahrani et al. 1999; Al-Mahmoud et al. 2007). In some older GFRP bars – especially those having post-applied wrapped deformations, the deformations have been observed to shear off (e.g., Moon et al. 2008). Similar to a GFRP lug, the sand coating on a sand-coated bar can be ‘sheared off’

the bar. The sand is typically broadcast onto the bar as it is pultruded and is therefore ‘embedded’ into the vinyl ester resin matrix prior to cure. There is no standard method to quantify the resulting shear capacity (adhesion) of the sand and underlying bar.

A simple test method and apparatus is demonstrated that can be used to assess adhesion of sand coating to FRP bars. Sand adhesion test results are compared with ASTM D7913 pull-off tests.

7.2 Test details

7.2.1 Test specimens and procedure

Five short lengths of each #4 and #5 bars sand-coated GFRP bars were tested (Figure 7.1a). The bars are cut longer than 50 mm. Measured bar properties are given in Table 4.2. Two 50 mm long hollow steel cylinders were fabricated (Figures 7.1b and c). The inside diameter, *d*, is about 4 mm larger than the measured diameter of the finished bar to be tested (d_b = 13.2 and 17.5 mm for #4 sGFRP and #5 sGFRP, respectively). A collar having a reduced inside diameter (aperture) *D* = 11.9 mm and 16.8 mm for the #4 sGFRP and #5 sGFRP bars, respectively, corresponding to the diameter of the bar without sand, is provided at midheight of the cylinder. The length of the collar is *L* = 3.2 and 4.5 mm for #4 sGFRP and #5 sGFRP bars, respectively, approximately one quarter the bar diameter. The upper 25 mm of the cylinder has a centering apparatus, allowing the bar to be installed without eccentricity relative to the collar (Figure 7.1). It should be noted that the test apparatus must be custom made for each bar type used since outer dimensions of sand-coated bars can vary substantially.

Bars were placed vertically in the steel cylinder and the assembly was positioned in a servo hydraulic testing machine with load capacity of 600 kN (Figure 7.1d). The bar was pushed into the cylinder at a rate of 1 mm/s. The bar is forced through the collar aperture which ‘shears off’ the sand coating. Displacement and load were recorded from the tests. At 25 mm displacement, the bar has been fully pushed through the cylinder assembly and its end begins to bear on the test machine: the load increases signifying the end of the test.

Figure 7.1 – Test specimens and apparatus.

a) #4 sGFRP and #5 sGFRP bars tested

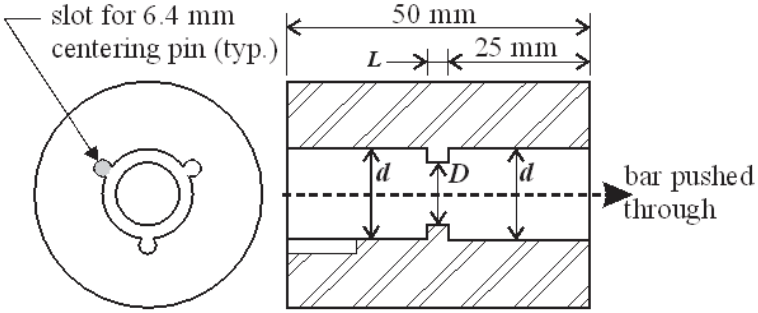

Bar	Measured d_b (mm)	d (mm)	D (mm)	L (mm)
#4 sGFRP	13.2	16.7	11.9	3.2
#5 sGFRP	17.5	21.5	16.8	4.5

b) Isometric drawing of test apparatus

c) Top and bottom of #4 test apparatus

d) #5 bar being tested – bar is pushed into steel cylinder, shearing off sand coating

Source: author.

The test is affected by friction and the accumulation of the removed sand surface around the aperture. The force required to shear the sand from the perimeter of the bars, p_{sand}, is given in terms of the force exerted in a circumferential ring 1 mm tall. p_{sand} and is determined at a displacement L, corresponding to the bar first entirely engaging the aperture collar:

$$p_{sand} = \frac{P_b}{L} \tag{7.1}$$

where P_b is the applied load at displacement L, and L is the length of the aperture (Figure 7.1b).

A comparison is made with the ASTM D7913 test results. The bond stress determined in the ASTM D7913 test is assumed to be acting uniformly over the $5d_b$ embedment length (Figure 2.7). From Equation [2.6], the force acting on a portion of the bar perimeter, p_{D7913}, can be estimated as:

$$p_{D7913} = \frac{P_{max}}{5d_b} \tag{7.2}$$

Combining Equations [2.6] and [7.2]:

$$p_{D7913} = \tau_{max}\pi d_b \tag{7.3}$$

where $\tau_{max} = P_{max}/5\pi d_b^2$ is the shear stress from the ASTM D7913 test ($5d_b$ is the length of bar embedment and πd_b is the bar circumference).

In Equation [7.3], by convention, d_b is based on the nominal bar diameter, 12.7 mm and 15.9 mm for #4 sGFRP and #5 sGFRP bars, respectively.

7.2.2 Sand adhesion test results and discussion

Five samples of each of the #4 sGFRP and #5 sGFRP bars were tested to determine the force required to shear the sand from bar surface. The results are presented in terms of displacement versus applied load in Figure 7.2 and individual results are summarized in Table 7.1.

Figure 7.2 – Applied load versus displacement results for sand adhesion tests.

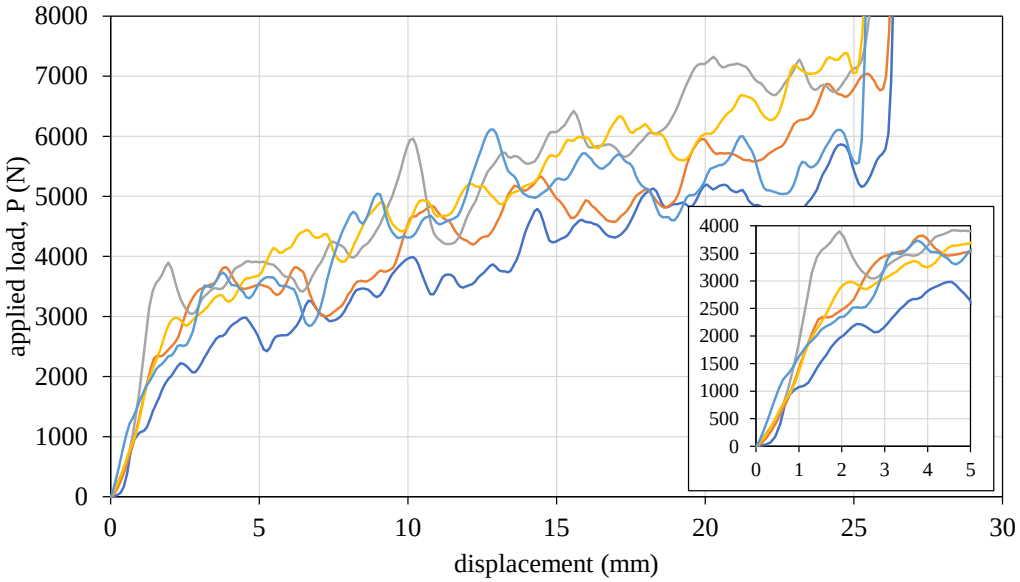

(a) #4 sGFRP bars.

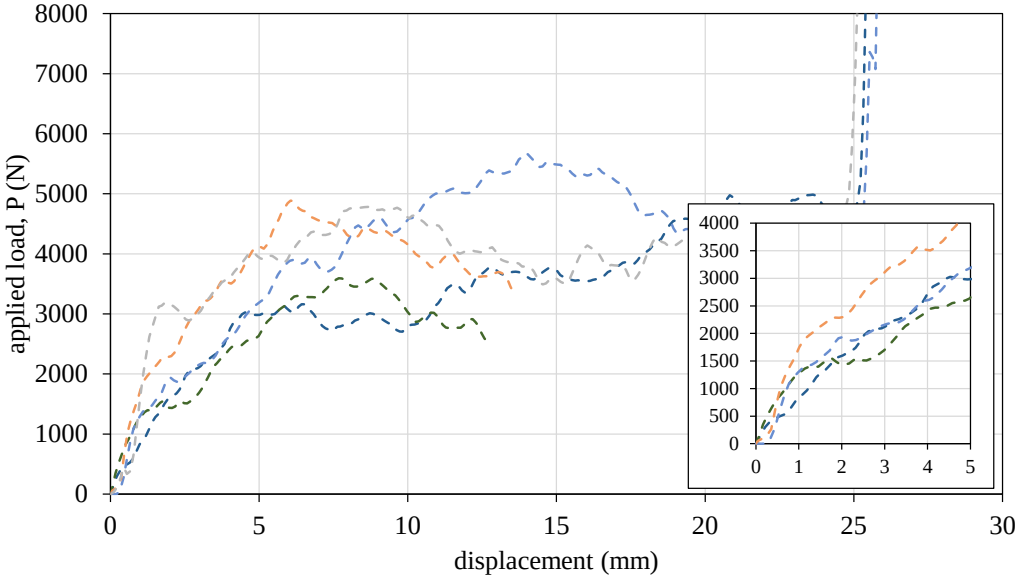

(b) #5 sGFRP bars.
Source: author.

Table 7.1 – Results from sand adhesion tests.

Bar	d_b (mm)	L (mm)	Specimen	P_b (N)	p_{sand} (N/mm) Equation [7.1]	τ_{max} from pull-out test (MPa)	p_{D7913} (N/mm) Equation [7.3]
#4 sGFRP	13.2	3.2	1	2313	723		
			2	3491	1091		
			3	3341	1044		
			4	3125	977		
			5	3512	1098		
				Average	986	7.33	292
				COV	0.157	0.39	-
#5 sGFRP	17.5	4.5	1	2995	666		
			2	2470	549		
			3	2888	642		
			4	3678	817		
			5	3863	858		
				Average	706	10.78	538
				COV	0.182	0.16	-

It is seen in Figure 7.2 that the applied force varies considerably during the test although does not fall below the force at which the entire aperture is engaged at displacement L. The variation and continued gradual increase in load are associated with friction and the accumulation of removed sand in the upper chamber of the test apparatus.

For both bar types tested, the force required to shear the sand from the bar exceeded the pull-out strength determined in the ASTM D7913 tests. Thus, it is possible to conclude that sand adhesion was unlikely to be a factor contributing to the low bond stress results observed for these bars in the ASTM D7913 tests (see Chapter 5).

However, the results for the #5 sGFRP bars indicate some likelihood that sand adhesion may affect pull-out results. Considering the variation inherent in both tests (assuming a Gaussian distribution of results) and the small sample size (n = 5), the probability that $p_{D7913} > p_{sand}$ – the condition in which sand adhesion affects the ASTM D7913 pull-out test – is 14% for the #5 sGFRP bars tested. The same probability of sand adhesion failure for the #4 sGFRP bars is negligible.

The motivation for this study was poor observed bond strength results for sand-coated GFRP bars (Table 5.2). Had either of these bars achieved parity (i.e., k_b = 1) with the #4 steel bars tested (τ_{max} =16.45 MPa), the value of p_{D7913} increases to 656 N/mm and 822 N/mm for the #4

and #5 steel bars, respectively. This would indicate a possible sand adhesion failure for at least the #5 bars tested.

7.3 Summary of the chapter

It was confirmed that, for the sand-coated GFRP bars considered, the adhesion of the sand coating to the bar was superior to the bond capacity of the bar, although not by as great a margin as one may expect. While sand-coated bars are usually observed to behave better than comparable deformed bars, the preliminary results presented here suggest that sand adhesion to the bars could control bond strength in some cases. Ultimately, however, the reason for the apparently low bond stress results for the bars tested is not deemed to be adhesion failure of the sand in this instance.

A simple test method and apparatus is demonstrated that can be used to assess adhesion of sand coating to FRP bars and may be adapted to consider the shear capacity of lugs on other types of FRP bars.

8

FINAL REMARKS

8.1 Conclusions

In situations where reinforced concrete structures are in aggressive environments, the corrosion of steel reinforcement is considered the major problem related to durability and is a factor that can significantly reduce service life. In this sense, Glass Fiber-Reinforced Polymers (GFRP) reinforcing bars, as materials more resistant to corrosion, have emerged as an alternative to steel as internal reinforcement in concrete structures.

Although GFRP shows a promising prospect for use as reinforcement, the mechanical properties of the bars – low modulus of elasticity and high tensile strength – lead to changes in the design paradigm for GFRP-reinforced concrete (GFRP-RC) structures. While steel RC structures are typically designed based on the strength limit state and then checked for serviceability requirements, the design of GFRP-RC members is often governed by deflection and crack control at the serviceability limit state.

Equations for bond and cracking control of GFRP-RC members are generally based on similar formulations as used for conventional steel RC elements with the addition of a bond-dependent coefficient, k_b, to account for bond performance different from that of steel. While bond behaviour between conventional steel and concrete is relatively well-known and documented, the same is not true for GFRP bars.

The first part of this study presented a parametric investigation based on data available in published literature in order to analyze the influence of different parameters in the estimation of k_b at the serviceability level crack width limit of 0.70 mm, although other values of crack width limit were also considered in the analysis. It was clear that k_b is sensitive to the concrete crack width at which it is calculated. Most of GFRP bars tested by the investigators presented

bond behaviour superior to that of steel (k_b less than 1.0), although k_b was found to be relatively insensitive to the surface treatment of the bar: whether deformed (ribbed) or sand-coated. On the other hand, k_b was found to be strongly correlated with the GFRP reinforcing bar stress, $f_{f,}$ at which k_b is determined. Correlations with other factors including concrete strength, cover concrete (greater than 12 mm) and GFRP bar diameter (less than 25 mm) were weak, reinforcing that the k_b factor is a bond coefficient dependent on the reinforcing bar, not its embedment. Considering values of k_b reported by the original authors using both Gergely-Lutz and Frosch equations, the paired t-test and the Wilcoxon signed-rank test confirmed that there is statistical difference on k_b estimated by both equations, indicating the more conservative nature of Gergely-Lutz equation (lower mean k_b). In the absence of bar-specific testing, the value of k_b equal to 1.2 recommend by ACI 440.11-22 could be considered appropriately conservative and reflects the still relatively small amount of available data.

The experimental part of this thesis proposed two relatively simple tests – the ASTM D7913 pull-out and prism tension tests – to assess the bond performance and cracking behaviour of GFRP bars, respectively. The study presented the evaluation of k_b using ASTM D7913 and confirming bond performance using a smaller number of prism tension tests. Data from the seven GFRP bar types considered in this study were used to supplement and extend an earlier database of 36 GFRP bar types reported by Sólyom and Balázs (2020).

Pull-out test results from this investigation indicated superior bond behaviour (k_b less than 1.0) for most of GFRP bars tested in normal-strength concrete, although the greater bond stresses were attained by specimens fabricated with high strength concrete, independent of the bar configuration. Furthermore, k_b was higher for the larger diameter of bars with same surface configuration. Considering all the GFRP bars tested, the higher bond stresses were found for helically wrapped (diameter of 6.3 and 9.5 mm) and ribbed GFRP (diameter of 12.7 and 19.1 mm), while the 12.7 mm diameter sand-coated GFRP exhibited the lowest value.

Based on the limited number of prism tension tests conducted, prisms reinforced with GFRP bars presented crack widths that were approximately three-four times greater than that of prisms reinforced with steel bars. A comparison of results for prism tests with those of ASTM D7913 pull-out tests was proposed, allowing the latter to be better calibrated for providing appropriate

design values for k_b and bond strength of GFRP bars. It could be concluded that k_b predicted by pull-out test were about 15-20% greater than those estimated by prism tension test for the same bar type and k_b estimated by both pull-out and prism tests were larger for the larger bar diameters (same surface configuration). The greater bond stresses were attained by the 12.7 mm diameter sand-coated GFRP bars.

Based on this assessment, this study can conclude that ASTM D7913 pull-out tests can be used to determine conservative values for k_b and to benchmark bond strength of GFRP bars, although this test must be used with caution when assessing relative bond parameters.

Comparing the results of pull-out and prism tests, apparently contradictory results for the bond capacity of the 12.7 mm diameter sand-coated GFRP bars emerged: the average bond stress from the pull-out test was lower than that obtained from the prism test. This led to one hypothesis that is a failure mode involving shearing the sand coating from the bars. A bespoke experimental study intended to assess the adhesion of the sand coating to the GFRP bar and thereby determine whether this may affect the bond performance of the bar was performed. The results confirmed that, for the bars considered, the adhesion of the sand coating to the bar was superior to the bond capacity of the bar – although not by as great a margin as one may expect – and that sand coating failure is unlikely.

8.2 Recommendations for future works

This research focused on the assessment of bond and cracking performances and k_b of GFRP bars. Suggestions for future investigations may include:

— conduct an experimental program using beam prism test – and pull-out tests – with a large sample size to confirm the hypothesis that prism tests are an adequate simple test for estimating k_b;

— perform prism tension test investigating parameters – such as bar diameter, surface configuration, service stress, and concrete strength – independently in order to verify their influence on cracking behaviour;

— propose a numerical model to describe bond-slip behaviour for different types of GFRP bars;

— analyze the effect of reinforcement strain on bond performance in prism tension test by adding strain gauges on the bar.

REFERENCES

ABDELKARIM, O. I., AHMED, E. A., MOHAMED, H. M., and BENMOKRANE, B. (2019). Flexural strength and serviceability evaluation of concrete beams reinforced with deformed GFRP bars. **Engineering Structures**, 186(May 2018), 282–296.

ABDULHAMEED, A. A., AL-ZUHAIRI, A. H., AL ZAIDEE, S. R., HANOON, A. N., AL ZAND, A. W., HASON, M. M., and ABDULHAMEED, H. A. (2022). The Behavior of Hybrid Fiber-Reinforced Concrete Elements: A New Stress-Strain Model Using an Evolutionary Approach. **Appl. Sci**. 2022, 12, 2245.

ACI COMMITTEE 318. (1999). **Building Code Requirements for Structural Concrete (ACI 318-1999) and Commentary (ACI 318R-99)**, American Concrete Institute, Farmington Hills, Michigan, USA.

ACI COMMITTEE 318. (2014). **Building Code Requirements for Structural Concrete (ACI 318-2014) and Commentary (ACI 318R-14)**, American Concrete Institute, Farmington Hills, Michigan, USA.

ACI COMMITTEE 318. (2019). **Building Code Requirements for Structural Concrete (ACI 318-2019) and Commentary (ACI 318R-19)**, American Concrete Institute, Farmington Hills, Michigan, USA.

ACI COMMITTEE 408. (2012). **Bond and Development of Straight Reinforcing Bars in Tension (ACI PRC 408.3R-12)**, American Concrete Institute, Farmington Hills, Michigan, USA.

ACI COMMITTEE 440. (2001). **Guide for the Design and Construction of Concrete Reinforced with FRP Bars (ACI PRC 440.1.1R-01)**, American Concrete Institute, Farmington Hills, Mich., 41 pp.

ACI COMMITTEE 440. (2006). **Guide for the Design and Construction of Structural Concrete Reinforced with FRP Bars (ACI PRC 440.1.1R-06)**, American Concrete Institute, Farmington Hills, Michigan, USA.

ACI COMMITTEE 440. (2007). **Report on Fiber-Reinforced Polymer (FRP) Reinforcement for Concrete Structures (ACI PRC 440R-07)**, American Concrete Institute, Farmington Hills, Michigan, USA.

ACI COMMITTEE 440. (2015). **Guide for the Design and Construction of Structural Concrete Reinforced with FRP Bars (ACI PRC 440.1.1R-15)**, American Concrete Institute, Farmington Hills, MI, 88 pp.7.

ACI COMMITTEE 440. (2022). **Building Code Requirements for Structural Concrete Reinforced with Glass Fiber Reinforced Polymer (GFRP) Bars**, American Concrete Institute, Farmington Hills MI, forthcoming.

AHMED, E., MOHAMED, H. M., EL-NEMR, A., VINCENT, P., and BENMOKRANE, B. (2013). Bond-dependent coefficient of deformed glass fiber-reinforced polymer (GFRP) reinforcing bars. **Proceedings**, Annual Conference - Canadian Society for Civil Engineering, 5(January), 3854–3861.

AL-DULAIJAN, S. U., NANNI, A., AL-ZAHRANI, M. M., and BAKIS, C. E. (1996). Bond Evaluation of Environmentally Conditioned GFRP/ Concrete System. **Proceedings** of the Second International Conference on Advanced Composite Materials in Bridges and Structures (ACMBS-2), M. M. El-Badry, ed., Canadian Society for Civil Engineering, Montreal, QC, Canada, pp. 845-852.

AL-MAHMOUD, F., CASTEL, A., FRANCOIS, R., TOURNEUR, C. (2007). Effect of surface pre-conditioning on bond of carbon fibre reinforced polymer rods to concrete. **Cement and Concrete Composites**; 29(9):677–689.

AL-ZAHRANI, M.M., AL-DULAIJAN, S.U., NANNI, A., BAKIS, C.E., BOOTHBY, T.E. (1999). Evaluation of bond using FRP rods with axisymmetric deformations. **Construction and Building Materials**;13(6):299–309.

ASTM A615-22. (2022). **Standard Specification for Deformed and Plain Carbon-Steel Bars for Concrete Reinforcement**, ASTM International, West Conshohocken PA, USA.

ASTM C39-21. (2021). **Standard Test Method for Compressive Strength of Cylindrical Concrete Specimens**, ASTM International, West Conshohocken PA, USA.

ASTM C496-17. (2017). **Standard Test Method for Splitting Tensile Strength of Cylindrical Concrete Specimens**, ASTM International, West Conshohocken PA, USA.

ASTM D7205-21. (2021). **Standard Test Method for Tensile Properties of Fiber Reinforced Polymer Matrix Composite Bars**, ASTM International, West Conshohocken PA, USA.

ASTM D7617-17. (2017). **Standard Test Method for Transverse Shear Strength of Fiber-reinforced Polymer Matrix Composite Bars**, ASTM International, West Conshohocken PA, USA.

ASTM D7913-14. (2020). **Standard Test Method for Bond Strength of Fiber-Reinforced Polymer Matrix Composite Bars to Concrete by Pullout Testing**, ASTM International, West Conshohocken PA, USA.

ASTM D7957-22. (2022). **Standard Specification for Solid Round Glass Fiber Reinforced Polymer Bars for Concrete Reinforcement**, ASTM International, West Conshohocken PA, USA.

ASTM D8505-23. (202). **Standard Specification for Basalt and Glass Fiber Reinforced Polymer (FRP) Bars for Concrete Reinforcement**, ASTM International, West Conshohocken PA, USA.

BAENA, M., TORRES, L., TURON, A., and BARRIS, C. (2009). Experimental study of bond behaviour between concrete and FRP bars using a pull-out test. **Composites Part B: Engineering**, 40(8), 784–797.

BAKIS, C. E., FREIMANIS, A. J., GREMEL, D., and NANNI, A. (1998). Effect of Resin Material on Bond and Tensile Properties of Unconditioned and Conditioned FRP Reinforcement Rods. **Proceedings** of the First International Conference on Durability of Composites for Construction, B. Benmokrane and H. Rahman, eds., Sherbrooke, QC, Canada, pp. 525-535.7

BAKIS, C. E., OSPINA, C. E., BRADBERRY, T. E., BENMOKRANE, B., GROSS, S. P., NEWHOOK, J. P., and THIAGARAJAN, G. (2006). Evaluation of crack widths in concrete flexural members reinforced with FRP bars. **Composites in Civil Engineering**, CICE 2006, 03(Cice), 307–310.

BANK, L. C., PUTERMAN, M., and KATZ, A. (1998). The Effect of Material Degradation on Bond Properties of FRP Reinforcing Bars in Concrete. **ACI Materials Journal**, V. 95, No. 3, May-June, pp. 232-243.

BARRIS, C., TORRES, L., COMAS, J., and MIÀS, C. (2013). Cracking and deflections in GFRP RC beams: An experimental study. **Composites Part B: Engineering**, 55, 580–590.

BARRIS, C., TORRES, L., VILANOVA, I., MIÀS, C., and LLORENS, M. (2016). Experimental study on crack width and crack spacing for Glass-FRP reinforced concrete beams. **Engineering Structures**, 131, 231–242.

BISCHOFF, P.H., GROSS, S., and OSPINA, C.E. (2009). The Story behind Proposed Changes to the ACI PRC 440.1 Deflection Requirements for FRP-Reinforced Concrete. ACI SP-264, **American Concrete Institute**, eds. Ospina, C., Bischoff, P., and Alkhrdaji, T., MI, pp. 53-76.

CANADIAN STANDARDS ASSOCIATION. (2006). **Canadian Highway Bridge Design Code (CAN/ CSA-S6-06.)**. Toronto, Ontario, Canada.

CANADIAN STANDARDS ASSOCIATION. (2012). **Design and Construction of Building Components with Fibre-Reinforced Polymers** (CAN/CSA-S806-12). Ontario, Canada.

CARRASQUILLO, R. L., NILSON, A. H., and SLATE, F. O. (1981). Properties of High Strength Concrete Subject to Short-Term Loads. **ACI Journal**, Vol. 78, No. 3, May-June, pp. 171 – 178.

CEB, 1990, "**CEB/FIP Model Code 1990**," Comité European de Béton, Thomas Telford, 437 pp.

CLARK, A. P. (1946). Comparative bond efficiency of deformed concrete reinforcing bars. **ACI Journal**, 43(4), 381-400.

CLARK, A. P. (1949). Bond of Concrete to Reinforcing Bars. **ACI Journal Proceedings** 46(11), 161-184.

CHAALLAL, O., and BENMOKRANE, B. (1993). Pullout and Bond of Glass-Fiber Rods Embedded in Concrete and Cement Grout. **Materials and Structures**;26(3):167– 175.

CHOI, O. C., HADJE-GHAFFARI, H., DARWIN, D., and MCCABE, S. L. (1990). **Bond of epoxy-coated reinforcement to concrete: bar parameters**. University of Kansas Center for Research, Inc.

COLLINS, M. P., and MITCHELL, D. (1997). Prestressed concrete structures. Toronto: **Response Publications**.

COSENZA, E., MANFREDI, G., and REALFONZO, R. (1997). Behavior and modeling of bond of FRP Rebars to concrete, **J. Compos. Constr.** 40–51. (ASCE)1090-0268(1997)1:2(40).

EL-NEMR, A, AHMED, E. A., and BENMOKRANE, B. (2013). Flexural behavior and serviceability of normal- And high-strength concrete beams reinforced with glass fiber-reinforced polymer bars. **ACI Structural Journal**, 110(6), 1077–1087.

EL-NEMR, A., AHMED, E. A., BARRIS, C., and BENMOKRANE, B. (2016). Bond-dependent coefficient of glass- and carbon-FRP bars in normal- and high-strength concretes. **Construction and Building Materials**, Vol. 113, pp 77-89.

EL-SALAKAWY, E., and BENMOKRANE, B. (2004). Serviceability of concrete bridge deck slabs reinforced with fiber-reinforced polymer composite bars. **ACI Structural Journal**, 101(5), 727–736.

FARSHADFAR, O., AJAAM, A., HANO, M., O'REILLY, M., and DARWIN, D. (2014). **Bond Strength of Reinforcing Bars with Deformation Spacings that Exceed Maximum Specified in ASTM A615**. The University of Kansas Center for Research, Inc.

FAZA, S. S., and GANGARAO, H. V. S. (1993). Glass FRP Reinforcing Bars for Concrete, Fiber-Reinforced-Plastic (FRP) Reinforcement for Concrete Structures: Properties and Applications, **Developments in Civil Engineering**, V. 42, A. Nanni, ed., Elsevier, Amsterdam, pp. 167-188.

FELDMAN, L. R., and BARTLETT, F. M. (2005). Bond strength variability in pullout specimens with plain reinforcement, **ACI Structural Journal**, 102(6), 860.

FIB. (2013). **Model Code for Concrete Structures 2010**. Ernst & Sohn.

FREIMANIS, A. J., BAKIS, C. E., NANNI, A., and GREMEL, D. (1998). A Comparison of Pullout and Tensile Behaviors of FRP Reinforcement for Concrete. **Proceedings** of the Second International Conference on Composites in Infrastructure (ICCI-98), V. 2, Tucson, AZ, pp. 52-65.

FROSCH, R.J. (1999). Another Look at Cracking and Crack Control in Reinforced Concrete", **ACI Structural Journal**, 96(3), 437-442.

GAO, D., BENMOKRANE, B., and MASMOUDI, R. (1998). A calculating method of flexural properties of FRP-Reinforced concrete beam: Part:1 Crack width and deflection. **Technical Report**, Department of Civil Engineering, University of Sherbrook, February, 22pp.

GERGELY, P. and LUTZ, L. A. (1968). Maximum Crack Width in Reinforced Concrete Flexural Members, ACI SP20: Causes, Mechanism, and Control of Cracking in Concrete. **American Concrete Institute**, pp 87-117.

HAO, Q., WANG, Y., HE, Z., and OU, J. (2009). Bond strength of glass fiber reinforced polymer ribbed rebars in normal strength concrete. **Constr. Build. Mater.** 23 865-871.

ISIS MANUAL NO. 3. (2007). **Reinforced Concrete Structures with Fibre-Reinforced Polymers**. ISIS Canada Research Network, University of Manitoba, Winnipeg, MB, 151 p.

JAPAN SOCIETY OF CIVIL ENGINEERING (JSCE). (1997). **Recommendation for Design and Construction of Concrete Structures using Continuous Fiber Reinforcing Materials**. Concrete Engineering Series, No. 23, Tokyo, Japan.

KASSEM, C. (2004). **Cracking and load-deflection behaviour of one-way concrete elements reinforced with FRP bars under flexure**. Ph.D. Thesis (in French), Dept. of Civil Engineering, Université de Sherbrooke, Sherbrooke, Québec, Canada.

KASSEM, C., FARGHALY, A. S., and BENMOKRANE, B. (2011). Evaluation of Flexural Behavior and Serviceability Performance of Concrete Beams Reinforced with FRP Bars. **Journal of Composites for Construction**, 15(5), 682–695.

LA TEGOLA, A. (1998). Actions for Verification of RC Structures with FRP Bars. **Journal of Composites for Construction**, ASCE, V. 2, No. 3, pp. 145-148.

LEE, W. K., JANSEN, D. C., BERLIN, K. B., and COHEN, I. E. (2010). Flexural cracks in Fiber-reinforced concrete beams with Fiber-reinforced polymer reinforcing bars. **ACI Structural Journal**, 107(3), 321–329.

LORRAIN, M. S., CAETANO, L. F., VALE SILVA, B., GOMES, L. E. S., BARBOSA, M. P., and Silva FILHO, L. C. P. (2010). Bond strength and rib geometry: a comparative study of the influence of deformation patterns on anchorage bond strength. In PCI **Annual Convention** and 3rd International FIB Congress FIB, Washington, D C. Chicago: 3rd FIB International Congress FIB.

MACGREGOR, J. G. (1997). **Reinforced Concrete: Mechanics and Design**. Prentice Hall Upper Saddle River, NJ, 450 p.

MAEKAWA, K., PIMANMAS, A., and OKAMURA, H. (2003). **Nonlinear Mechanics of Reinforced Concrete**. Spon Press, London.

MASMOUDI, R., THÉRIAULT, M., and BENMOKRANE, B. (1998). Flexural behavior of concrete beams reinforced with deformed fiber reinforced plastic reinforcing rods. **ACI Struct. J.**, Vol. 95, No. 6, pp. 665-675.

MCCALLUM, B. E. C., and NEWHOOK, J.P. (2012). Evaluation of the Bond Dependent Coefficient and Parameters which Influence Crack Width in GFRP Reinforced Concrete. **Proceedings** of 6th International Conference on Advanced Composite Materials in Bridges and Structures. Kingston, Ontario, Canada.

MCCALLUM, B. (2013). **Experimental Evaluation of the Bond Dependent Coefficient and Parameters which influeence Crack Width in GFRP Reinforced Concrete**. M.S. Thesis, Dalhousie University Halifax, Nova Scotia.

MOON, D.Y., SIM, J., OH, H.S. and BENMOKRANE, B. (2008). An exploratory study of GFRP rebar with ribs containing milled glass fibers, **Composites Part B: Engineering** 39(5), 882-890.

MORCOUS, G., and HENIN, E. (2018). Bond-dependent coefficient of helically wrapped sand-coatedglass fiber-reinforced polymer (GFRP) bars. **Advances in Civil Engineering Materials**, 7(1), 353–366.

MOTA, C.; ALMINAR, S.; and SVECOVA, D. (2006) Critical Review of Deflection Formulas for FRP-RC Members. **Journal of Composites for Construction**, ASCE, V. 10, No. 3, pp. 183-194.

NANNI, A. (1993). Flexural Behavior and Design of Reinforced Concrete Using FRP Rods. **Journal of Structural Engineering**, ASCE, V. 119, No. 11, pp. 3344-3359.

NANNI, A. (2003). North American design guidelines for concrete reinforcement and strengthening using FRP: Principles, applications and unresolved issues. **Construction and Building Materials**, 17(6-7), 439-446.

NANNI, A., NENNINGER, J., ASH, K., and LIU, J. (1997). Experimental Bond Behavior of Hybrid Rods for Concrete Reinforcement. **Structural Engineering and Mechanics**, V. 5, No. 4, pp. 339-353.

NANNI, A., AL-ZAHRANI, M.M., AL-DULAIJAN, S.U., BAKIS, C.E., BOOTHBY, T.E. (2005). Bond of FRP reinforcement to concrete - experimental results. In: Taerwe, L., editor. Second International **Symposium** on Non-Metallic (FRP) Reinforcement for Concrete Structures, p. 135–145.

NEWHOOK, J.P. (2000). The use of fibre reinfroced concrete to reduce crack widths in GFRP reinforced concrete beams. **Proc.** 3rd Intl. Conf. Advanced Composite Materials in Bridges and Structures, ACMBS III, Editors: J. L.

NOËL, M., and SOUDKI, K. (2013). Estimation of the crack width and deformation of FRP-reinforced concrete flexural members with and without transverse shear reinforcement. **Engineering Structures**, 59, 393–398.

OSOFERO, A. I., CORRADI, M., and BORRI, A. (2014). Experimental Study of Bond Strength between Titanium Bar and Lime-Based Mortar. **Journal of Materials in Civil Engineering**, 04014182.

OSPINA, C. E., and BAKIS, C. E. (2007). Indirect flexural crack control of concrete beams and one-way slabs reinforced with FRP bars. **Proceedings** of the 8th International Symposium on Fibre-Reinforced Polymer Reinforcement for Concrete Structures, 1, 1–9.

PARK, R., and PAULAY, T. (1975). **Reinforced concrete structures**. John Wiley and Sons, 769pp.

PEZESHK, S. (2008). **Reinforced Concrete Design Notes**, CIVIL 4135, The University of Memphis.

PLATT, S. (2018). **Development of Titanium Reinforcing Bars for Concrete and Masonry**, Doctoral dissertation, University of Pittsburgh.

PLATT, S., and HARRIES, K. A. (2018). Geometry, material properties and bond performance of prototype titanium reinforcing bars. **Construction and Building Materials**, 187, 1253–1266.

RAFI, M.M, NADJAI, A., and ALI, F. (2007). Analytical Modeling of Concrete Beams Reinforced with Carbon FRP Bars. **Journal of Composite Materials**. 41(22):2675-2690.

REIS, E. E., MOZER, J. D., BIANCHINI, A. C. and KESLER, C. E. (1964). **Causes and control of cracking in concrete reinforced with high strength steel Bars – A review of research**, T. and A. M. Report No. 261, University of Illinois, IL.

RIBEIRO, S.E.C., and DINIZ, S.M.C. (2013). Reliability- Based Design Recommendations for FRP-Reinforced Concrete Beams. **Engineering Structures**, V. 52, pp. 273–283.

SALIB, S. R., and ABDEL-SAYED, G. (2004). Prediction of crack width for fiber-reinforced polymer-reinforced concrete beams. **ACI Structural Journal**, 101(4), 532-536.

SHANG, C. (2019). **Evaluation of the Bond-Dependent Coefficient for GFRP Bars in Concrete Beams**. M.S. Thesis, Dept. of Civil Engineering, University of Manitoba, Winnipeg, MB, Canada.

SHIELD, C., BROWN, V., BAKIS, C. E., and S. GROSS. (2019). A Recalibration of the Crack Width Bond-Dependent Coefficient for GFRP-Reinforced Concrete. **J. Compos. Constr**., vol. 23, no. 4, p. 04019020.

SILVA, E., HARRIES, K., LUDVIG, P., PLATT, S. (2021). Toward a Practical Approach to Experimental Evaluation of Cracking Behaviour of GFRP-Reinforced Concrete. In A. Ilki, M. Ispir, & P. Inci (Eds.), 10th International Conference on FRP Composites in Civil Engineering - **Proceedings** of CICE 2020/2021 (pp. 866-877). (Lecture Notes in Civil Engineering; Vol. 198 LNCE). Springer Science and Business Media Deutschland GmbH.

SILVA, E., HARRIES, K., LUDVIG, P., PLATT, S. (2022). Toward a Practical Approach to Experimental Evaluation of Cracking Behaviour of GFRP-Reinforced Concrete. In: Ilki, A., Ispir, M., Inci, P. (eds) 10th International Conference on FRP Composites in Civil Engineering. CICE 2021. **Lecture Notes in Civil Engineering**, vol 198. Springer, Cham.

SOLTANI, A., HARRIES, K. A., and SHAHROOZ, B. M. (2013). Crack Opening Behavior of Concrete Reinforced with High Strength Reinforcing Steel. **International Journal of Concrete Structures and Material**s, 7(4), pp. 253–564.

SÓLYOM, S., and BALÁZS, G. L. (2020). Bond of FRP bars with different surface characteristics. **Construction and Building Materials**, 264, 119839.

SORETZ, S., and HOLZENBEIN, H. (1979). Influence of rib dimensions of reinforcing bars on bond and bendability. In **Journal Proceedings** (Vol. 76, No. 1, pp. 111-128).

THÉRIAULT, M., and BENMOKRANE, B. (1998). Effects of FRP reinforcement ratio and concrete strength on flexural behavior of concrete beams. **J. Comp. Const.**, Vol. 2, No. 1, pp. 7-16.

TRAN, T. D., NGUYEN, M. H., and NGUYEN, T. H. (2018). Experimental Investigation of Bond-Dependent Coefficient of Glass Fiber Reinforced Polymer Bars. In: Tran-Nguyen HH., Wong H., Ragueneau F., Ha-Minh C. (eds) **Proceedings** of the 4th Congrès International de Géotechnique - Ouvrages -Structures. CIGOS 2017. Lecture Notes in Civil Engineering, vol 8. Springer, Singapore.

VOS, E. (1983). **Influence of loading rate and radial pressure on bond in reinforced concrete: A numerical and experimental approach**. Doctoral dissertation. TU Delft, Delft University of Technology.

WU, H. Q., and GILBERT, R. I. (2009). Modeling short-term tension stiffening in reinforced concrete prisms using a continuum-based finite element model. **Eng. Struct.**, vol. 31, no. 10, pp. 2380–2391.

YAN, F., LIN, Z., YANG, M. (2016). Bond mechanism and bond strength of GFRP bars to concrete: a review. **Compos. Part B Eng.** 98, 56–69.

ZOU, Y., and HUCKELBRIDGE, A. (2007). Experimental Analysis of Crack Growth in GFRP Reinforced Concrete. **Journal of Bridge Engineering**, 12(2), 246–255.

APPENDIX A – CHARACTERISTICS OF THE SPECIMENS OF THE EXPERIMENTAL DATABASE

Details of the specimens of the parametric study described in Chapter 3 are presented in Table A.1.

Table A.1 – Details of the specimens of the database of the parametric study.

Reference [a]	Specimen nomenclature	n	Prism size: b x h x L (mm x mm x mm)	f'_c (MPa)	f_{ct} (MPa) *	E_c (GPa) **	d (mm)	d_b (mm)	f_{fu} (MPa)	E_b (GPa)	c_c (mm)	Surface treatment [b]
a	S16-C38-I	1	200 x 300 x 2,800	46.4	4.2	29.5	254	15.9	1,685	65	26.7	iv
a	S16-C50-I	1	200 x 300 x 2,800	46.4	4.2	29.5	254	15.9	1,685	65	26.7	iv
a	S19-C50-I	1	200 x 300 x 2,800	46.4	4.2	29.5	253	19.1	1,484	65	26.7	iv
a	S22-C50-I	1	200 x 300 x 2,800	40.5	3.9	28.0	251	22.2	1,428	68	26.7	iv
a	R16-C38-I	1	200 x 300 x 2,800	43.6	4.0	28.8	254	16	1,100	60	26.7	iv
a	R16-C50-I	1	200 x 300 x 2,800	43.6	4.0	28.8	254	16	1,100	60	26.7	iii
a	R19-C50-I	1	200 x 300 x 2,800	43.6	4.0	28.8	252	20	1,060	64	26.7	iii
a	S16-C38-II	1	200 x 300 x 2,800	40.5	3.9	28.0	254	15.9	1,685	65	25.3	iv
a	R16-C38-II	1	200 x 300 x 2,800	40.5	3.9	28.0	254	16	1,100	60	25.3	iii
	Total	9										
b	B1-35-12	1	200 x 300 x 3,100	34.1	3.3	26.3	246	12	1,166	65	38	v
b	B2-35-16	1	200 x 300 x 3,100	34.1	3.3	26.3	244	16	1,122	65	38	v
b	B3-35-20	1	200 x 300 x 3,100	34.1	3.3	26.3	230	20	1,117	69	50	v
b	B4-35-25	1	200 x 300 x 3,100	34.1	3.3	26.3	228	25	1,340	65	50	v
b	B5-65-12	1	200 x 300 x 3,100	67.5	4.6	34.2	246	12	1,166	65	38	v
b	B6-65-16	1	200 x 300 x 3,100	67.5	4.6	34.2	244	16	1,122	63	38	v
b	B7-65-20	1	200 x 300 x 3,100	67.5	4.6	34.2	230	20	1,117	69	50	v
b	B8-65-25	1	200 x 300 x 3,100	67.5	4.6	34.2	228	25	1,340	65	50	v
	Total	8										
c	2D14-1	1	200 x 300 x 3,000	40.8	3.6	39.2	253	14	928	46	32	ii
c	2D14-2	1	200 x 300 x 3,000	40.8	3.6	39.2	253	14	928	46	32	ii
c	2D16-1	1	200 x 300 x 3,000	40.8	3.6	39.2	252	16	939	46	32	ii
c	2D16-2	1	200 x 300 x 3,000	40.8	3.6	39.2	252	16	939	46	32	ii
c	2D20-1	1	200 x 300 x 3,000	40.8	3.6	39.2	240	20	974	46	42	ii
c	2D20-2	1	200 x 300 x 3,000	40.8	3.6	39.2	240	20	974	46	42	ii
	Total	6										
d	B2#4-1	1	203 x 304 x 3,050	45	3.8	29.2	250	13	887	48.4	38	i
d	B2#4-2	1	203 x 304 x 3,050	45	3.8	29.2	250	13	887	48.4	38	i
d	B2#6-1	1	203 x 304 x 3,050	45	3.8	29.2	234	19	815	49.5	51	i
d	B2#6-2	1	203 x 304 x 3,050	45	3.8	29.2	234	19	815	49.5	51	i
d	B2#8-1	1	203 x 304 x 3,050	45	3.8	29.2	231	25	686	49.6	51	i
d	B2#8-2	1	203 x 304 x 3,050	45	3.8	29.2	231	25	686	49.6	51	i

Reference [a]	Specimen nomenclature	n	Prism size: b x h x L (mm x mm x mm)	f'_c (MPa)	f_{ct} (MPa) *	E_c (GPa) **	d (mm)	d_b (mm)	f_{fu} (MPa)	E_b (GPa)	c_c (mm)	Surface treatment [b]
	Total	6										
e	N2#15G1	1	200 x 400 x 4,250	38.9	3.81	27.6	343	15	762	50.0	40	iv
e	N2#15G3	1	200 x 400 x 4,250	33.8	3.11	26.2	343	15	1,245	59.5	40	iii
e	N3#20G1	1	200 x 400 x 4,250	42.1	3.18	28.4	340	20	728	47.6	40	iv
e	N2#22G1	1	200 x 400 x 4,250	38.9	3.81	27.6	339	22	693	46.4	40	iv
e	N3#20G2	1	200 x 400 x 4,250	48.1	3.96	29.9	340	20	1,082	52.5	40	iv
e	N2#25G1	1	200 x 400 x 4,250	48.1	3.96	29.9	338	25	666	53.2	40	iv
e	N2#25G2	1	200 x 400 x 4,250	48.1	3.96	29.9	338	25	1,132	66.3	40	iv
e	N2#25G3	1	200 x 400 x 4,250	33.8	3.11	26.2	338	25	906	60.3	40	iii
e	H3#20G2	1	200 x 400 x 4,250	81.5	5.45	37.0	340	20	1,082	52.5	40	iv
e	H2#25G1	1	200 x 400 x 4,250	81.5	5.45	37.0	338	25	666	53.2	40	iv
e	H2#25G2	1	200 x 400 x 4,250	81.5	5.45	37.0	338	25	1,132	66.3	40	iv
e	H2#25G3	1	200 x 400 x 4,250	76.5	4.62	36.0	338	25	906	60.3	40	iii
	Total	12										
f	G1-216-25-150	1	180 x 240 x 2,800	33.1	3.2	24.8	201	16	1,313	69.1	25	iii
f	G1-216-25-250	1	180 x 240 x 2,800	33.1	3.2	24.8	201	16	1,313	69.1	25	iii
f	G1-216-25-000	1	180 x 240 x 2,800	33.1	3.2	24.8	201	16	1,313	69.1	25	iii
f	G1-212-25-150	1	180 x 240 x 2,800	33.1	3.2	24.8	203	12	1,231	64.4	25	iii
f	G1-212-40-150	1	180 x 240 x 2,800	33.1	3.2	24.8	188	12	1,231	64.4	40	iii
f	G1-212-55-150	1	180 x 240 x 2,800	34.3	3.3	27.9	173	12	1,231	64.4	55	i
f	G2-213-25-150	1	180 x 240 x 2,800	34.3	3.3	27.9	203	13	827	45.9	25	i
f	G2-213-25-000	1	180 x 240 x 2,800	34.3	3.3	27.9	203	13	827	45.9	25	i
f	G2-310-25-000	1	180 x 240 x 2,800	34.3	3.3	27.9	204	10	827	45.7	25	i
f	G2-213-25-150G	1	180 x 240 x 2,800	34.3	3.3	27.9	203	13	827	45.9	25	i
f	G2-213-25-250G	1	180 x 240 x 2,800	34.3	3.3	27.9	203	13	827	45.9	25	i
f	G2-216-25-150	1	180 x 240 x 2,800	34.3	3.3	27.9	201	16	758	48.8	25	i
f	G2-313-25-150	1	180 x 240 x 2,800	34.3	3.3	27.9	203	13	827	45.9	25	i
	Total	13										
g	G1	1	600 x 300 x 5,000	58.1	3.9	32.2	262	16	683	48.2	30	iv
g	G1-ST	1	600 x 300 x 5,000	58.1	3.9	32.2	252	16	683	48.2	30	iv
	Total	2										
h	B1	1	200 x 300 x 3,000	31	3.1	25.4	243	15.9	724	46.0	38	i
h	B2	1	200 x 300 x 3,000	31	3.1	25.4	229	19.1	690	46.0	50	i
h	B3	1	200 x 300 x 3,000	36	3.4	26.8	243	15.9	724	46.0	38	i
h	B4	1	200 x 300 x 3,000	36	3.4	26.8	229	19.1	690	46.0	50	i
h	B5	1	200 x 300 x 3,000	36	3.4	26.8	231	15.9	724	46.0	50	i
h	B6	1	200 x 300 x 3,000	36	3.4	26.8	241	19.1	690	46.0	38	i
h	B7	1	200 x 300 x 3,000	32	3.2	25.7	243	15.9	724	46.0	38	i
h	B8	1	200 x 300 x 3,000	32	3.2	25.7	229	19.1	690	46.0	50	i
h	B9	1	200 x 300 x 3,000	32	3.2	25.7	243	15.9	724	46.0	38	i
h	B10	1	200 x 300 x 3,000	32	3.2	25.7	229	19.1	690	46.0	50	i
h	B13	1	200 x 300 x 3,000	28	3.0	24.5	243	15.9	724	46.0	38	i

Reference [a]	Specimen nomenclature	n	Prism size: b x h x L (mm x mm x mm)	f'_c (MPa)	f_{ct} (MPa) *	E_c (GPa) **	d (mm)	d_b (mm)	f_{fu} (MPa)	E_b (GPa)	c_c (mm)	Surface treatment [b]
h	B14	1	200 x 300 x 3,000	28	3.0	24.5	229	19.1	690	46.0	50	i
h	B15	1	200 x 300 x 3,000	28	3.0	24.5	243	15.9	724	46.0	38	i
h	B16	1	200 x 300 x 3,000	28	3.0	24.5	229	19.1	690	46.0	50	i
h	S1	1	600 x 150 x 3,000	31	3.1	25.4	107	9.5	765	45.4	38	iv
h	S2	1	600 x 150 x 3,000	31	3.1	25.4	106	12.7	708	46.3	38	iv
h	S3	1	600 x 150 x 3,000	36	3.4	26.8	104	15.9	683	48.2	38	iv
h	S4	1	600 x 150 x 3,000	36	3.4	26.8	102	19.1	656	47.6	38	iv
h	S5	1	600 x 200 x 3,000	30	3.1	25.1	157	9.5	765	45.4	38	iv
h	S6	1	600 x 200 x 3,000	30	3.1	25.1	156	12.7	708	46.3	38	iv
h	S7	1	600 x 200 x 3,000	29	3.0	24.8	154	15.9	683	48.2	38	iv
h	S8	1	600 x 200 x 3,000	29	3.0	24.8	152	19.1	656	47.6	38	iv
h	S9	1	600 x 225 x 3,000	25	2.8	23.5	162	25.4	597	51.9	50	iv
	Total	23										
i	N2#13G2	1	200 x 400 x 4,250	33.5	3.6	26.1	344	13	1,639	67.0	40	iv
i	N3#13G1	1	200 x 400 x 4,250	33.5	3.6	26.1	344	13	817	48.7	40	iv
i	H2#13G2	1	200 x 400 x 4,250	59.1	4.6	32.4	344	13	1,639	67.0	40	iv
i	H3#13G1	1	200 x 400 x 4,250	59.1	4.5	32.4	344	13	817	48.7	40	iv
i	N5#15G2	1	200 x 400 x 4,250	29.0	2.5	24.8	322	16	1,362	69.3	40	iv
i	N6#15G1	1	200 x 400 x 4,250	33.5	3.6	26.1	319	16	762	50.0	40	iv
i	H5#15G2	1	200 x 400 x 4,250	73.4	3.7	35.3	322	16	1,362	69.3	40	iv
i	H6#15G1	1	200 x 400 x 4,250	73.4	3.7	35.3	319	16	762	50.0	40	iv
i	N5#15G3	1	200 x 400 x 4,250	33.8	3.1	26.2	322	16	1,245	59.5	40	iii
i	N2#25G3	1	200 x 400 x 4,250	33.8	3.1	26.2	337	25	906	60.3	40	iii
i	H5#15G3	1	200 x 400 x 4,250	73.4	3.7	35.3	322	16	1,245	59.5	40	iii
i	H2#25G3	1	200 x 400 x 4,250	73.4	3.7	35.3	337	25	906	60.3	40	iii
	Total	12										
j	N-212-D1-A	1	140 x 190 x 2,050	32.1	2.8	25.9	164	12	1,321	63.4	12	iii
j	N-212-D1-B	1	140 x 190 x 2,050	32.1	2.8	25.9	164	12	1,321	63.4	12	iii
j	N-216-D1-A	1	140 x 190 x 2,050	32.1	2.8	25.9	162	16	1,015	64.6	12	iii
j	N-216-D1-B	1	140 x 190 x 2,050	32.1	2.8	25.9	162	16	1,015	64.6	12	iii
j	N-316-D1-A	1	140 x 190 x 2,050	32.1	2.8	25.9	162	16	1,015	64.6	12	iii
j	N-212-D2-A	1	160 x 190 x 2,050	32.1	2.8	25.9	144	12	1,321	63.4	32	iii
j	N-212-D2-B	1	160 x 190 x 2,050	32.1	2.8	25.9	144	16	1,321	63.4	32	iii
j	N-216-D2-A	1	160 x 190 x 2,050	32.1	2.8	25.9	142	16	1,015	64.6	32	iii
j	N-216-D2-B	1	160 x 190 x 2,050	32.1	2.8	25.9	142	16	1,015	64.6	32	iii
j	N-316-D2-A	1	160 x 190 x 2,050	32.1	2.8	25.9	142	16	1,015	64.6	32	iii
j	N-316-D2-B	1	160 x 190 x 2,050	32.1	2.8	25.9	142	16	1,015	64.6	32	iii
	Total	11										
k	N2#4	1	200 x 300 x 3,100	41.5	3.6	28.3	256	12	1,166	65	28	v
k	N2#5	1	200 x 300 x 3,100	41.5	3.6	28.3	254	16	1,122	63	28	v
k	N2#6	1	200 x 300 x 3,100	41.5	3.6	28.3	240	20	1,117	69	40	v
k	N2#8	1	200 x 300 x 3,100	41.5	3.6	28.3	238	25	1,340	65	40	v
	Total	4										

Reference [a]	Specimen nomenclature	n	Prism size: b x h x L (mm x mm x mm)	f'_c (MPa)	f_{ct} (MPa) *	E_c (GPa) **	d (mm)	d_b (mm)	f_{fu} (MPa)	E_b (GPa)	c_c (mm)	Surface treatment [b]
l	G1-6	1	200 x 300 x 3,250	39.05	3.5	29.3	232	12.7	617	40	30	iv
l	G1-8	1	200 x 300 x 3,250	39.05	3.5	29.3	232	12.7	617	40	30	iv
l	G2-6	1	200 x 300 x 3,250	39.05	3.5	29.3	233	12	747	36	30	iii
l	G2-8	1	200 x 300 x 3,250	39.05	3.5	29.3	233	12	747	36	30	iii
	Total	4										
m	G2N0	1	120 x 250 x 1,830	43	5.6	28.7	197	6.4	507	37.8	50	i
m	G3N0	1	120 x 250 x 1,830	39	6.1	27.6	195	9.5	769	43.3	50	i
m	G4N0	1	120 x 250 x 1,830	39	5.4	27.6	194	12.7	690	45.6	50	i
m	G2P1	1	120 x 250 x 1,830	31	5.2	25.4	197	6.4	507	37.8	50	i
m	G3P1	1	120 x 250 x 1,830	33	5.2	26.0	195	9.5	769	43.3	50	i
m	G4P1	1	120 x 250 x 1,830	30	5.0	25.1	194	12.7	690	45.6	50	i
	Total	6										
n	C3 X 8.5H5	1	76 x 215 x 1,830	27.9	4.9	24.4	182	15.9	655	40.8	25	i
n	C4 X 8.5H5	1	102 x 215 x 1,830	27.9	4.9	24.4	182	15.9	655	40.8	25	i
n	C5 X 8.5H5	1	127 x 215 x 1,830	27.9	4.9	24.4	182	15.9	655	40.8	25	i
n	C6 X 8.5H5	1	152 x 215 x 1,830	27.9	4.9	24.4	182	15.9	655	40.8	25	i
n	C3 X 8.5P5	1	76 x 215 x 1,830	27.9	4.9	24.4	182	15.9	674	42	25	iv
n	C4 X 8.5P5	1	102 x 215 x 1,830	27.9	4.9	24.4	182	15.9	674	42	25	iv
n	C5 X 8.5P5	1	127 x 215 x 1,830	27.9	4.9	24.4	182	15.9	674	42	25	iv
n	C6 X 8.5P5	1	152 x 215 x 1,830	27.9	4.9	24.4	182	15.9	674	42	25	iv
	Total	8										
o	GIS-6	1	200 x 300 x 3,300	39.05	3.5	29.3	232	12.7	617	40	30	i
o	GIS-8	1	200 x 300 x 3,300	39.05	3.5	29.3	232	12.7	617	40	30	i
o	GCB-6	1	200 x 300 x 3,300	39.05	3.5	29.3	233	12	747	36	30	iii
o	GCB-8	1	200 x 300 x 3,300	39.05	3.5	29.3	233	12	747	36	30	iii
	Total	4										
p	S-G1	1	1,000 x 200 x 3,100	40	3.5	30	162	15.9	597	40	30	iv
p	S-G2	1	1,000 x 200 x 3,100	40	3.5	30	159	22.2	540	40	30	iv
p	S-G3	1	1,000 x 200 x 3,100	40	3.5	30	159	22.2	540	40	30	iv
	Total	3										
q	1A, 1B	2	190 x 225 x 2,900	44	3.7	29.0	179	15	675	41	35	iv
q	2A, 2B	2	190 x 225 x 2,900	36	3.4	26.8	179	15	675	41	35	iv
q	3A, 3B	2	190 x 225 x 2,900	42	3.6	28.4	179	15	675	41	35	iv
q	4A, 4B	2	190 x 225 x 2,900	46	3.8	29.4	179	15	675	41	35	iv
	Total	8										
r	BC2NA	1	130 x 180 x 1,800	53.1	4.1	33.0	148	12.3	773	38	20	v
r	BC2NB	1	130 x 180 x 1,800	53.1	4.1	33.0	148	12.3	773	38	20	v
r	BC2HA	1	130 x 180 x 1,800	57.2	4.2	34.0	148	12.3	773	38	20	v
r	BC2HB	1	130 x 180 x 1,800	57.2	4.2	34.0	148	12.3	773	38	20	v

Reference [a]	Specimen nomenclature	n	Prism size: b x h x L (mm x mm x mm)	f'_c (MPa)	f_{ct} (MPa) *	E_c (GPa) **	d (mm)	d_b (mm)	f_{fu} (MPa)	E_b (GPa)	c_c (mm)	Surface treatment [b]
r	BC2VA	1	130 x 180 x 1,800	97.4	5.5	42.1	148	12.3	773	38	20	v
r	BC4NA	1	130 x 180 x 1,800	46.2	3.8	31.6	119	12.3	773	38	20	v
r	BC4HA	1	130 x 180 x 1,800	53.9	4.1	33.2	119	12.3	773	38	20	v
r	BC4HB	1	130 x 180 x 1,800	53.9	4.1	33.2	119	12.3	773	38	20	v
r	BC4VA	1	130 x 180 x 1,800	93.5	5.4	41.1	119	12.3	773	38	20	v
r	BC4VB	1	130 x 180 x 1,800	93.5	5.4	41.1	119	12.3	773	38	20	v
	Total	10										
s	CB2B-1	1	200 x 300 x 3,300	52	4.0	33.0	253	14.9	773	37.6	30	v
s	CB2B-2	1	200 x 300 x 3,300	52	4.0	33.0	253	14.9	773	37.6	30	v
s	CB3B-1	1	200 x 300 x 3,300	52	4.0	33.0	253	14.9	773	37.6	30	v
s	CB3B-2	1	200 x 300 x 3,300	52	4.0	33.0	253	14.9	773	37.6	30	v
s	CB4B-1	1	200 x 300 x 3,300	45	4.0	33.0	230	14.9	773	37.6	30	v
s	CB4B-2	1	200 x 300 x 3,300	45	4.0	33.0	230	14.9	773	37.6	30	v
s	CB6B-1	1	200 x 300 x 3,300	45	4.0	33.0	230	14.9	773	37.6	30	v
s	CB6B-2	1	200 x 300 x 3,300	45	4.0	33.0	230	14.9	773	37.6	30	v
	Total	8										

[a] Reference list given in Section 3.1.
[b] Surface treatment: i = helically wrapped with sand-coated; ii = helically wrapped; iii = grooved/ indented; iv = sand-coated; v = ribbed.
n = number of specimens.
f'_c = concrete compressive strength.
b x h x L = width x height x length.
f'_c = concrete compressive strength.
* f_{ct} = concrete tensile strength (for studies in which f_{ct} was not reported by authors, nominal f_{ct} is calculated in this work by equation $f_t = 0.56\sqrt{f'_c}$) [ACI 318-14]).
** E_c = modulus of elasticity of concrete (for studies in which E_c was not reported by authors, nominal E_c is calculated in this work by Equation [C.2]).
d = depth of the section.
d_b = bar diameter.
f_{fu} = tensile strength of the GFRP bar.
E_b = modulus of elasticity of bar.
c_c = clear cover.

APPENDIX B – CALCULATION EXAMPLE: BOND-DEPENDENT COEFFICIENT FOR CRACK WIDTH EQUAL TO 0.70 MM

This appendix presents beam N2#13G2 tested by El-Nemr et al. (2013) as an example of calculation of the bond-dependent coefficient, k_b, at crack width equal to 0.70 mm (Figure 3.2). The calculation follows the elastic cracked section theory that is based on the following assumptions: (i) the section is cracked but remains linear elastic and (ii) the concrete in tension is considered to be ineffective while the GFRP reinforcement takes all tensile stress.

B.1 Geometric characteristics and mechanical properties of materials

- Compressive strength of concrete: f'_c = 33.5 MPa.
- Modulus of elasticity of concrete: E_c = 26.1 GPa.
- Nominal diameter of GFRP bar: d_b = 13 mm.
- Reinforcement configuration: 2 ϕ13 mm diameter bars in 1 layer.
- Total area of GFRP reinforcement: A_f = 258 mm².
- Modulus of elasticity of GFRP bar: E_b = 67 GPa.
- Tensile strength of GFRP bar: f_{fu} = 1639 MPa.
- Stirrup configuration: double legged d_s = 10 mm diameter.
- Cross section (b x h): 200 mm x 400 mm.
- Span of the beam: L = 4,250 mm.
- Clear cover: c_c = 40 mm.
- Reinforcement ratio: ρ_f = 0.38%.

B.2 Procedure for calculation of the bond-dependent coefficient

Rearranging Frosch equation (Equation 2.11) to calculate k_b at w = 0.70 mm:

$$k_{b,w=0.70} = \frac{w}{2\frac{f_f}{E_b}\beta\sqrt{{d_c}^2 + \left(\frac{s}{2}\right)^2}} \quad \text{(B.1)}$$

B.2.1 Tensile stress in GFRP reinforcement, f_f

The stress in GFRP reinforcement can be calculated as:

$$f_f = \frac{M}{A_f jd} \quad \text{(B.2)}$$

where M is the applied moment equal to 25 kN.m corresponding to crack width of 0.7 mm (see Figure B.1), A_f = 258 mm², and jd is the moment arm between tension and compression force computed as (ACI PRC 440.1, 2007):

$$j = 1 - \frac{1}{3}k \quad \text{(B.3)}$$

and

$$k = \sqrt{2\rho_f\eta + \left(\rho_f\eta\right)^2} - \rho_f\eta \quad \text{(B.4)}$$

where η is the modular ratio: $\eta = E_b / E_c$.

Thus: η = 2.57, k = 0.13, and j = 0.96.

Figure B.1 – Moment-to-maximum crack width relationships.

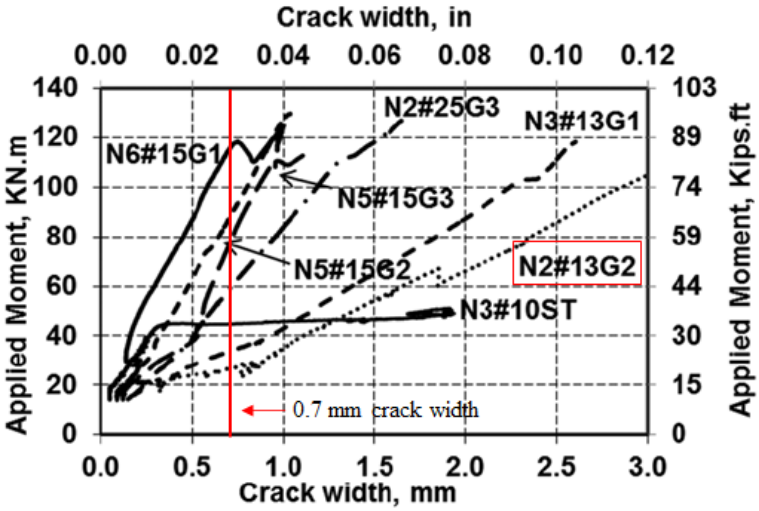

Source: El-Nemr et al. (2013).

The effective depth, d, is calculated as:

$$d = h - d_c \tag{B.5}$$

where d_c is the thickness of concrete cover measured to the center of bar calculated as:

$d_c = c_c + d_s + (d_b/2) = 56.4$ mm; making $d = 343.6$ mm.

B.2.2 Ratio of the distance from the neutral axis of the member to the extreme tension fiber to the distance from the neutral axis to the centroid of the tensile reinforcement, β

The factor β can be estimated as (Park and Paulay, 1975):

$$\beta = \frac{h - x}{d - x} \tag{B.6}$$

where x is the depth of the neutral axis calculated as:

$$x = \frac{\sqrt{2dB + 1} - 1}{B} \tag{B.7}$$

and

$$B = \frac{b}{\eta A_f} \tag{B.8}$$

Then, B = 0.30, x = 44.5, and β = 1.19.

B.2.3 Longitudinal GFRP bar spacing, s

The longitudinal GFRP bar spacing in the experimental specimen can be estimated as:

$$s = b - c_{c,l} * 2 - d_s * 2 - d_b \quad \text{(B.9)}$$

where $c_{c,l}$ is the lateral clear cover equal to 25 mm. Thus, s = 117 mm.

B.2.4 Bond-dependent coefficient for crack width of 0.70 mm, $k_{b,w=0.70}$

Finally, the bond-dependent coefficient for crack width equal to 0.70 mm calculated by Equation [B.1] is 0.82.

All other data presented in Chapter 3 is calculated similarly when k_b is not explicitly reported in the source material.

APPENDIX C – CALCULATION OF TENSILE STRENGTH OF C3 CONCRETE

Considering the prism to be a composite element, the assumption of perfect bond (i.e., $\varepsilon_c = \varepsilon_b$) in the uncracked section can be applied. Starting from such hypothesis, the C3 concrete tensile strength, f_{ct}, can be estimated by equating the strains in the concrete and bar to that of the composite transformed section:

$$\frac{N_c}{E_c A_c} = \frac{N_b}{E_b A_b} = \frac{N}{E_c A_c + E_b A_b} \tag{C.1}$$

where N_c and N_b are the portion of the load carried by the concrete and the bar, respectively; that is, $N_c + N_b$ = applied load N; E_c and A_c are the modulus of elasticity and the area of the concrete, respectively; and E_b and A_b are the modulus of elasticity and the area of the reinforcing bar, respectively.

The modulus of elasticity of concrete can be calculated as (Carrasquillo et al., 1981):

$$E_c = 3320\sqrt{f'_c} + 6900 \tag{C.2}$$

where f'_c is the concrete compressive strength.

Finally, the concrete tensile strength, f_{ct}, can be determined using the measured load corresponding to the appearance of the first crack, P_1:

$$f_{ct} = \frac{1}{A_c}\frac{P_1 A_c E_c}{E_c A_c + E_b A_b} = \frac{P_1 E_c}{E_c A_c + E_b A_b} \tag{C.3}$$

Table C.1 shows the results for tensile strength for the twelve prisms tested.

Table C.1 – Calculation of tensile strength of C3 concrete.

Prism	#4 steel		#6 steel			#4 rGFRP		#6 rGFRP			#4 sGFRP	
Specimen	1	2	1	2	3	1	2	1	2	3	1	2
d_b (mm)	12.7		19.1			12.7		19.1			12.7	
Nominal A_b (mm²)	127		287			127		287			127	
b (mm)	100		150			100		150			100	
L (mm)	1905		2860			1905		2860			1905	
$A_c = A_g - A_b$ (mm²)	9873		22213			9873		22213			9873	
E_b (GPa)	200		200			60.3		60.3			46.9	
E_c (MPa)	27.3											
P_1 (kN)	22.2	23.7	46.3	39.8	52.8	20.0	31.5	49.9	33.3	49.7	28.1	32.8
f_{ct} (MPa)	2.06	2.20	1.91	1.64	2.17	1.97	3.11	2.18	1.46	2.18	2.79	3.25
Average f_{ct} (MPa) (COV)	2.24 (0.24)											

APPENDIX D – PULL-OUT TESTS RESULTS FOR ALL SPECIMENS

The experimental results for all the 80 specimens tested are detailed in Table D.1. Specimens having #2 and #3 bars were tested at CEFET-MG (Brazil) and with larger #4, #5 and #6 bars were tested at the University of Pittsburgh (USA).

Table D.1 – Pull-out test results.

Bar	Specimen	Concrete batch	$\tau_{0.05}$ (MPa)	$\tau_{0.10}$ (MPa)	$\tau_{0.25}$ (MPa)	τ_{max} (MPa)	Average free end slip at τ_{max} (mm)	k_b at τ_{max}	Failure mode*
#2 steel	1	C1	2.59	4.28	8.03	12.18	1.059		PO
#2 steel	2	C1	1.38	2.25	6.06	12.70	1.193		PO
#2 steel	3	C1	1.57	3.29	6.18	10.59	0.932	n.a.	PO
#2 steel	4	C1	1.05	1.99	5.24	10.86	1.038		PO
#2 steel	5	C1	2.90	4.43	6.27	10.62	1.241		PO
		Average	1.90	3.25	6.36	11.39	1.093		
		COV	0.42	0.34	0.16	0.09	0.11		
#3 steel	1	C2	5.83	8.26	12.14	17.44	1.109		PO
#3 steel	2	C2	5.62	7.44	10.71	16.81	1.261		PO
#3 steel	3	C2	0.17	0.38	6.57	17.01	1.512	n.a.	PO
#3 steel	4	C2	2.11	3.44	5.45	10.39	1.582		PO
#3 steel	5	C2	3.47	5.43	8.41	12.96	1.254		PO
		Average	3.44	4.99	8.66	14.92	1.344		
		COV	0.70	0.64	0.32	0.21	0.15		
#2 hGFRP	1	C1	3.92	6.37	11.45	17.56	1.453		PO
#2 hGFRP	2	C1	0.91	2.95	9.39	18.37	1.453		PO
#2 hGFRP	3	C1	1.83	4.59	13.20	22.17	1.242	0.62	PO
#2 hGFRP	4	C1	0.15	0.23	1.02	19.86	2.006		PO
#2 hGFRP	5	C1	2.71	5.22	9.68	14.03	1.560		PO
		Average	1.90	3.87	8.95	18.40	1.543		
		COV	0.78	0.62	0.52	0.16	0.18		
#3 hGFRP	1	C2	1.22	1.46	2.56	9.77	2.893		PO
#3 hGFRP	2	C2	1.23	1.59	2.66	10.72	2.763		PO
#3 hGFRP	3	C2	2.59	3.37	5.34	12.07	2.269	1.25	PO
#3 hGFRP	4	C2	2.50	3.22	6.01	16.17	2.904		PO
#3 hGFRP	5	C2	1.33	1.77	2.86	10.99	2.875		PO
		Average	1.77	2.28	3.89	11.94	2.741		
		COV	0.40	0.41	0.43	0.21	0.10		
#4 steel	1	C3	E	E	E	16.40	1.296		PO
#4 steel	2	C3	E	E	E	14.64	1.034		PO
#4 steel	3	C3	6.67	8.02	13.72	17.36	0.974	n.a.	PO
#4 steel	4	C3	3.87	5.23	9.57	15.40	1.260		PO
#4 steel	5	C3	6.96	9.11	14.07	17.20	0.834		PO

Bar	Specimen	Concrete batch	$\tau_{0.05}$ (MPa)	$\tau_{0.10}$ (MPa)	$\tau_{0.25}$ (MPa)	τ_{max} (MPa)	Average free end slip at τ_{max} (mm)	k_b at τ_{max}	Failure mode*
#4 steel	6	C3	8.84	10.97	14.72	20.10	0.925		PO
#4 steel	7	C3	5.94	8.59	12.85	15.91	0.953		PO
#4 steel	8	C3	7.38	8.11	13.69	18.47	0.735		PO
#4 steel	9	C3	7.70	9.71	12.38	14.51	0.662		PO
#4 steel	10	C3	10.39	11.07	12.99	14.50	0.808		PO
		Average	7.22	8.85	13.00	16.45	0.95		
		COV	0.27	0.21	0.12	0.11	0.22		
#6 steel	1	C3	E	E	E	E	E		S
#6 steel	2	C3	E	E	E	E	E		S
#6 steel	3	C3	E	E	E	E	E		S
#6 steel	4	C3	E	E	E	19.35	1.747		PO
#6 steel	5	C3	E	E	E	18.98	1.551	n.a.	PO
#6 steel	6	C3	E	E	E	18.61	1.454		PO
#6 steel	7	C3	E	E	E	20.59	1.020		PO
#6 steel	8	C3	9.78	11.51	14.84	17.28	0.949		PO
#6 steel	9	C3	6.17	9.55	15.25	24.33	1.259		PO
#6 steel	10	C3	9.11	11.27	16.70	24.14	1.000		PO
		Average	8.35	10.78	15.60	20.47	1.28		
		COV	0.23	0.10	0.06	0.13	0.24		
#4 rGFRP	1	C3	3.82	5.03	7.72	15.90	2.294		PO
#4 rGFRP	2	C3	3.70	4.09	5.78	12.13	2.322		PO
#4 rGFRP	3	C3	2.14	2.90	4.71	10.02	2.302		PO
#4 rGFRP	4	C3	3.33	4.07	5.80	14.02	3.046		PO
#4 rGFRP	5	C3	2.68	3.51	5.28	9.96	2.551	1.31	PO
#4 rGFRP	6	C3	2.81	3.21	4.78	10.20	3.062		PO
#4 rGFRP	7	C3	3.05	3.77	5.28	10.53	2.681		PO
#4 rGFRP	8	C3	E	3.62	5.54	13.71	2.811		PO
#4 rGFRP	9	C3	4.44	4.86	6.59	13.98	2.768		PO
#4 rGFRP	10	C3	3.81	4.61	6.50	14.65	2.472		PO
		Average	3.31	3.97	5.80	12.51	2.63		
		COV	0.21	0.18	0.16	0.18	0.11		
#6 rGFRP	1	C3	E	E	E	15.56	1.116		PO
#6 rGFRP	2	C3	E	E	E	14.04	2.289		PO
#6 rGFRP	3	C3	E	E	E	11.12	1.927		PO
#6 rGFRP	4	C3	E	E	E	12.54	1.949		PO
#6 rGFRP	5	C3	4.34	5.21	6.87	13.46	1.914	1.43	PO
#6 rGFRP	6	C3	3.55	4.67	6.94	13.03	2.192		PO
#6 rGFRP	7	C3	6.23	7.29	9.08	14.37	1.653		PO
#6 rGFRP	8	C3	4.93	5.48	7.36	14.77	2.106		PO
#6 rGFRP	9	C3	6.57	7.77	11.36	20.20	1.839		PO
#6 rGFRP	10	C3	3.69	4.50	6.65	14.38	2.222		PO
		Average	4.89	5.82	8.04	14.35	1.92		
		COV	0.26	0.24	0.23	0.17	0.18		
#4 sGFRP	1	C3	E	E	E	9.85	0.804		PO
#4 sGFRP	2	C3	6.29	7.40	7.62	7.65	0.154	2.24	PO
#4 sGFRP	3	C3	E	1.89	2.72	3.44	0.770		PO

Bar	Specimen	Concrete batch	$\tau_{0.05}$ (MPa)	$\tau_{0.10}$ (MPa)	$\tau_{0.25}$ (MPa)	τ_{max} (MPa)	Average free end slip at τ_{max} (mm)	k_b at τ_{max}	Failure mode*
#4 sGFRP	4	C3	9.51	10.27	11.95	11.95	0.237		PO
#4 sGFRP	5	C3	5.32	5.63	5.35	5.63	0.076		PO
#4 sGFRP	6	C3	4.12	5.04	5.91	6.43	0.761		PO
#4 sGFRP	7	C3	2.18	3.15	4.31	4.74	0.656		PO
#4 sGFRP	8	C3	8.28	10.30	10.81	11.13	0.548		PO
#4 sGFRP	9	C3	5.10	5.80	7.07	7.70	0.885		PO
#4 sGFRP	10	C3	2.29	2.97	4.14	4.79	0.861		PO
		Average	5.39	5.83	6.66	7.33	0.58		
		COV	0.48	0.52	0.46	0.39	0.53		
#5 sGFRP	1	C3	5.22	7.33	8.53	8.99	3.878		PO
#5 sGFRP	2	C3	10.10	11.14	11.48	11.52	0.307		PO
#5 sGFRP	3	C3	7.13	9.02	10.01	10.40	0.516	n.a.	PO
#5 sGFRP	4	C3	5.57	6.54	8.16	9.70	7.690		PO
#5 sGFRP	5	C3	10.20	10.75	11.74	13.27	6.350		PO
		Average	7.64	8.96	9.98	10.78	3.75		
		COV	0.31	0.23	0.16	0.16	0.89		
#5 sGFRP-s	1	C3	E	E	E	9.35	6.658		PO
#5 sGFRP-s	2	C3	4.09	5.54	6.53	9.23	7.268		PO
#5 sGFRP-s	3	C3	7.27	8.50	10.38	12.43	4.805	n.a.	PO
#5 sGFRP-s	4	C3	3.57	4.49	6.39	11.31	8.646		PO
#5 sGFRP-s	5	C3	5.36	6.56	7.86	12.02	8.677		PO
		Average	5.07	6.27	7.79	10.87	7.21		
		COV	0.32	0.27	0.24	0.14	0.22		

E = error during data acquisition.

* PO = pull-out of the bar; S = splitting of the concrete cube.

APPENDIX E – DETAILS OF THE COMPLETE EXPERIMENTAL DATABASE OF PULL-OUT TESTS

Table E.1 – Results of the pull-out tests of the experimental database.

Bar type	ASTM A615 Gr. 60 steel							
ID	R14				#2 steel	#3 steel	#4 steel	#6 steel
Reference	Sólyom and Balázs (2020)				This study			
Image of the bar (all images are not in the same scale)								
d_b (mm)	6	6	8	8	6.3	9.5	12.7	19
A_b (mm²)	28.3	28.3	50.3	50.3	31	71	129	284
E_b (MPa)	210	210	210	210	200	200	200	200
f_{fu} (MPa)	> 500	> 500	> 500	> 500	500	500	500	500
R_r	0.092	0.092	0.120	0.120	0.049	0.086	0.074	0.089
s_r (mm)	4.3	4.3	6.0	6.0	4.4	6.2	8.6	11.8
Cube size, b (mm)	150	150	150	150	200	200	200	200
f'_c (MPa)	35.3	66.1	35.3	66.1	33.2	35.0	37.8	37.8
f_{ct} (MPa)	2.9	4.6	2.9	4.6	3.1	2.9	2.2	2.2
$l_b = 5d_b$ (mm)	30	30	40	40	31.5	47.5	63.5	95
τ_{avg} at 0.002 mm slip (MPa)	1.52	2.05	8.51	5.66	n.a.	n.a.	n.a.	n.a.
COV	0.30	0.18	0.78	0.53				
n	4	4	4	3				
τ_{avg} at 0.05 mm slip (MPa)	3.71	6.82	11.6	16.05	1.90	3.44	7.22	8.35
COV	0.32	0.42	0.53	0.08	0.42	0.70	0.27	0.23
n	4	4	4	3	5	5	8	3
τ_{avg} at 0.10 mm or at 0.15 mm slip (MPa)	6.09[a]	13.41[a]	15.46[a]	23.11[a]	3.25[b]	4.99[b]	8.85[b]	10.78[b]
COV	0.22	0.33	0.44	0.09	0.34	0.64	0.21	0.10
n	4	4	4	3	5	5	8	3
τ_{avg} at 0.25 mm slip (MPa)	n.a.	n.a.	n.a.	n.a.	6.36	8.66	13	15.6
COV					0.16	0.32	0.12	0.06
n					5	5	8	3
$\tau_{max,avg}$ (MPa)	11.66	20.04	21.85	25.23	11.39	14.92	16.45	20.47
COV	0.21	0.17	0.30	0.07	0.09	0.21	0.11	0.13
n	4	4	4	3	5	5	10	7
Average free end slip at τ_{max} (mm)	0.786	0.585	0.545	0.751	1.09	1.34	0.95	1.28
COV	0.25	0.46	0.36	0.28	0.11	0.15	0.22	0.24
n	4	4	4	4	5	5	10	7
k_b at τ_{max}	n.a.	n.a.	n.a.	n.a.	n.a.	n.a.	n.a.	n.a.

Bar type	Fine sand-coated GFRP						Coarse sand-coated GFRP	Sand-coated GFRP
ID	R2		R5				R4	#4 sGFRP
Reference	Sólyom and Balázs (2020)							This study
Image of the bar (all images are not in the same scale)								
d_b (mm)	6	10	6	10	12	12	6	12.7
A_b (mm²)	28.3	78.5	28.3	78.5	113.1	113.1	28.3	129
E_b (MPa)	54.5 – 59.9	54.5 – 59.9	50.0 – 55.0	50.0 – 55.0	50.0 – 55.0	50.0 – 55.0	54.5 – 59.9	46.9
f_{fu} (MPa)	1308 – 1415	1308 – 1415	990 – 1130	990 – 1130	990 – 1130	990 – 1130	1308 – 1415	927
R_r s_r (mm)	n.a.	n.a.	n.a.	n.a.	n.a.	n.a.	n.a.	n.a.
Cube size, b (mm)	150	150	150	150	150	150	150	200
f'_c (MPa)	35.3	35.3	35.3	35.3	35.3	66.1	35.3	37.8
f_{ct} (MPa)	2.9	2.9	2.9	2.9	2.9	4.6	2.9	2.2
$l_b = 5d_b$ (mm)	30	50	30	50	60	60	30	63.5
τ_{avg} at 0.002 mm slip (MPa)	6.53	8.04	9.95	11.11	E	10.20	6.70	n.a.
COV	0.26	0.16	0.12	0.13	n.a.	0.34	0.27	
n	4	4	4	4		4	4	
τ_{avg} at 0.05 mm slip (MPa)	6.52	3.17	4.72	7.08	3.3	3.42	4.38	5.39
COV	0.11	0.26	0.10	0.38	0.36	0.21	0.28	0.48
n	4	4	4	4	4	4	4	8
τ_{avg} at 0.10 mm or at 0.15 mm slip (MPa)	11.55[a]	8.18[a]	11.87[a]	14.54[a]	8.42[a]	10.30[a]	11.03[a]	5.83[b]
COV	0.15	0.14	0.09	0.15	0.27	0.19	0.11	0.52
n	4	4	4	4	4	4	4	9
τ_{avg} at 0.25 mm slip (MPa)	n.a.	n.a.	n.a.	n.a.	n.a.	n.a.	n.a.	6.66
COV								0.46
n								9
$\tau_{max,avg}$ (MPa)	13.97	13.18	23.67	20.10	17.53	22.85	18.78	7.33
COV	0.17	0.09	0.03	0.03	0.08	0.03	0.13	0.39
n	4	4	4	4	4	4	4	10
Average free end slip at τ_{max} (mm)	0.198	0.226	0.329	0.276	E	0.026	0.243	0.580
COV	0.29	0.34	0.25	0.28	n.a.	1.35	0.19	0.53
n	4	4	4	4		4	4	10
k_b at τ_{max}	**0.83**	n.a.	**0.49**	n.a.	n.a.	n.a.	**0.79**	2.24

Bar type	Sand-coated GFRP	Most sand removed GFRP	Helically wrapped GFRP		Helically wrapped GFRP			
ID	#5 sGFRP	#5 sGFRP-s	#2 hGFRP	#3 hGFRP	R6			
Reference	This study				Sólyom and Balázs (2020)			
Image of the bar (all images are not in the same scale)								
d_b (mm)	15.9	15.9	6.3	9.5	6	6	8	8
A_b (mm²)	200	200	31	71	28.3	28.3	50.3	50.3
E_b (MPa)	48.4	48.4	28	37	45.9 – 46.8	45.9 – 46.8	45.9 – 46.8	45.9 – 46.8
f_{fu} (MPa)	738.6	738.6	590	973	1117 – 1288	1117 – 1288	1117 – 1288	1117 – 1288
R_r	n.a.	n.a.	0.035	0.050	0.043	0.043	0.047	0.047
s_r (mm)			15.4	13.3	18.3	18.3	21.0	21.0
Cube size, b (mm)	200	200	200	200	150	150	150	150
f'_c (MPa)	37.8	37.8	33.2	35.0	35.3	66.1	35.3	66.1
f_{ct} (MPa)	2.2	2.2	3.1	2.9	2.9	4.6	2.9	4.6
$l_b = 5d_b$ (mm)	79.5	79.5	31.5	47.5	30	30	40	40
τ_{avg} at 0.002 mm slip (MPa)	n.a.	n.a.	n.a.	n.a.	2.88	1.25	3.17	E
COV					0.18	0.26	0.50	n.a.
n					4	4	3	
τ_{avg} at 0.05 mm slip (MPa)	7.64	5.07	1.90	1.77	1.5	1.58	2.75	1.71
COV	0.31	0.32	0.78	0.40	0.53	0.16	0.46	0.49
n	5	4	5	5	4	4	3	4
τ_{avg} at 0.10 mm or at 0.15 mm slip (MPa)	8.96[(b)]	6.27[(b)]	3.87[(b)]	2.28[(b)]	3.74[(a)]	4.43[(a)]	5.76[(a)]	4.79[(a)]
COV	0.23	0.27	0.62	0.41	0.42	0.12	0.22	0.40
n	5	4	5	5	4	4	3	4
τ_{avg} at 0.25 mm slip (MPa)	9.98	7.79	8.95	3.89	n.a.	n.a.	n.a.	n.a.
COV	0.16	0.24	0.52	0.43				
n	5	4	5	5				
$\tau_{max,avg}$ (MPa)	10.78	10.87	18.40	11.94	17.90	21.19	16.54	26.74
COV	0.16	0.14	0.16	0.21	0.20	0.17	0.08	0.06
n	5	5	5	5	4	4	3	4
Average free end slip at τ_{max} (mm)	3.750	7.210	1.54	2.74	1.695	2.825	1.367	E
COV	0.89	0.22	0.19	0.10	0.51	0.50	n.a.	n.a.
n	5	5	5	5	4	4	2	n.a.
k_b at τ_{max}	n.a.	n.a.	**0.62**	1.25	**0.65**	**0.95**	1.32	**0.94**

Bar type	Helically wrapped and sand-coated GFRP							
ID	R7						R8	
Reference	Sólyom and Balázs (2020)							
Image of the bar (all images are not in the same scale)								
d_b (mm)	6	6	8	10	12	12	6	8
A_b (mm²)	28.3	28.3	50.3	78.5	113.1	113.1	28.3	50.3
E_b (MPa)	46	46	46	46	46	46	> 45	> 45
f_{fu} (MPa)	827 – 896	827 – 896	827 – 896	827 – 896	827 – 896	827 – 896	> 1100	> 1100
R_r	0.021	0.021	0.021	0.015	0.024	0.024	0.051	0.037
s_r (mm)	24.2	24.2	24.2	24.6	23.1	23.1	6.1	6.8
Cube size, b (mm)	150	150	150	150	150	150	150	150
f'_c (MPa)	35.3	66.1	35.3	35.3	35.3	66.1	35.3	35.3
f_{ct} (MPa)	2.9	4.6	2.9	2.9	2.9	4.6	2.9	2.9
$l_b = 5d_b$ (mm)	30	30	40	50	60	60	30	40
τ_{avg} at 0.002 mm slip (MPa)	7.05	7.36	3.17	7.83	5.77	11.66	7.58	9.26
COV	0.19	n.a.	n.a.	n.a.	0.03	0.03	0.46	0.15
n	4	2	2	2	4	3	3	3
τ_{avg} at 0.05 mm slip (MPa)	5.34	6.77	2.75	4.64	2.76	10.67	4.27	5.53
COV	0.47	0.20	0.46	0.11	0.13	0.21	0.41	0.21
n	4	4	3	3	4	3	4	3
τ_{avg} at 0.10 mm or at 0.15 mm slip (MPa)	10.66[(a)]	14.20[(a)]	5.76[(a)]	10.31[(a)]	6.50[(a)]	17.22[(a)]	9.11[(a)]	9.99[(a)]
COV	0.15	0.11	0.22	0.07	0.12	0.02	0.19	0.11
n	4	4	3	3	4	3	4	3
τ_{avg} at 0.25 mm slip (MPa)	n.a.	n.a.	n.a.	n.a.	n.a.	n.a.	n.a.	n.a.
COV								
n								
$\tau_{max,avg}$ (MPa)	13.59	18.37	18.27	18.39	13.55	21.86	16.22	16.45
COV	0.10	0.05	0.12	0.11	0.08	0.10	0.05	0.08
n	4	4	3	3	4	3	4	3
Average free end slip at τ_{max} (mm)	0.153	0.125	0.268	0.380	0.513	0.245	0.215	0.206
COV	0.04	n.a.	0.40	0.28	0.12	0.09	0.21	0.20
n	4	2	3	3	3	3	3	3
k_b at τ_{max}	**0.86**	1.09	1.20	n.a.	n.a.	n.a.	**0.72**	1.33

Bar type	Helically wrapped and sand-coated GFRP					Indented GFRP		
ID	R8		R9			R10		
Reference	Sólyom and Balázs (2020)							
Image of the bar (all images are not in the same scale)								
d_b (mm)	8	6	8	8	10	8	8	12
A_b (mm²)	50.3	28.3	50.3	50.3	78.5	50.3	50.3	113.1
E_b (MPa)	> 45	> 50	> 50	> 50	> 50	60	60	60
f_{fu} (MPa)	> 1100	> 1100	> 1100	> 1100	> 1100	1500	1500	1500
R_r	0.037	0.059	0.043	0.043	0.035	0.055	0.055	0.090
s_r (mm)	6.8	5.2	6.1	6.1	7.1	8.3	8.3	8.7
Cube size, b (mm)	150	150	150	150	150	150	150	150
f'_c (MPa)	66.1	35.3	35.3	66.1	35.3	35.3	66.1	35.3
f_{ct} (MPa)	4.6	2.9	2.9	4.6	2.9	2.9	4.6	2.9
$l_b = 5d_b$ (mm)	40	30	40	40	50	40	40	60
τ_{avg} at 0.002 mm slip (MPa)	10.39	11.93	9.34	11.29	8.86	1.94	3.07	3.21
COV	n.a.	0.15	0.46	0.11	0.26	0.39	0.28	0.26
n	2	4	3	4	4	3	4	4
τ_{avg} at 0.05 mm slip (MPa)	2.80	2.55	6.53	10.95	7.78	3.06	3.19	4.41
COV	0.30	0.18	0.39	0.14	0.17	0.07	0.09	0.18
n	4	4	4	4	4	3	4	4
τ_{avg} at 0.10 mm or at 0.15 mm slip (MPa)	8.20[(a)]	6.95[(a)]	13.91[(a)]	16.95[(a)]	13.86[(a)]	6.81[(a)]	8.59[(a)]	8.66[(a)]
COV	0.10	0.16	0.18	0.11	0.13	0.25	0.10	0.15
n	4	4	4	4	4	3	4	4
τ_{avg} at 0.25 mm slip (MPa)	n.a.	n.a.	n.a.	n.a.	n.a.	n.a.	n.a.	n.a.
COV								
n								
$\tau_{max,avg}$ (MPa)	22.57	20.79	19.36	23.00	18.03	10.75	17.70	12.23
COV	0.09	0.10	0.11	0.15	0.10	0.15	0.12	0.12
n	4	4	4	4	4	3	4	4
Average free end slip at τ_{max} (mm)	1.047	0.247	0.203	1.938	0.248	0.470	0.314	0.574
COV	n.a.	0.23	0.14	0.07	0.13	0.03	0.12	0.35
n	2	4	3	4	4	3	4	4
k_b at τ_{max}	1.12	**0.56**	1.13	1.10	n.a.	2.03	1.43	n.a.

Bar type	Indented GFRP	Ribbed GFRP				GFRP with machined ribs	
ID	R10	R12		R13		#4 rGFRP	#6 rGFRP
Reference	Sólyom and Balázs (2020)					This study	
Image of the bar (all images are not in the same scale)							
d_b (mm)	12	12	12	12	12	12.7	19
A_b (mm²)	113.1	113.1	113.1	113.1	113.1	129	284
E_b (MPa)	60	42.5	42.5	42.5	42.5	60.3	603
f_{fu} (MPa)	1500	> 1000	> 1000	> 1000	> 1000	962	898
R_r	0.090	0.082	0.082	0.074	0.074	0.030	0.024
s_r (mm)	8.7	5.9	5.9	7.3	7.3	10.2	10.4
Cube size, b (mm)	150	150	150	150	150	200	200
f'_c (MPa)	66.1	35.3	66.1	35.3	66.1	37.8	37.8
f_{ct} (MPa)	4.6	2.9	4.6	2.9	4.6	2.2	2.2
$l_b = 5d_b$ (mm)	60	60	60	60	60	63.5	95
τ_{avg} at 0.002 mm slip (MPa)	5.82	4.36	8.21	4.06	3.92	n.a.	n.a.
COV	0.22	0.09	0.07	0.06	0.04		
n	4	4	4	4	4		
τ_{avg} at 0.05 mm slip (MPa)	10.84	3.58	8.12	1.77	2.7	3.31	4.89
COV	0.38	0.15	0.15	0.11	0.54	0.21	0.26
n	4	4	4	4	4	9	6
τ_{avg} at 0.10 mm or at 0.15 mm slip (MPa)	15.74[(a)]	8.28[(a)]	18.40[(a)]	5.32[(a)]	6.21[(a)]	3.97[(b)]	5.82[(b)]
COV	0.26	0.12	0.11	0.15	0.26	0.18	0.24
n	4	4	4	4	4	10	6
τ_{avg} at 0.25 mm slip (MPa)	n.a.	n.a.	n.a.	n.a.	n.a.	5.80	8.04
COV						0.16	0.23
n						10	6
$\tau_{max,avg}$ (MPa)	18.40	15.13	28.36	15.38	18.09	12.51	14.35
COV	0.17	0.08	0.10	0.02	0.04	0.18	0.17
n	4	4	4	4	4	10	10
Average free end slip at τ_{max} (mm)	0.230	1.556	0.559	1.438	1.747	2.63	1.92
COV	0.12	0.07	0.22	0.20	0.27	0.11	0.18
n	4	4	4	4	4	10	10
k_b at τ_{max}	n.a.	n.a.	n.a.	n.a.	n.a.	1.31	1.43

[(a)] Bond stress corresponding to 0.15 mm loaded end slip.
[(b)] Bond stress corresponding to 0.10 mm free end slip.